MODEL CATALYSIS OF AMMONIA SYNTHESIS AND IRON-WATER
INTERFACES – A SUM FREQUENCY GENERATION VIBRATIONAL
SPECTROSCOPIC STUDY OF SOLID-GAS INTERFACES AND ANION
PHOTOELECTRON SPECROSCOPIC STUDY OF SELECTED ANION
CLUSTERS

by

Michael James Ferguson

B. CHE. (University of Dayton) 2001

A dissertation submitted in partial satisfaction of the

Requirements for the degree of

Doctor of Philosophy

in

Chemistry

in the

GRADUATE DIVISION

of the

UNIVERSITY OF CALIFORNIA, BERKELEY

Committee in Charge:

Professor Gabor A. Somorjai, Chair

Professor Ronald C. Cohen

Professor Robert W. Dibble

Fall 2005

Abstract

MODEL CATALYSIS OF AMMONIA SYNTHESIS AND IRON-WATER
INTERFACES – A SUM FREQUENCY GENERATION VIBRATIONAL
SPECTROSCOPIC STUDY OF SOLID-GAS INTERFACES AND ANION
PHOTOELECTRON SPECROSCOPIC STUDY OF SELECTED ANION
CLUSTERS

by

Michael James Ferguson

Doctor of Philosophy in Chemistry

University of California, Berkeley

Professor Gabor A. Somorjai, Chair

The ammonia synthesis reaction has been studied using single crystal model

catalysis combined with sum frequency generation (SFG) vibrational spectroscopy.

The adsorption of gases N_2, H_2, O_2 and NH_3 that play a role in ammonia synthesis

have been studied on the Fe(111) crystal surface by sum frequency generation

vibrational spectroscopy using an integrated Ultra-High Vacuum (UHV) / high-

pressure system. SFG spectra are presented for the dissociation intermediates, NH_2

(~3325 cm^{-1}) and NH (~3235 cm^{-1}) under high pressure of ammonia or equilibrium

concentrations of reactants and products on Fe(111) surfaces.

Special attention was paid to understand how potassium promotion of the iron

catalyst affects the intermediates of ammonia synthesis. An Fe(111) surface promoted

with 0.2 monolayers of potassium red shifts the vibrational frequencies of the reactive

surface intermediates, NH and NH_2, providing evidence for weakened the nitrogen-

hydrogen bonds relative to clean Fe(111). Spectral features of these surface

intermediates persisted to higher temperatures for promoted iron surfaces than for clean Fe(111) surfaces implying that nitrogen-iron bonds are stronger for the promoted surface. The ratio of the NH to NH_2 signal changed for promoted surfaces in the presence of equilibrium concentrations of reactants and products. The order of adding oxygen and potassium to promoted surfaces does not alter the spectra indicating that ammonia induces surface reconstruction of the catalyst to produce the same surface morphology.

When oxygen is co-adsorbed with nitrogen, hydrogen, ammonia or potassium on Fe(111), a relative phase shift of the spectra occurs as compared to the presence of adsorbates on clean iron surfaces.

Water adsorption on iron was also probed using SFG vibrational spectroscopy. For both H_2O and D_2O, the only spectral feature was in the range of the free OH or free OD. From the absence of SFG spectra of ice-like structure we conclude that surface hydroxides are formed and no liquid water is present on the surface.

Other than model catalysis, gas phase anion photoelectron spectroscopy of the Cl + H_2 van der Waals well, silicon clusters, germanium clusters, aluminum oxide clusters and indium phosphide clusters were studied. The spectra help to map out the neutral potential energy surfaces of the clusters. For aluminum oxide, the structures of the anions and neutrals were explored and for silicon, germanium and indium phosphide the electronic structure of larger clusters was mapped out.

Dedication

This dissertation is dedicated to the love of my life, Megan Kathleen Kelly, my

family, especially my parents and for the greater glory of God, in hope that any

knowledge conferred herein will be used for the betterment of humankind.

Table of Contents

List of Figures

List of Tables

Acknowledgements

I am faced with the difficult task to cram into this short space as much thanks as I can for all those who have made my graduate studies at Berkeley possible for these past four years. Those who are not mentioned by name are no means insignificant. I would like to start by thanking the staff of both LBNL and Berkeley. Everyone has played an integral role in my graduate career and is deserving of gratitude. Of special note I would like to thank the College of Chemistry machine shop and electronics shop. I would also like to thank Lisa Torres who helped me significantly and Lynn Keithlin of the chemistry graduate office.

My research group has been almost like my scientific family and has made my stay much more interesting. I appreciate all the friendship and scholarly advice that was bestowed all these years. Particularly, I would like to thank Staffan Westerberg for training me in the laboratory, Kevin Becraft, Lucio Flores and Sasha Kweskin for their help in teaching me SFG. Diana Phillips and Roger York have also been good laboratory companions with helping me deal with the laser. Max Montano and Anthony Contreras always provided inspiring conversations. The rest of the group must be mentioned too for their camaraderie and occasional fooseball partaking. Inger Coble has also been a great help for many of the administrative duties. I would also like to thank Gabor Somorjai for being a great advisor. He has helped me develop and grow over these past years and is interested in helping me continue to grow past my graduation, making his advisory role a true mentorship.

I have also been blessed with many friends during my short stay (without which would have certainly felt much longer) at Berkeley to whom I hope to keep for

a lifelong duration. There are of course the chemistry department friends I have made who are always great company at Chem Keg or other events like Cody Folden and Aaron Van Tassle. There is of course Dr. Dan Horner with our wild and interesting "adventure nights." I will always smile when I think of sneaking up and scaring sweet Beth Kautzman. Also, the members of the Alpha Beta Chapter of The Sigma Chi Fraternity who have been constant friends during my tenure at Berkeley certainly have contributed to my education. And to the rest of my friends who are not mentioned, but important to me nonetheless.

My family has also been a constant source of love and support through my graduate career. I drew the most strength from my parents and siblings through any tough times and shared in the joys during the good times. I am lucky to have such a great family markedly since I moved thousands of miles away to be at Berkeley.

I would like to especially acknowledge Meg. Falling in love with you has been the best experience of my life and will continue to affect me all my days. I hope that in the future, I can read these words and be taken back into time where now we have just built a life together and are looking forward to our incumbent marriage. I was torn between two things when I first entered graduate school: the lab with my thirst for knowledge and the longing I always felt to be with you. Leaving you every day to pursue my dreams was difficult and caused me to fall into reflection over what drove me to leave and pursue my studies. I am overjoyed to say that over these years we have grown so that I do not have to forsake ambition to accomplish what I want; rather, together we have become a means for each other such that we have both

become stronger and are both more capable of success than apart. My Love, I look

forward to spending each and every moment with you until the end of time.

Chapter 1.   Introduction – Model catalysis of ammonia synthesis and iron-water interfaces – a sum frequency generation vibrational spectroscopic study of solid-gas interfaces

Preface:

Modern ammonia synthesis is a catalytic process where hydrogen and nitrogen are mixed in a 3:1 stoichiometric mixture and are reacted on the surface of an iron catalyst. The surface science and catalysis of this reaction has been extensively studied. The research presented in this thesis is a study of how surface adsorbents affect the reactive intermediates, emphasizing the promotion effect of potassium. The primary technique used in this study is sum frequency generation vibrational spectroscopy.

Historical perspective:

The development of the technology for ammonia synthesis has some interesting historical roots. Ammonia's current main use is in fertilizer production, but prior to the mass-production of ammonia, fertilizer was generated from organic media and a small percentage mined[1]. Ammonia synthesis is has made the population boom possible raising the world's population from 1.6 billion in 1900 to almost 6 billion today[2]. In 1798, T.R. Malthus noticed that the human population was growing geometrically while food production was growing arithmetically. He concluded that eventually, the human race would grow beyond what the earth could sustain. What Malthus predicted started to become a reality near the start of the twentieth century[3]. Then in 1898 Sir William Crookes gave a speech challenging

chemists to find a source of food for the world. Crookes stated in a speech to the

British Association for the Advancement of Science[4]:

> "It is the chemist who must come to the rescue of the threatened
>
> communities. It is through the laboratory that starvation may
>
> ultimately be turned into plenty. Before we are in the grip of actual
>
> dearth the chemist will step in and postpone the day of famine to
>
> so distant a period that we and our sons and grandsons may
>
> legitimately live without undue solicitude for the future."

One solution to this predicament was to find a way to economically and efficiently

fixate nitrogen, since it was already known that fertilizers containing nitrogen

compounds greatly improved crop yields.

This goal was realized by Fritz Haber in 1908[4, 5] when he was able to

produce ammonia in a substantial yield from nitrogen and hydrogen by the use of an

osmium catalyst at a pressure of about 175 bar and at 550 °C. Haber's apparatus

produced about 90 grams of ammonia per hour with about 98 grams of the osmium

catalyst[1, 3, 6, 7]. Due to the cost of osmium, research into more economically

feasible catalysts was conducted. Then Alwin Mittasch of BASF in 1910 found that

adding alumina, Al_2O_3, and potash, K_2O, to iron was a suitable catalyst for ammonia

synthesis.

At this point, there was a sizable gap between Fritz Haber's apparatus and a

full-sized plant that would be able to mass-produce ammonia. The largest part of this

problem was the high pressure of reactant gasses that was needed to produce

ammonia. The technology to perform this high pressure reaction was developed by

Carl Bosch of BASF in 1913 who oversaw the first factory dedicated to ammonia synthesis in Oppau, Germany[1, 8, 9]. This factory was able to produce 30 tons of ammonia per day with 300 Kg of the doubly promoted iron catalyst with a total pressure of 200 atmospheres of the nitrogen and hydrogen reactant gasses.

The technology lead to the realization of mass-produced nitrogen fixation, both Fritz Haber and Carl Bosch received Nobel prizes for their work. Haber received his for his work on the catalytic synthesis of ammonia and Bosch for his development of the high-pressure technology enabling mass-production of ammonia.

There have been significant improvements in ammonia synthesis since the first factory that Carl Bosch started in 1913 both in the catalyst and in the manufacturing technology. Advances in the pressure containment equipment and in the production of the reactant gasses, nitrogen and hydrogen, have made ammonia synthesis more energy efficient and cost-effective[1]. Even though nearly one hundred years has passed since the work of Haber and Bosch, the basic composition and method of synthesis is relatively unchanged.

Industrial ammonia synthesis:

Since the development of the ammonia synthesis catalyst in 1913, there have been no major changes in the composition of the iron catalyst. To prepare the catalyst, potassium oxide and aluminum oxide are fused with magnetite, Fe_3O_4, at about 1600 °C followed by reduction by hydrogen. This catalyst is referred to as "doubly promoted" iron; whereas, if no potassium oxide is added and just alumina is added to the iron catalyst, this catalyst is referred to as "singly promoted." Industrial catalysts

may also contain oxides of calcium, magnesium, or silicon depending on reaction conditions[1].

After the catalyst is prepared, it is introduced to a 3:1 stoichiometric ratio of hydrogen and nitrogen. This production of reactant synthesis gas is described in Figure 1.1.
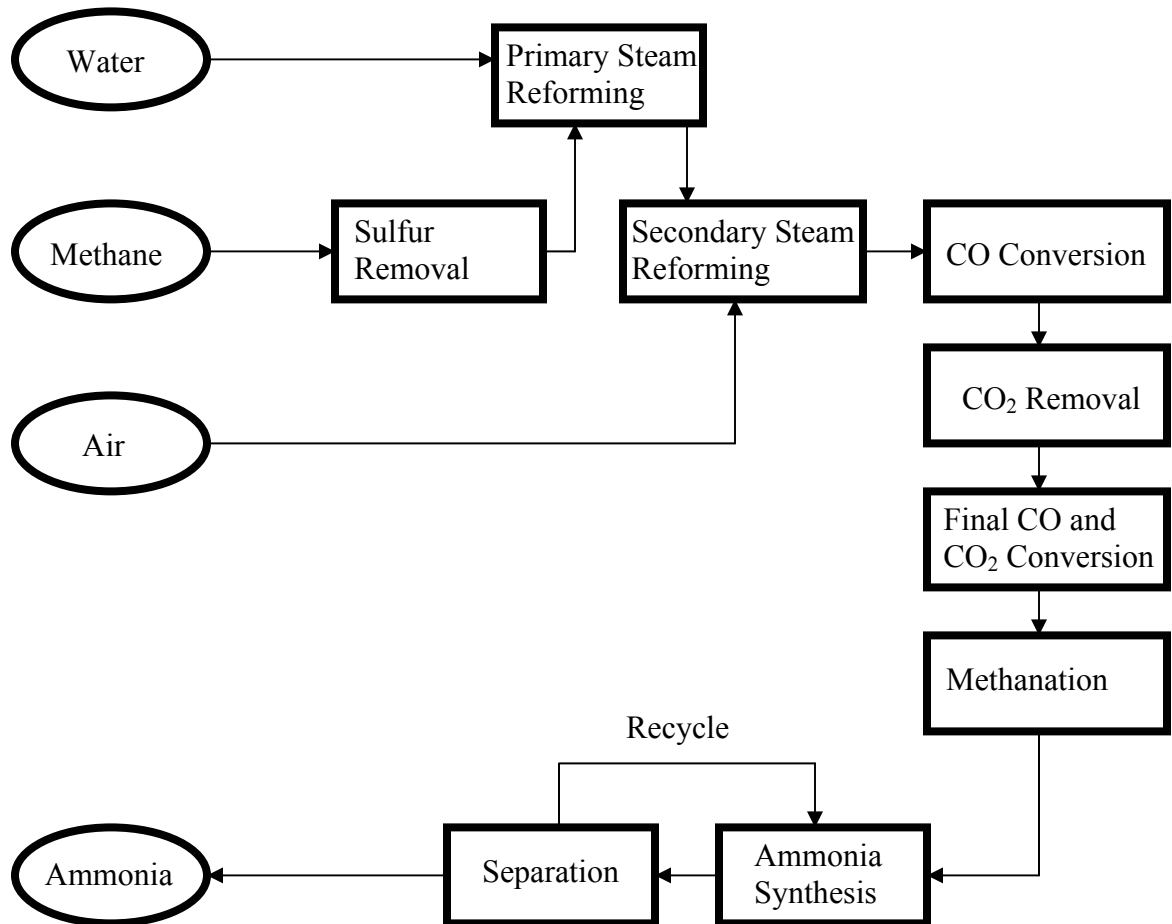
Figure 1.1 – Industrial Ammonia Synthesis.

The synthesis starts out with methane, water and air. The methane and water react to provide hydrogen. Air contributes oxygen for combustion reactions to increase the temperature of the mixture gasses and nitrogen for the ammonia synthesis. The

methane first needs to have any residual sulfur removed from it because sulfur will greatly reduce the activity of the catalysts used in ammonia synthesis. The sulfur is first hydrogenated to form hydrogen sulfide by using a cobalt/molybdenum catalyst or a catalyst that is a mixture of cobalt and nickel on an alumina support. The hydrogen sulfide is then adsorbed onto zinc oxide.

$$RSH_{(g)} + H_{2(g)} \rightarrow H_2S_{(g)} + RH_{(g)} \tag{1.1}$$

$$H_2S_{(g)} + ZnO_{(s)} \rightarrow ZnS_{(s)} + H_2O_{(g)} \tag{1.2}$$

The methane is then reacted with steam for primary steam reformation. The primary steam reformation takes place over a nickel oxide catalyst. The overall reaction is endothermic and consists of the following gas phase reactions:

$$CH_{4(g)} + H_2O_{(g)} \rightarrow CO_{(g)} + 3H_{2(g)} \tag{1.3}$$

$$CO_{(g)} + H_2O_{(g)} \rightarrow CO_{2(g)} + H_{2(g)} \tag{1.4}$$

Since the overall reaction is endothermic, the temperature is increased to drive the reaction to the right. Secondary steam reforming further produces heat by adding air to the mixture, combusting both methane and hydrogen increasing the temperature and the concentration of steam. More hydrogen gas is produced in the secondary steam reforming by the same reaction as equation 1.4 over a nickel oxide catalyst. The air added in this stage also provides for the nitrogen necessary for the production of ammonia. After the reactant gasses leave the secondary steam reformation stage, they need to be cooled. The heat from the cooled gas can be used to generate electricity or to preheat the gasses entering the primary or secondary steam reformers to further increase the efficiency of the overall ammonia production[10]. After the gasses are cooled, the carbon monoxide needs to be converted. This takes place in

two stages, a high temperature shift and a low temperature shift following the reaction

in equation 1.4. The high temperature shift takes place over an iron oxide/zinc oxide

catalyst. The gas is then cooled and the low temperature shift takes place over a

copper oxide/zinc oxide catalyst. Next, the carbon dioxide needs to be removed. The

carbon dioxide is removed by a hot aqueous potassium carbonate solution by the

following reaction:

$$K_2CO_{3(aq)} + H_2O_{(l)} + CO_{2(g)} \rightarrow 2KHCO_{3(aq)} \tag{1.5}$$
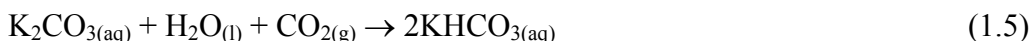
The reactant gasses may further be purified by methanation over a nickel oxide

catalyst by the following reactions to remove any residual CO and CO_2:

$$CO_{(g)} + 3H_{2(g)} \rightarrow CH_{4(g)} + H_2O_{(g)} \tag{1.6}$$

$$CO_{2(g)} + 4H_{2(g)} \rightarrow CH_{4(g)} + 2H_2O_{(g)} \tag{1.7}$$

The synthesis gas mixture then enters into the reactor where ammonia synthesis takes

place. The catalyst in this reaction is promoted magnetite (iron oxide). Ammonia is

formed in the reactor and then separated. The unused reactant gasses are recycled.

There are many possible steps in ammonia synthesis that involve a wide range of

catalytic surfaces, but the emphasis of the research presented in this thesis is on the

iron ammonia synthesis catalyst.

Basics of Ammonia Synthesis:

Ammonia synthesis from hydrogen and nitrogen is an exothermic process.

This reaction is described in equation 1.8:

$$3H_{2(g)} + N_{2(g)} \rightarrow 2NH_{3(g)} \qquad \Delta H^0 = -92.4 \text{ kJ mol}^{-1} \tag{1.8}$$

The rate-determining step for this synthesis is the dissociation of nitrogen[1]. For the

iron catalyst, nitrogen dissociates more rapidly over highly coordinated iron. Figure

1.2 shows some of the iron surfaces and the coordination number of the surface iron atoms. The Fe(111) and Fe(211) surfaces are the only ones shown that have iron with seven nearest neighbors on the surface and are the more reactive surfaces. Figure 1.3 compares the reactivity of these surfaces. The addition of a "structural promoter" like alumina to the iron catalyst results in the restructuring of the iron surface to expose the Fe(111) or Fe(211) surfaces[11]. This reconstruction is advantageous because the highly coordinated iron is the most reactive to ammonia synthesis. Addition of potassium promotes the ammonia synthesis by decreasing the heat of adsorption of nitrogen[1, 12] and decreasing the heat of adsorption of ammonia[1] over the iron surface which will aid in both decreasing the barrier for the rate-determining step and free up more sites once ammonia is produced. Norskov and coworkers further explored this cause of this promoter effect and determined that it was due to electrostatic effects of the potassium[13]. A potassium atom's electric field induces the Stark effect to nearby molecules, thereby splitting the molecular orbitals allowing more electron density to enter into the antibonding orbitals. This then lowers the heat of adsorption of the nitrogen and ammonia on the potassium promoted iron surface.
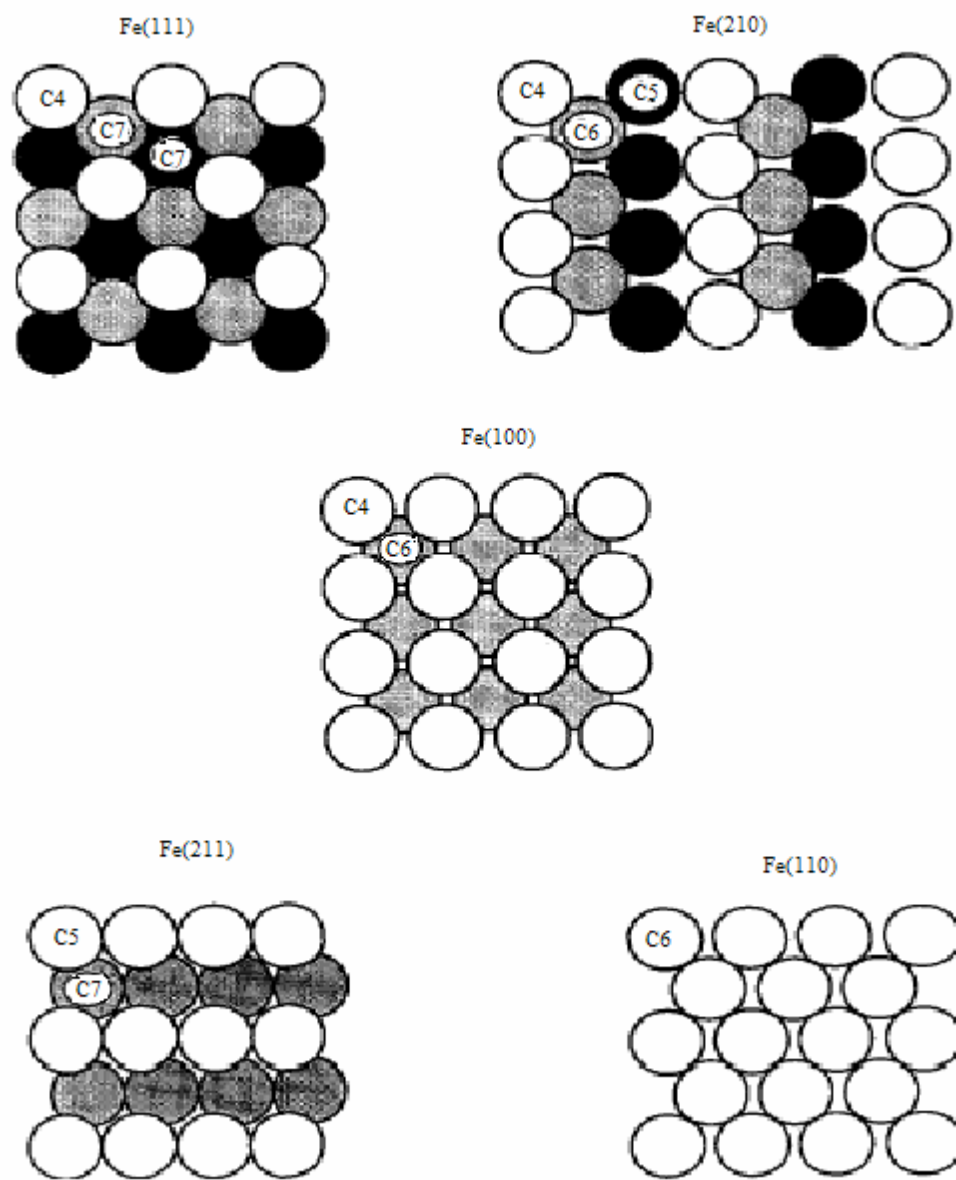
Figure 1.2 – Comparison of the iron surfaces [14].

673K, 20 atm 3:1 H2:N2
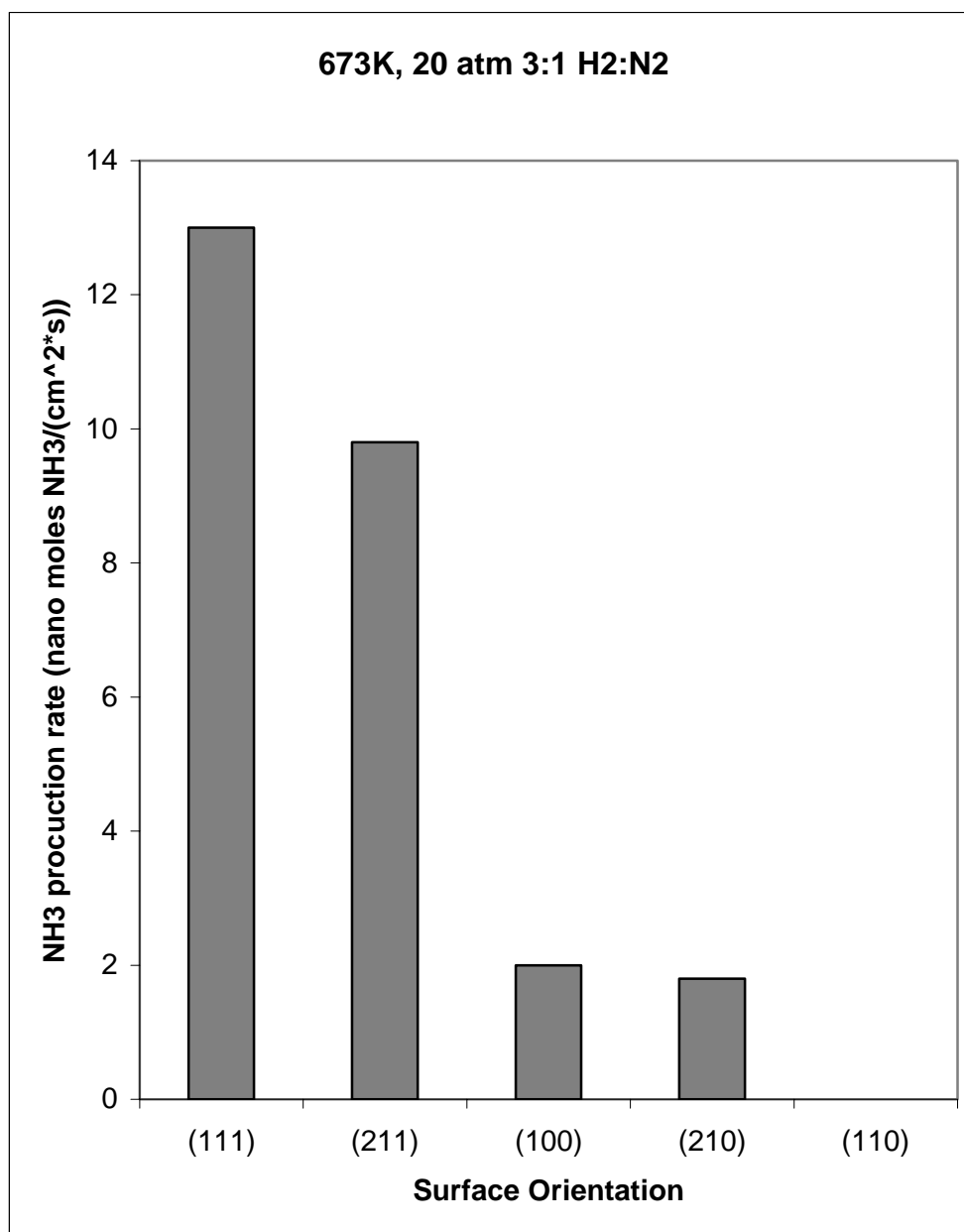
Figure 1.3 – The relative reactivates of the iron surface for ammonia synthesis[14]. The x-axis shows the different iron surfaces and the y-axis gives the reactivity of the surface to ammonia synthesis.

Sum frequency generation vibrational spectroscopy:

The primary technique used in this thesis to study the model catalysis of ammonia synthesis is sum frequency generation (SFG) vibrational spectroscopy. The portion on SFG in this chapter will discuss the theory involved in SFG; the experimental section of the thesis will describe the experimental setup in the laboratory. SFG is conceptually simple to understand, two incumbent light beams, one visible ω_{vis} and one infrared ω_{IR}, combine to form the sum frequency.

$$\omega_{IR} + \omega_{vis} = \omega_{sum} \tag{1.9}$$

This process relies on a non-linear optical effect. The intensity of the SFG varies if the infrared beam is in resonance with a vibrational mode of a molecule at the iron single crystal surface. The spectra presented are the intensity of the sum frequency of the light generated as the infrared frequencies are scanned.

The selection rules of SFG activity differ in other linear vibrational techniques like those for infrared and Raman spectroscopies. In order for a vibration to be sum frequency active, it must be in an asymmetric environment. This makes the technique particularly suited for surface science because an isotropic distribution of molecules in a bulk phase is centrosymmetric and therefore inactive to SFG. An interface in an isotropic bulk phase does break the symmetry, so the interface can be SFG active. Furthermore, in order for these interfacial molecules to be SFG active, they need to have a net polarization, so randomly oriented molecules on a surface will not yield an SFG spectrum.

The technique of sum frequency generation is a relatively new tool for surface scientists. In 1962 SFG was both first observed [15] and described in theory[16]. The

field had to wait until high powered pulsed lasers were developed before the surfaces of interfaces were able to be probed[17-19] because only lasers provided the intense electric fields necessary to induce non-linear effects. Currently, the use of SFG as a surface technique has gained a lot of attention and as such has generated many publications on the theory and phenomena in the literature[18, 20-27]. To aid in the understanding of the spectra presented in this thesis, a brief description of the SFG process is presented, first starting in linear optics because almost every phenomenon observed in everyday life is governed by linear optics, then move our discussion into non-linear optics.

A molecule consists of several atoms. Each atom has a positive nucleus and a negative electron cloud associated with it. This separation of charges can lead to a dipole, especially in the presence of an electric field. The electron distribution in the molecule responds to this external field. In the presence of this field, the induced dipole, μ, is given by:

$$\mu = \mu^0 + \alpha E \tag{1.10}$$

where μ^0 is the static dipole, α is the polarizability and E is the electric field. Since the induced dipole is not, in general, in the same direction as E, α can be represented by a (3 X 3) tensor. In the condensed phase experimental setup, it is more convenient to consider the polarization, P, or dipole moment per unit volume. In an electric field:

$$P = P^{(0)} + \varepsilon_0 \chi^{(1)} E \tag{1.11}$$

where $\chi^{(1)}$, the linear susceptibility, takes the place of polarizability and $P^{(0)}$ is the static polarizability. Since few materials have static polarizability, that term can be neglected. For a simple molecular material, the susceptibility depends on the number

of molecules per unit volume, N, multiplied by the molecular polarizability averaged over all the orientations of the molecules in the material. Now the linear susceptibility can be described as:

$$\chi^{(1)} = \frac{N <\alpha>}{\varepsilon_0} \qquad (1.12)$$

The linear properties of an isotropic material are characterized by the complex refractive intex, n. The refractive index is related to the linear susceptibility by:

$$n = \sqrt{1 + \chi^{(1)}} \qquad (1.13)$$

The real part of the refractive index determines the speed of light, v, in the medium:

$$v = \frac{c}{\text{Re}(n)} \qquad (1.14)$$

The imaginary part of the refractive index determines the adsorption coefficient:

$$\alpha = \frac{4\pi}{\lambda_0} \text{Im} \sqrt{1 + \chi^{(1)}} \qquad (1.15)$$

where λ_0 is the wavelength of light in a vacuum.

Since lasers can produce intense beams of light, the strength of the electric field is comparable to the electron field felt by an electron in a molecule. The response of the electron to the electric field mush now must include both the linear and non-linear terms. The dipole moment is now described as:

$$\mu = \mu^0 + \alpha E + \beta : EE + \gamma \vdots EEE + ... \qquad (1.16)$$

where β and γ are the first and second hyperpolarizabilities. The notation is described as follows:

$$\beta : EE = \sum_{j,k} \beta_{ijk} E_j E_k \qquad (1.17)$$

12

The corresponding expression for polarization is:

$$P = \varepsilon_0(\chi^{(1)}E + \chi^{(2)} : EE + \chi^{(3)} \vdots EEE + ...$$ (1.18)

The second order susceptibility, $\chi^{(2)}$, is a third order tensor and the third order

susceptibility, $\chi^{(3)}$, is a fourth order tensor. These non-linear optical terms are

generally much smaller than $\chi^{(1)}$ and are generally neglected when the electric field

is weak. If this electric field is greater than 10^6 V/m, then these non-linear optical

terms can no longer be neglected. Optical processes that arise from $\chi^{(2)}$ and $\chi^{(3)}$ are

known as second and third order non-linear processes. One of the consequences of

these non-linear terms is that the frequency of light can change. Consider an electric

field of the form:

$$E = E(r) \cos \omega t$$ (1.19)

in a material with a non-zero second order susceptibility. $P^{(2)}$ is then:

$$P^{(2)} = \varepsilon_0 \chi^{(2)} : EE$$ (1.20)

$$P^{(2)} = \varepsilon_0 \chi^{(2)} : E(r)E(r)\cos^2 \omega t$$ (1.21)

$$P^{(2)} = \varepsilon_0 \chi^{(2)} : E(r)E(r)(1 + \cos 2\omega t)$$ (1.22)

The first term in equation 1.22 represents the static electric field of the material. The

second term, EE, denotes a dipole oscillating at twice the frequency of the incident

light, 2ω. This oscillating dipole can emit a photon of light at the frequency, 2ω. The

process by which the frequency of the incoming light is doubled is known as second

harmonic generation (SHG). If there are two laser beams with different frequencies of

light ω_1 and ω_2 present simultaneously, then additional terms for $P^{(2)}$ appear in the

form:

$$P^{(2)} = \varepsilon_0 \chi^{(2)} : E_1(r)E_2(r)\cos\omega_1 t \cos\omega_2 t \qquad (1.23)$$

$$P^{(2)} = \frac{1}{2}\varepsilon_0 \chi^{(2)} : E_1(r)E_2(r)[\cos(\omega_1 + \omega_2)t + \cos(\omega_1 - \omega_2)t] \qquad (1.24)$$

Now there are dipoles oscillating at different frequencies $(\omega_1 + \omega_2)$ and

$(\omega_1 - \omega_2)$ known as the SFG and the difference frequency generation (DFG)

respectively. In this
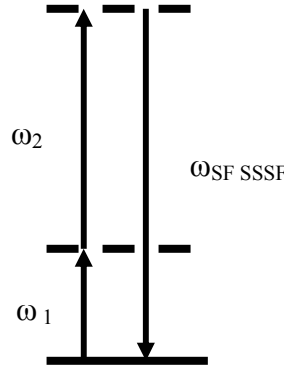
Figure 1.4. Sum frequency generation.

experiment, SFG vibrational spectroscopy is used and ω_1 and ω_2 are chosen for

visible and infrared beams respectively. The intensity, I, of the emitted light depends

on $\left|P^{(2)}\right|^2$, so for the intensity of the SFG beam

$$I(\omega_1 + \omega_2) \propto \left|\chi^{(2)}\right|^2 I(\omega_{vis})I(\omega_{IR}) \qquad (1.25)$$

Generally, the sum frequency will be generated in all directions; however, the sum

frequency is strongly peaked in one direction from phase matching conditions. For

the energy transfer to be maximized, the conservation of energy and momentum must

14

be conserved. Energy conservation requires the relation in equation 1.9 while momentum conservation requires:

$$\mathbf{k}_{vis} + \mathbf{k}_{IR} = \mathbf{k}_{sum} \tag{1.26}$$

now considering the angles of incidence of the two beams:

$$k_{vis}\sin \theta_{vis} + k_{IR}\sin \theta_{IR} = k_{sum}\sin \theta_{sum} \tag{1.27}$$

where k_{vis}, k_{IR} and k_{sum} are the wavenumbers, $2\pi/\lambda$, θ_{vis} and θ_{IR} are the angles of incidence of the laser beams and θ_{sum} is the angle of the sum frequency light.

Expanding upon equation 1.25, one can write the intensity of the sum frequency as:

$$I(\omega_{sum}) \propto \left| \chi_{eff}^{(2)} \right|^2 \tag{1.28}$$

for vibrationally resonant SFG, equation 1.28 can be described as:

$$I(\omega_{sum}) \propto \left| \chi_{NR} + \sum_q \frac{A_q e^{i\vartheta_q}}{\omega_{IR} - \omega_q + i\Gamma_q} \right|^2 \tag{1.29}$$

where χ_{NR} is the nonresonant contributions, A_q is the vibrational mode strength, Γ_q is the damping term and θ_q is the relative phase between the nonresonant contribution and the qth vibrational mode. The second part of equation 1.29 is maximized when the incident infrared laser frequency matches a vibrational mode of a surface species. Equation 1.29 suggests that there are three parts to an SFG spectrum: the first part is a nonresonant background contribution from χ_{NR}, the second is a resonant contribution from the second term and the third comes from interactions between the resonant and nonresonant contributions.
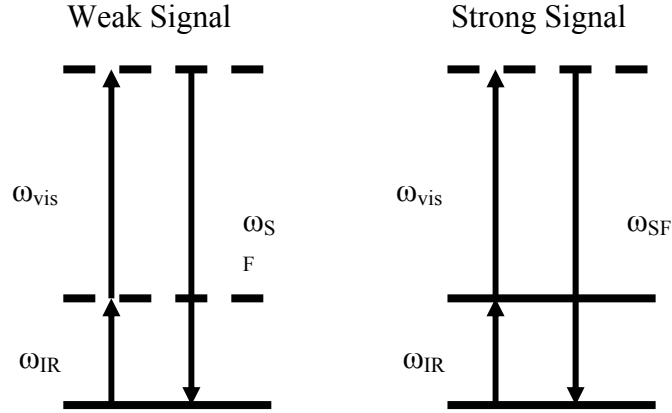
Figure 1.5 – Resonant versus nonresonant sum frequency generation. When the infrared beam matches a surface vibrational state (on the right side), the signal is resonantly enhanced and is larger than when the infrared beam does not match a surface vibrational state (on the left side).

In analogy with the linear optical equation 1.12:

$$\chi_R^{(2)} = \frac{N < \beta >}{\varepsilon_0} \tag{1.30}$$

where the resonant part of the effective non-linear susceptibility is found by averaging over the hyperpolarizability, β, over all orientations of molecules. Near a vibrational transition, the hyperpolarizability becomes:

$$\beta_{lmn}(\omega_{sum}) =$$

$$-\frac{1}{2\hbar}\sum \left\{ \frac{<g|\mu_l|s><s|\mu_m|v>}{\hbar(\omega_{sum}-\omega_{sg})} - \frac{<g|\mu_m|s><s|\mu_l|v>}{\hbar(\omega_{vis}+\omega_{sg})} \right\} x \left\{ \frac{<v|\mu_n|g>}{\omega_{IR}-\omega_q+i\Gamma} \right\} \tag{1.31}$$

where $<g\,|$ is the ground state, $<v\,|$ is the excited state, $<s\,|$ is any other state, Γ is the relaxation time of the excited vibrational state and μ is the dipole operator. Equation 1.31 has a simple physical interoperation: the first term can be identified as a Raman dipole transition moment and the second term may be an infrared transition dipole moment. Therefore, in order for a molecular vibration to be SFG active, it must be both Raman and infrared active.

In general, the second order susceptibility is a twenty-seven-element tensor. Using symmetry for an in-plane isotropic surface, the second order susceptibility reduces to:

$$\chi_{zzz}^{(2)}; \chi_{xxz}^{(2)} = \chi_{yyz}^{(2)}; \chi_{xzx}^{(2)} = \chi_{yzy}^{(2)}; \chi_{zxx}^{(2)} = \chi_{zyy}^{(2)} \tag{1.32}$$

where z is the direction normal to the surface. Those four elements contribute to the sum frequency signal under four different polarization conditions, SSP, SPS, PSS and PPP where the polarizations are listed in order of deceasing frequency (sum, vis, IR). For P polarization, the electric field vector is parallel to the plane of incidence. In S polarization, the electric field vector is perpendicular to the plane of incidence. The vibrational modes present in the polarizations depend on the polarization of the infrared field and the direction of the infrared and Raman transition moments. Since metals are very reflective in the infrared, all of the fields in the x and y directions virtually cancel, while the fields in the z direction (azimuthal) constructively add. Due to this fact, the only polarizations available to metals are SSP and PPP. Another property of metals is that the electrons are free to conduct within the metals. This will give rise to an image of a dipole on the surface of the metal. An effect of this image dipole is that any vibrations parallel to the surface may cancel out the dipole of that

17

vibration. Meanwhile, vibrations perpendicular to the surface are reinforced by an

image dipole.
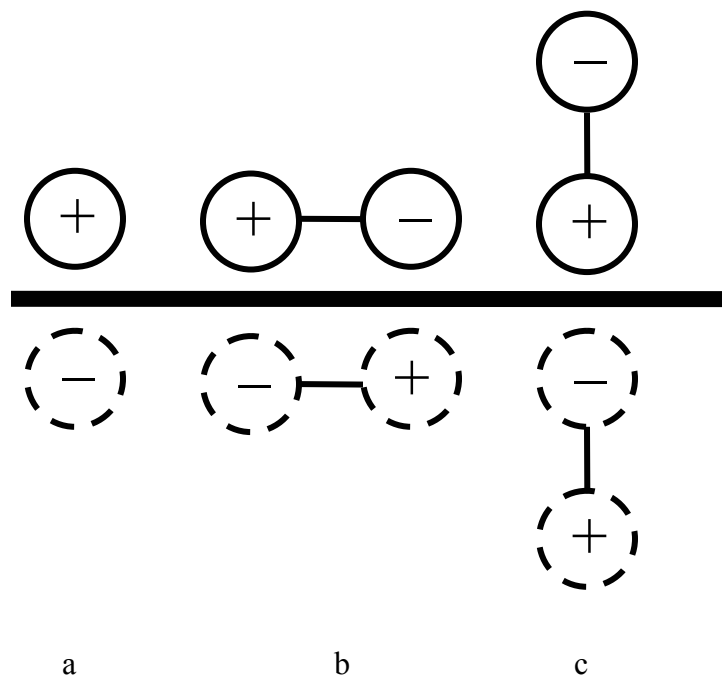
Figure 1.6 – Image dipoles. When a charge is at a surface then the metal will form an

image of that charge like for part a. Part b shows that a dipole parallel to the surface

will have an opposing image dipole, while a dipole normal to the surface will be

reinforced by its image dipole.

Ultrahigh vacuum/high-pressure system:

In the current project, ammonia synthesis is studied using single crystal model catalysis. The apparatus described in this section is used to provide a reproducible and well-defined surface. This surface can the be probed using SFG vibrational spectroscopy pressures up to an atmosphere.

The ultrahigh vacuum(UHV)/high-pressure system used in this study has been described previously[28, 29]. A schematic depicting the apparatus is described in Figure 1.7. Briefly, it is two level apparatus that allows for surface preparation and analysis in the upper UHV portion, base pressure 5×10^{-10} Torr, and the lower chamber allows high-pressure or vacuum SFG vibrational spectroscopy studies on the crystal surface. The UHV portion contained an ion bombardment gun for cleaning, three leak valves (two for dosing gasses and one to let in gasses from the reaction cell), an Auger electron spectrometer (AES)/low energy electron diffraction (LEED) apparatus, an ion gauge, a turbo molecular pump, an ion pump, a quadrupole mass spectrometer and a potassium getter source. To clean the sample, 3×10^{-5} Torr of Ar gas was leaked into the chamber and then the sample was bombarded with 1.5 kV Ar^{+} ions. If the surface of the iron crystal contains carbon, then the sample was resistively heated to 600 °C and ion bombarded with 1×10^{-7} Torr of oxygen and 3×10^{-5} Torr Ar in the chamber. After the sample was bombarded, the crystal was resistively heated to 500 °C for four minutes to anneal the sample. The surface cleanliness was then verified by AES. If the chamber had to be vented to atmosphere or if a high-pressure study had recently taken place, then the crystal would often need to be annealed for one to two hours at 500-600 °C before it was bombarded with ions.

The getter source was a six inch flange with two copper feed troughs welded by the center of the flange an inch apart where two copper supports were placed via set screw onto each of the feed troughs at a 45 degree angle. Three commercial potassium SAES getter filaments (SAES getters is the name of the company) were placed on these copper flanges with small copper c clamps to complete a circuit. The SAES getter filaments were about ten centimeters away from the crystal. The getters themselves are a metal boat containing potassium dichromate and an alloy of 16% aluminum, 84% zirconium. Upon heating, the Al-Zr alloy reduces the potassium dichromate and potassium metal is liberated. This potassium is then added to the iron surface. The amount of potassium added to the surface of the iron was calibrated by looking at the temperature programmed desorption (TPD) of the potassium on the iron crystal[30]. Leaving the three filaments to a current of 21 amperes allowed the deposition of about one-tenth of a monolayer every minute.

After the iron crystal was prepared in the UHV section of the apparatus, it could then be descended into the high-pressure cell by means of a hydraulic pump. Vacuum could be maintained in the UHV portion of the chamber up to 10 atmospheres of pressure in the high-pressure cell by means of a knife-edge on the sample holder and a vespel gasket between the two apparati. For the SFG experiments, the reaction cell was equipped with two calcium fluoride windows to allow infrared light to reach the sample. Infrared light intensity was also measured after the sample, so two calcium fluoride windows were necessary for the entering and exiting light.

The sample mount consisted of four feed troughs. Two of these feed troughs were the leads for a type K thermocouple that was spot welded to the top of the iron single crystal. The other two feed troughs were copper leads for the resistive heater. These copper leads are what the iron single crystal is actually mounted to. The cylindrical, copper leads had a flat section about a centimeter and a half long machined to them with two 2-56 tapped holes about a centimeter apart. The sample was mounted by first spot welding iron foil to the side of the crystal and then spot welding a section of the mounted foil to the 2-56 set screws protruding from the copper feed troughs. This allowed the sample to be mounted and provided electrical connections to the resistive heater.
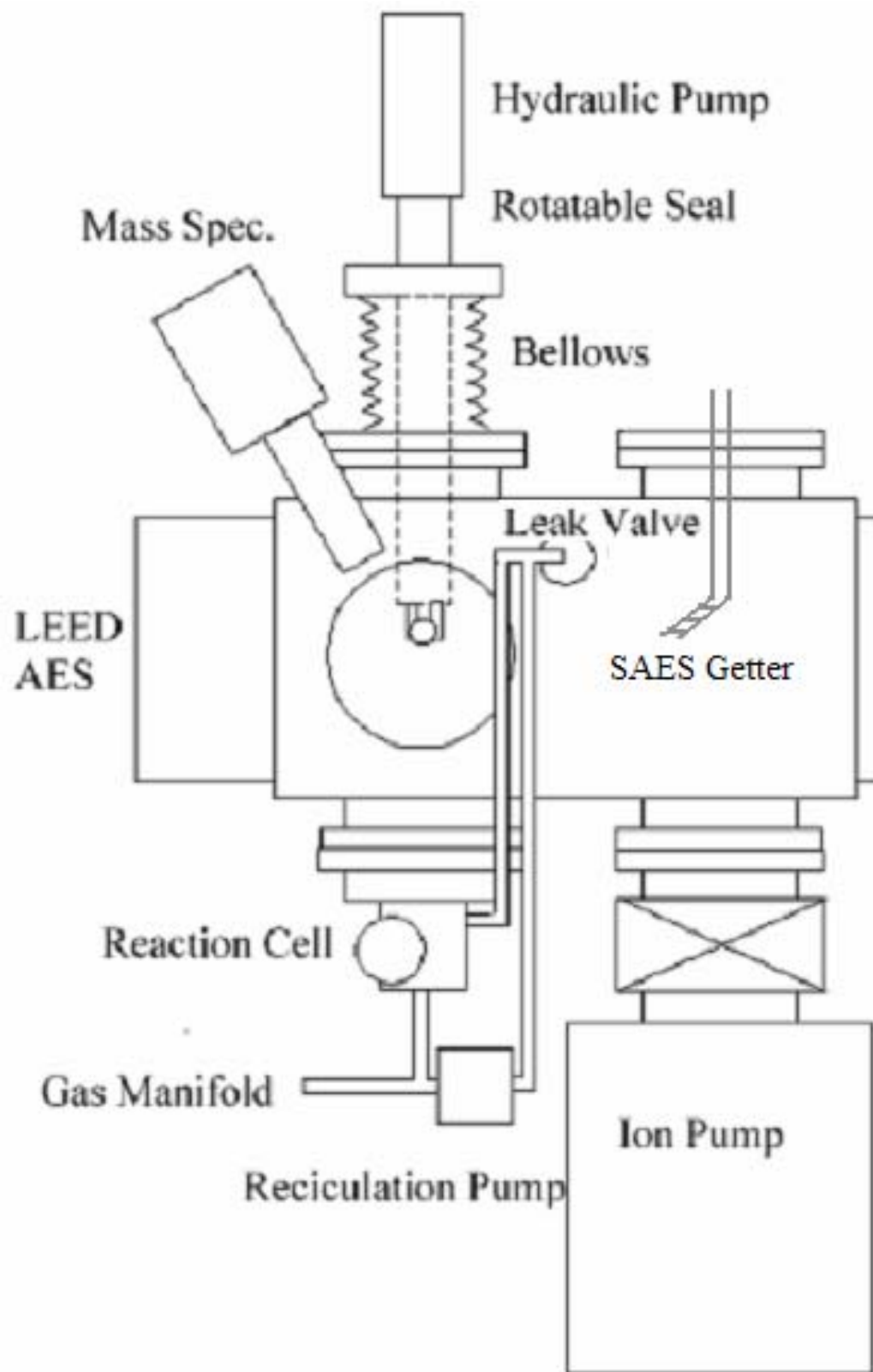
Figure 1.7 – UHV/High-pressure system.

References:

1.	Jennings, J.R., *Catalytic Ammonia Synthesis Fundamentals and Practice*. Fundamental and Applied Catalysis, ed. M.S.S. M. V. Twigg. 1991, New York: Plenum Press.

2.	Smil, V., *Detonator of the population explosion.* Nature, 1999. **400**: p. 415.

3.	Topham, S.A., *Catalysis, Science and Technology*, ed. M.B. John R. Anderson. Vol. 7. 1985, Berlin: Springer-Verlag.

4.	Crookes, W., *Report of the 68th meeting of the British Association for the Advancement of Science, Bristol, 1898*. 1898, London: John Murray.

5.	Goran, M., *The Story of Fritz Haber*. 1967, Oklahoma: University of Oaklahoma Press.

6.	Haber, F., Z. Elek., 1910. **16**: p. 244.

7.	Haber, F. and R.L. Rossignol, Z. Elek., 1913. **19**: p. 53.

8.	Mittasch, A., *Geschichte der Ammoniaksynthese*. 1951, Weinheim: Verlag Chemie.

9.	Partington, J.R. and L.H. Parker, *The Nitrogen Industry*. 1922, London: Constable.

10.	Brykowski, F.J., *Ammonia and Synthesis Gas Recent and Energy Saving Processes*. 1981, Park Ridge, NJ: Noyes Data Co.

11.	Strongin, D.R., S.R. Bare, and G.A. Somorjai, *The effects of aluminum oxide in restructuring iron single crystal surfaces for ammonia synthesis.* Journal of Catalysis, 1987. **103**(2): p. 289-301.

12.   Strongin, D.R. and G.A. Somorjai, *Effects of potassium on ammonia synthesis over iron single-crystal surfaces.* Journal of Catalysis, 1988. **109**(1): p. 51-60.

13.   Stoltze, P. and J.K. Norskov, *An interpretation of the high-pressure kinetics of ammonia synthesis based on a microscopic model.* Journal of Catalysis, 1988. **110**(1): p. 1-10.

14.   D. R. Strongin, J.C., Simon R. Bare, G.A. Somorjai, *The importance of C7 sites and Surface Roughness in the Ammonia Synthesis Reaction over Iron.* Journal of Catalysis, 1987. **103**: p. 213-215.

15.   M. Bass, P.A.F., A. E. Hill, C. W. Peters, and G. Weinreich, *Optical Mixing.* Physical Review Letters, 1962. **8**: p. 18.

16.   Bloembergen, N. and P.S. Pershan, *Light Waves at the Boundary of Nonlinear Media.* Physical Review, 1962. **128**(2): p. 606-622.

17.   J. H. Hunt, P.G.-S.a.Y.R.S., *Observation of C-H stretch vibrations of monolayers of molecules optical sum-frequency generation.* Chemical Physics Letters, 1986. **133**(3): p. 189-192.

18.   X. D. Zhu, H.S., and Y. R. Shen, *Surface vibrational spectroscopy by infrared-visible sum frequency generation.* Physical Review B, 1987. **35**(6): p. 3047-3050.

19.   A. L. Harris, C.E.D.C., N. J. Levinos and D. N. Loiacono, *Monolayer vibrational spectroscopy by infrared-visible sum generation at metal and semiconductor surfaces.* Chemical Physics Letters, 1987. **141**(4): p. 350-356.

20.   Shen, Y.R., *The Principles of Nonlinear Optics*. 1984, New York: Wiley.

21.   Shen, Y.R., *Surfaces probed by nonlinear optics.* Surface Science, 1994. **299-300**: p. 551-562.

22.   Lambert, A.G., P.B. Davies, and D.J. Neivandt, *Implementing the theory of sum frequency generation vibrational spectroscopy: A tutorial review.* Applied Spectroscopy Reviews, 2005. **40**(2): p. 103-145.

23.   Shen, Y.R., *Surface properties probed by second-harmonic and sum-frequency generation.* Nature, 1989. **337**: p. 519-525.

24.   Q. Du, R.S., E. Freysz, and Y. R. Shen, *Vibrational spectroscopy of water at the vapor/water interface.* Physical Review Letters, 1993. **70**(15): p. 2313-2316.

25.   Malkiat S. Johal, R.N.W., and Paul B. Davies, *Coadsorption of Tri-chain Surfactants and Dodecanol at a Hydrophobic Surface Studied by Sum-Frequency Spectroscopy.* Journal of Physical Chemistry, 1996. **100**(1): p. 274-279.

26.   John C. Conboy, M.C.M., and Geraldine L. Richmond, *Investigation of Surfactant Conformation and Order at the Liquid-Liquid Interface by Total Internal Reflection Sum-Frequency Vibrational Spectroscopy.* Journal of Physical Chemistry, 1996. **100**(18): p. 7617-7622.

27.   Buck, M. and M. Himmelhaus, *Vibrational spectroscopy of interfaces by infrared–visible sum frequency generation.* Journal of Vacuum Science & Technology A, 2001. **19**(6): p. 2717-2736.

28.   Westerberg, S., *Catalyzed Hydrogenation of Nitrogen and Ethylene on Metal (Fe, Pt) Single Crystal Surfaces and Effects of Coadsorption: a Sum*

Frequency Generation Vibrational Spectroscopy Study, in *Chemistry*. 2004, University of California: Berkeley.

29.   Staffan Westerberg, C.W., Keng Chou, Gabor Somorjai, *High-Pressure Ammonia Adsorption and Dissociation on Clean Fe(111) and Oxygen-Precovered Fe(111) Studied by Sum Frequency Generation Vibrational Spectroscopy.* The Journal of Physical Chemistry B, 2004. **108**: p. 6374-6380.

30.   S. B. Lee, M.W., and G. Ertl, *Adsorption of Potassium on Iron.* Surface Science, 1981. **108**: p. 357-367.

31.   Neumark, D.M., *Spectroscopy of reactive potential energy surfaces.* Phys. Chem. Comm., 2002. **5**(11): p. 76-81.

32.   Neumark, D.M., *Probing the transition state with negative ion photodetachment: experiment and theory.* Physical Chemistry Chemical Physics, 2005. **7**: p. 433-442.

33.   Neumark, D.M., *Transition State Spectroscopy.* Science, 1996. **272**: p. 1446-1447.

34.   Ho, K.-M., et al., *Structures of medium-sized silicon clusters.* Nature, 1998. **392**(6676): p. 582-585.

35.   Xu, C., et al., *Vibrationally resolved photoelectron spectroscopy of silicon cluster anions Sin (n = 3-7).* Journal of Chemical Physics, 1998. **108**(4): p. 1395-1406.

36.   Alivisatos, A.P., *Perspectives on the physical chemistry of semiconductor nanocrystals.* Journal of Physical Chemistry, 1996. **100**(31): p. 13226-13239.

37.   Asmis, K.R., T.R. Taylor, and D.M. Neumark, *Anion photoelectron spectroscopy of B2N-.* The Journal of Chemical Physics, 1999. **111**(19): p. 8838-8851.

38.   Asmis, K.R., T.R. Taylor, and D.M. Neumark, *Anion photoelectron spectroscopy of B3N-.* Journal of Chemical Physics, 1999. **111**(23): p. 10491-10500.

Chapter 2.   Studies of Fe(111) promoted surfaces

Introduction:

Since iron was found as a suitable catalyst for ammonia synthesis in the early twentieth century, much research into has been performed on the doubly promoted iron catalyst. After the advent of ultra-high vacuum (UHV) apparati in common scientific practice, the surface of the ammonia synthesis catalyst has been studied[1]. The surface science of the ammonia synthesis catalyst has been studied in the Somorjai laboratory using single crystals as model catalyst systems[2-6]. These studies helped to elucidate the promotion effect of the alumina to the catalyst and the reactivities of the different faces of an iron crystal to ammonia synthesis. Ertl and coworkers helped to identify the fundamental steps involved in ammonia synthesis on the iron catalyst[7-9] and Norskov and coworkers explored the promotion effect of potassium by theory[10] proving that potassium promoted the reaction due to electrostatic effects. Some infrared surface work by Nakata and coworkers also helped to shape our understanding of the system[11-13]. The model system was further explored when sum frequency generation (SFG) vibrational spectroscopy was used to probe the reaction intermediates[14]. Using SFG, the reactive intermediates can be studied *in situ* in high-pressure environments, approaching the conditions existing for the catalyst under industrial synthesis conditions (550 ºC and 100-200 atmospheres of pressure). The current study is on the effect of potassium and oxygen on the reactive intermediates of ammonia synthesis. In order to conduct this study, surfaces were prepared and exposed to 200 Torr of ammonia gas. These surfaces are

then compared to 200 Torr of ammonia on the Fe(111) surface. Some pressure effects of the ammonia on the promoted surface are also explored.

Experimental:

The UHV/high-pressure system used in this study has been described previously[14, 15]. Briefly, it is an UHV system combined with a high-pressure cell. The UHV part of the apparatus is used to clean and characterize the surface studied and then the sample is placed into a high-pressure cell where it is exposed to 200 Torr of ammonia gas. The sample is heated by means of a resistive heater. Temperature is measured by a type K thermocouple welded on top of the sample.

Potassium is added to the iron single crystal by a SAES getter source. The getter source allows a specific deposition of potassium. For this study, the potassium was added at two tenths of a monolayer to the iron surface. If the study included an oxidized surface, the surface was oxidized for ten minutes in the presence of 1×10^{-5} Torr O_2 gas. To cover the surface with nitrogen, the iron single crystal was exposed to 1×10^{-5} Torr of NH_3 gas for ten minutes and heated to 500 ℃. The formation of the surface to be studied is performed in the UHV portion of the chamber.

After the surface to be studied is prepared, the sample is placed into a high-pressure cell. The surface was probed by SFG vibrational spectroscopy. The two laser beams are generated in a Laservision OPG/OPA pumped by a 20 picosecond Nd:YAG Continuum Leopard. The infrared light is tunable from 2000 to 4000 cm^{-1} with a bandwidth of 7 cm^{-1}. The visible beam is 532 nm generated from a doubling crystal from a discarded 1064 nm laser beam from the OPG stage. The two laser beams are then overlapped in space and time on the Fe(111) single crystal. The sum

frequency light is then sent through a monochromator and collected via a photo multiplier tube connected to a gated integrator to ensure only the sum frequency light is detected. The infrared light is collected before and after the sample. The spectra are normalized by dividing the output voltage of the gated integrator by the square root of the infrared intensity before and after the high-pressure cell. The temperature may also be varied to explore the evolution of spectral features at different temperatures.

To aid in the analysis of the spectra, the data were fit with the following equation:

$$I(\omega_{sum}) \propto \left| \chi_{NR} + \sum_q \frac{A_q e^{i\vartheta_q}}{\omega_{IR} - \omega_q + i\Gamma_q} \right|^2 \qquad (2.1)$$

where χ_{NR} is the nonresonant contributions, A_q is the vibrational mode strength, Γ_q is the damping term and θ_q is the relative phase between the nonresonant contribution and the qth vibrational mode. The second part of equation 3.1 is maximized when the frequency of the incident infrared laser beam, ω_{IR}, matches a vibrational mode of a surface species, ω_q.

Results:

The main focus of the current study is probing the reactive intermediates for the ammonia synthesis reaction by SFG vibrational spectroscopy. The majority of the species on all surfaces studied are nitrogen and hydrogen atoms. Only about one or two percent of all surface sites are covered by the reactive intermediates[16]. Atomic nitrogen has surface vibrational frequencies of 500-1100 cm^{-1} depending on the bonding geometry, and hydrogen has a surface vibrational frequency of 1950 cm^{-1}. Both species have frequencies too low to probe with the current SFG setup. Another

factor that could make the reaction intermediates hard to detect with SFG is that if there is disordering at the surface. SFG vibrational spectroscopy presents an average of all the species probed in the area that the visible and infrared laser beams overlap. If there is no overall orientation at the surface, there will be no signal other than the nonresonant background. Also if the adsorbed species are tilted with respect to the surface normal, it may be difficult to detect the surface species with SFG vibrational spectroscopy due to the fact that the image dipole may cancel out the dipole at the surface.

The spectra for 200 Torr of ammonia on Fe(111) are presented in Figure 2.1. The observed spectral features are the NH stretch and NH_2 symmetric stretch and compare well with values reported in the literature. The NH_2 asymmetric stretch is not seen in the spectra and may be due to the image dipole from the surface of the iron canceling out the change in dipole that is parallel to the surface. For all of the spectra, there are valleys. This is due to the interference between the resonant contributions of the surface species and the large non-resonant background of iron from equation 2.1. The SFG spectra show two prominent features, two local minima corresponding to the NH and NH_2 symmetric stretching frequencies. The local minima of these two peaks are 3245 cm^{-1} for the NH stretch and 3330 cm^{-1} for the NH_2 symmetric stretch. Due to the interaction of the resonant and non-resonant nonlinear susceptibilities, it is difficult to exactly pinpoint where these modes are centered. The comparisons between the spectra will be made with the minima of these modes. The values of the surface intermediates correspond well with the reported values in the literature[11-13], although there is no evidence of the NH_2 asymmetric

31

stretch in the SFG spectra which may be explained by the rapid ammonia dissociation on the clean Fe(111) surface at room temperature[15] or from image dipole effects. The feature attributed to the NH stretch decreases at 50 ºC and completely disappears by 75 ºC. The feature attributed to the NH_2 symmetric stretch steadily decreases until it is no longer seen at 100 ºC.
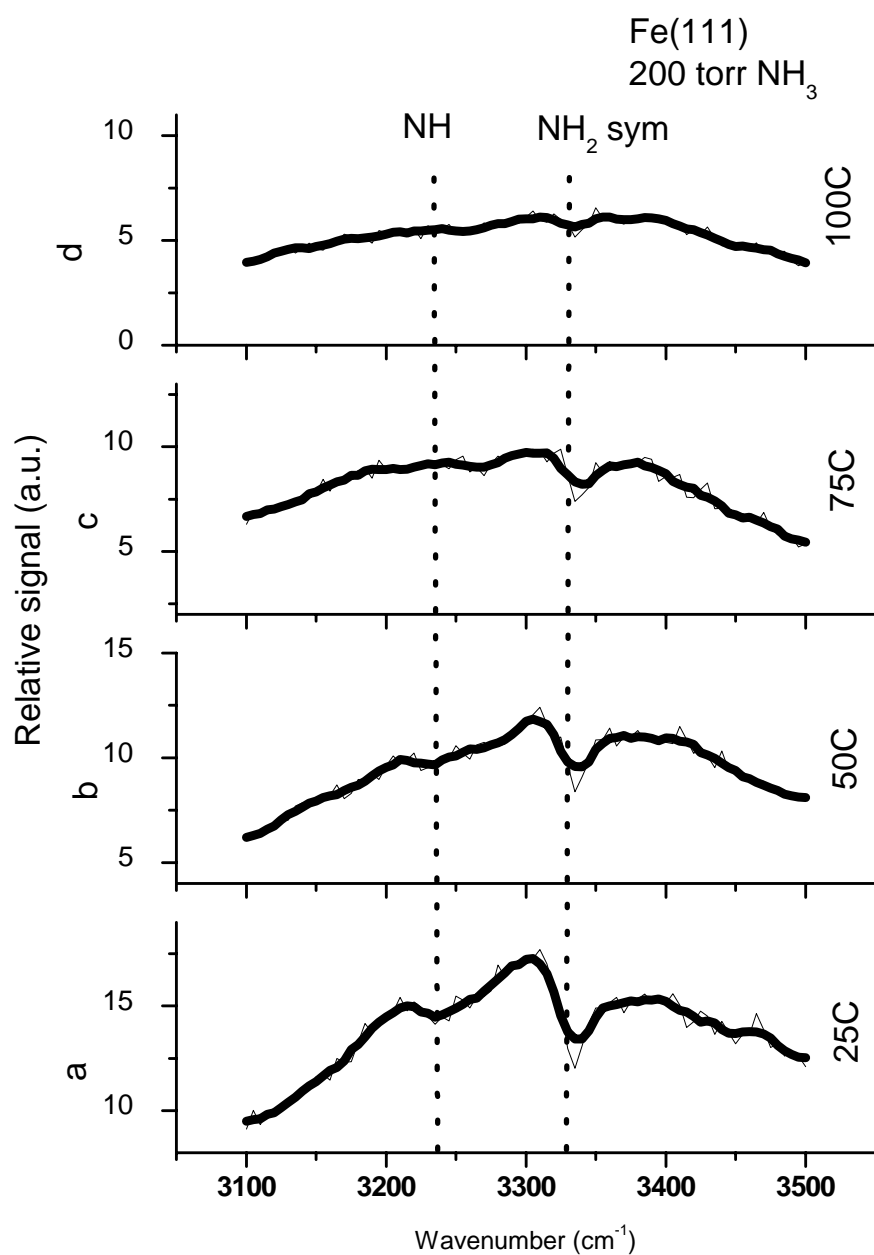
Figure 2.1 – Temperature dependant SFG spectra of 200 Torr ammonia on Fe(111).

Experimental data are shown with light lines and then smoothed to the darker line.

(a) 25 ºC, (b) 50 ºC, (c) 75 ºC, (d) 100 ºC.

A similar spectrum is shown for promoted iron in Figure 2.2. The order in which oxygen and potassium are added to the surface does not matter after ammonia is added. For Figure 2.2, the oxygen is added first, and then two tenths of a monolayer of potassium is added. The local minima of the two peaks are 3220 cm^{-1} for the NH stretch and 3305 cm^{-1} for the NH$_2$ symmetric stretch. The spectral features are retained for 25 ºC higher than for clean Fe(111). The pressure effects of ammonia gas are explored in Figure 2.3. Dosing the surface with ammonia (1 x 10^{-5} Torr ammonia) does not result in any features in the spectrum. At 20 Torr, a unique feature appears that does not appear in the other spectra. Then as the pressure increases, the NH stretch and the NH$_2$ symmetric stretch appears and the features just continue to become more sharp as the pressure is increased.

There may be some surface reconstruction after the ammonia is added to the surface explaining why the order of adding potassium and oxygen is irrelevant. Another interesting effect is that the signal for the Fe(111) surface that is first oxidized then promoted with potassium increases over time and levels off. To illustrate this, Figure 2.4 shows the signal at 3300 cm^{-1} for Fe(111) first oxidized, then promoted with two tenths of a monolayer of potassium exposed to 200 Torr of ammonia. The zero in time corresponds to when ammonia was added to the system. The SFG signal steadily increasing and then leveling off may be a sign of surface reconstruction.
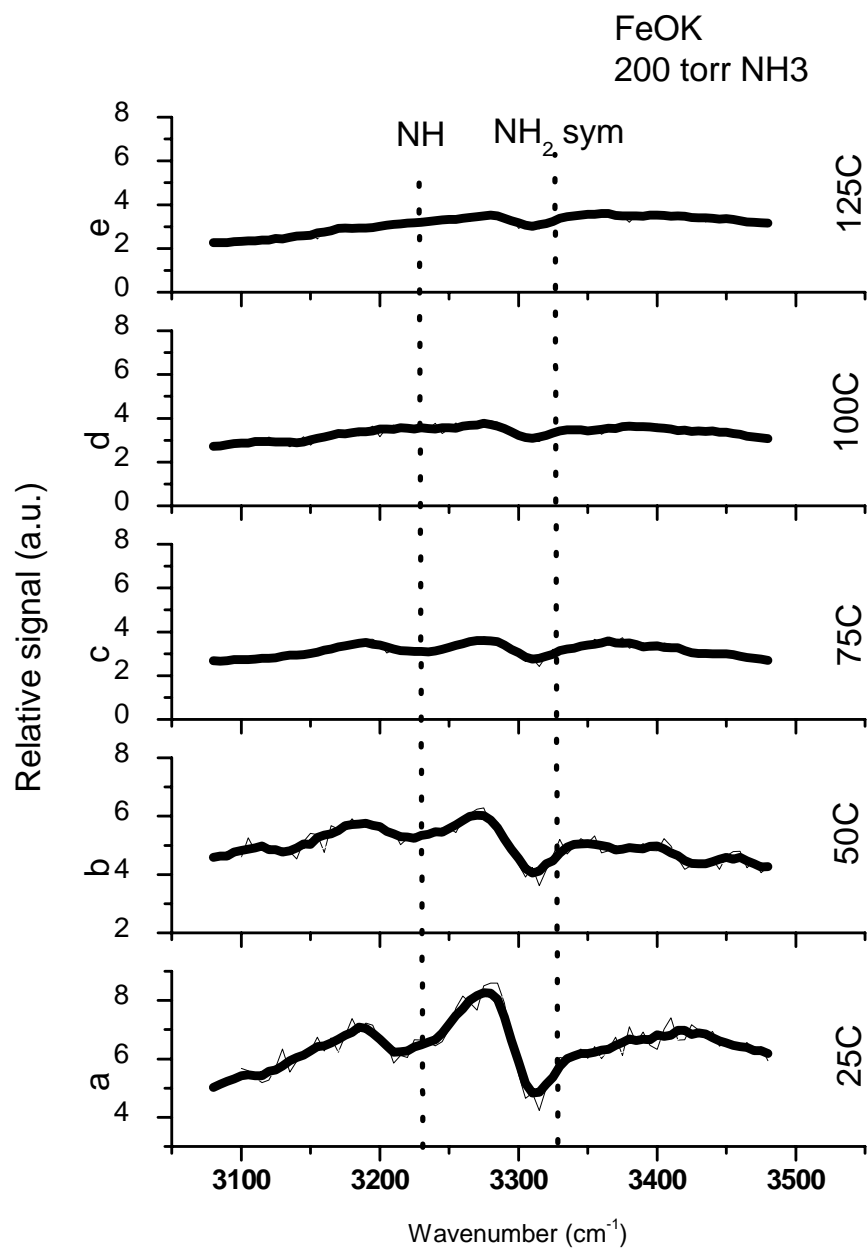
Figure 2.2 – Temperature dependant SFG spectra of 200 Torr ammonia on oxidized, promoted Fe(111). Experimental data are shown with light lines and then smoothed to the darker line. (a) 25 ºC, (b) 50 ºC, (c) 75 ºC, (d) 100 ºC, (e) 125 ºC.
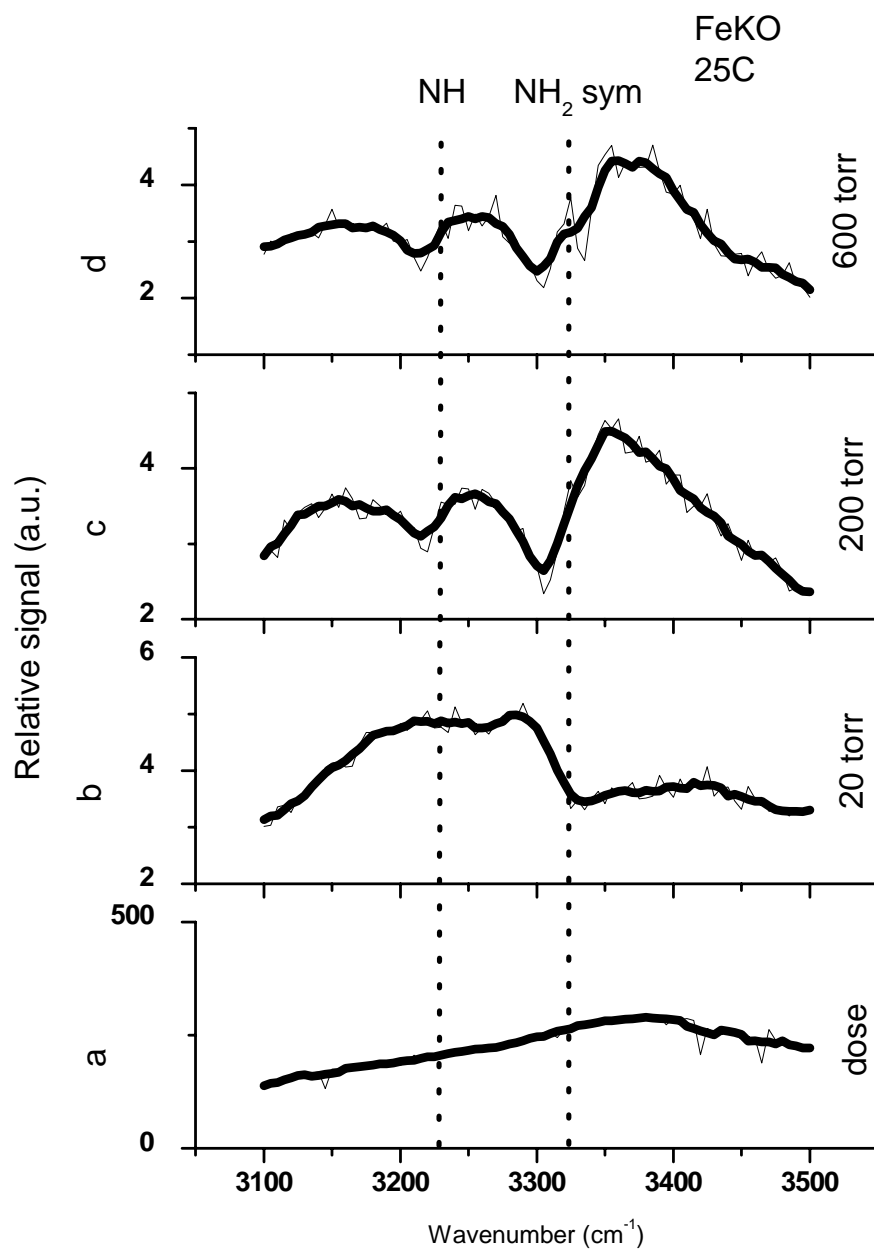
Figure 2.3 – Pressure dependant SFG spectra on oxidized, promoted Fe(111) at 25

°C. Experimental data are shown with light lines and then smoothed to the darker line.

(a) dose at 1×10^{-5} Torr ammonia, (b) 20 Torr ammonia,

(b) (c) 200 Torr ammonia, (d) 600 Torr ammonia.
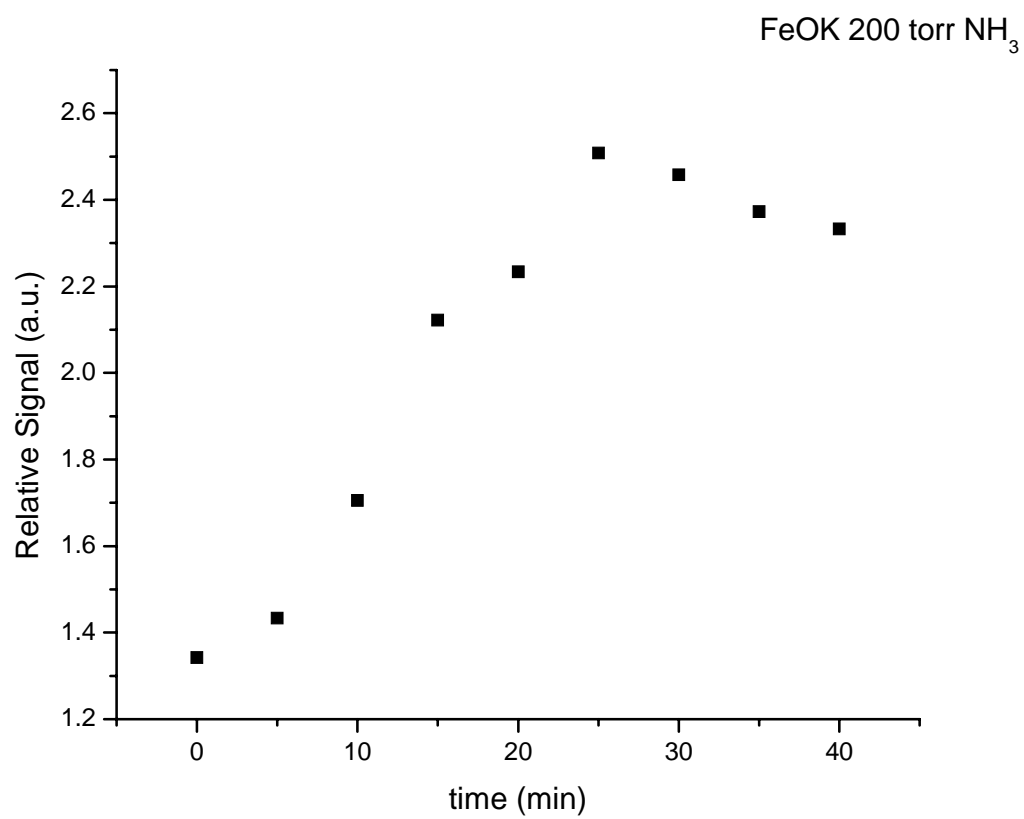
Figure 2.4 – Time dependant SFG signal at 3300 cm^{-1} for oxidized, promoted

Fe(111) surface at 25 °C.

With the previous study, it was found that when ammonia was co-adsorbed with oxygen, there was a phase shift relative to the clean Fe(111) of about 180 degrees[14]. This result was reproduced for the clean Fe(111) surface and the temperature effects of the spectral features are also explored. This phase inversion is visible by a peak appearing around 3400 cm^{-1} and persisting up to 75 ºC. No features are visible at 100 ºC for ammonia co adsorbed with oxygen. Figure 2.5 plots out the temperature dependant SFG spectra for 200 Torr ammonia co adsorbed with 0.5 Torr oxygen gas on clean Fe(111).

Similarly, ammonia was co-adsorbed with oxygen on the potassium promoted Fe(111) surface. The spectral features persist much longer for this surface. The NH stretch spectral feature persists to 75 ºC and the NH$_2$ symmetric stretch persists to 125 ºC. A phase inversion also is visible for the promoted surface as it was for the clean Fe(111). Figure 2.6 presents the temperature dependant SFG spectra for ammonia co adsorbed with 0.5 Torr oxygen gas on clean promoted, oxidized Fe(111).

An ammonia pretreated surface was also explored. The surface was first heated to 500 ºC and then exposed to 1 x 10^{-5} Torr of ammonia for ten minutes in the UHV portion of the apparatus. Auger electron spectroscopy (AES) to verified that nitrogen was on the surface of the Fe(111) single crystal. This ammonia-pretreated surface was then placed in the reaction cell and exposed to 200 Torr of ammonia gas. The temperature dependant SFG spectra for the ammonia-pretreated surface are shown in Figure 2.7. As the spectra evolve, a new feature at 3395 cm^{-1} starts to appear. The local minima of the two other modes are 3230 cm^{-1} for the NH stretch and 3310 cm^{-1} for the NH$_2$ symmetric stretch. Some data taken by Staffan Westerberg

38

is also presented in Figure 2.7. These data are of an SFG spectrum of ammonia on the

Fe(111) surface cooled to 210K and at an exposure of 10 Langmuirs of ammonia (one

Langmuir is 1 x 10^{-6} Torr of pressure per second)
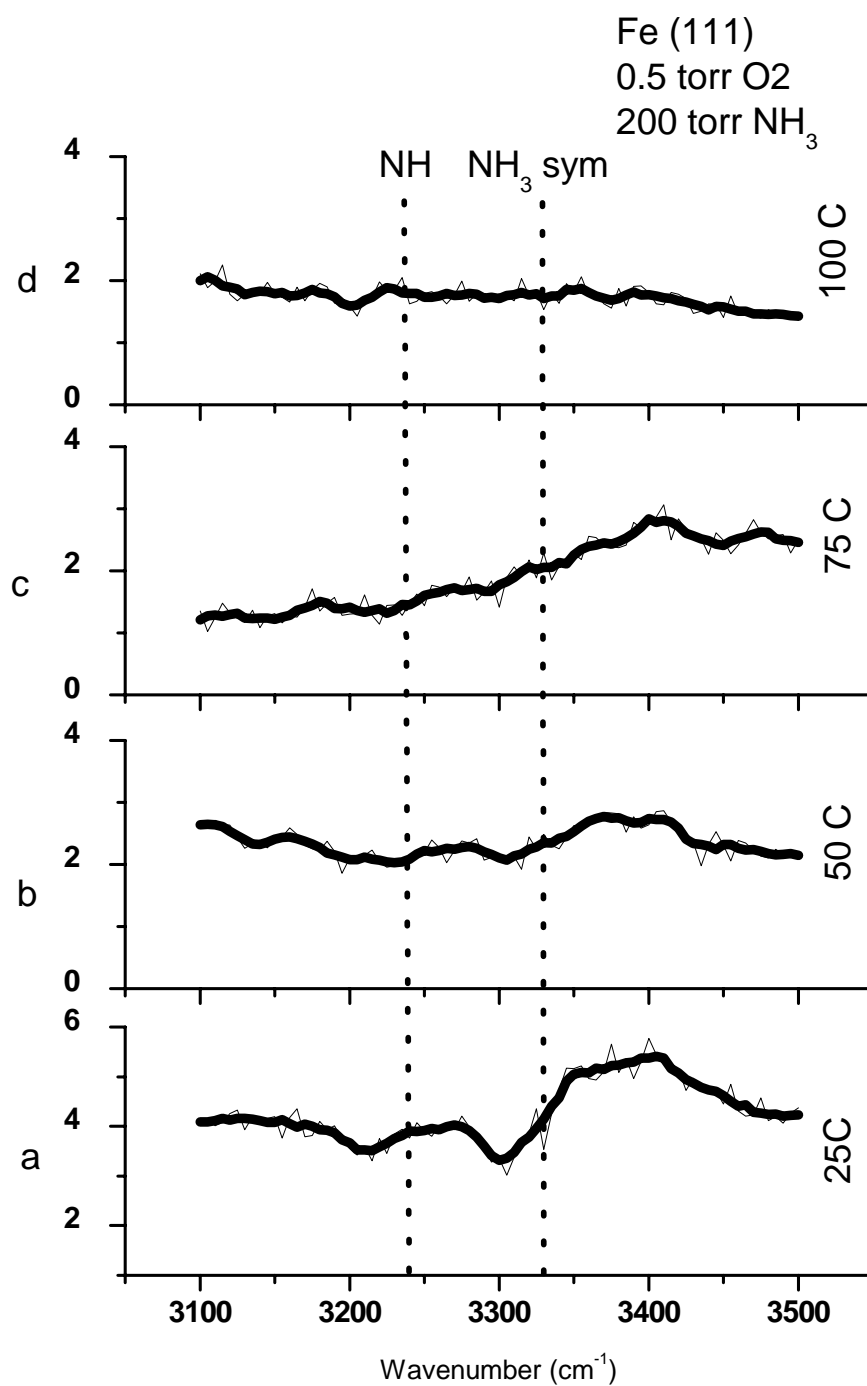
Figure 2.5 – Temperature dependant SFG spectra of 200 Torr ammonia co adsorbed

with 0.5 Torr oxygen gas on Fe(111). Experimental data are shown with light lines

and then smoothed to the darker line. (a) 25 ºC, (b) 50 ºC, (c) 75 ºC, (d) 100 ºC.
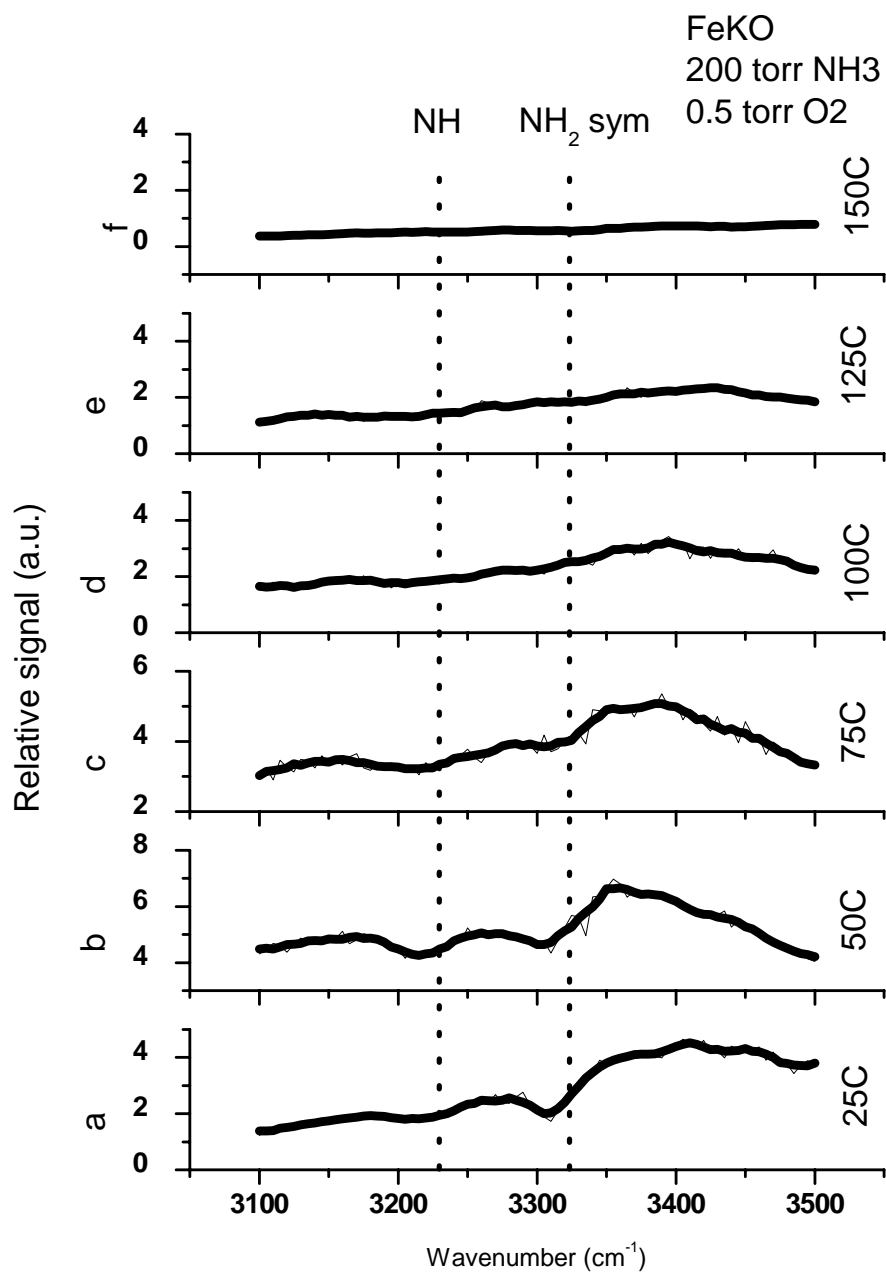
Figure 2.6 – Temperature dependant SFG spectra of 200 Torr ammonia co adsorbed

with 0.5 Torr oxygen gas on oxidized, promoted Fe(111). Experimental data are

shown with light lines and then smoothed to the darker line.

(a) 25 ºC, (b) 50 ºC, (c) 75 ºC, (d) 100 ºC.
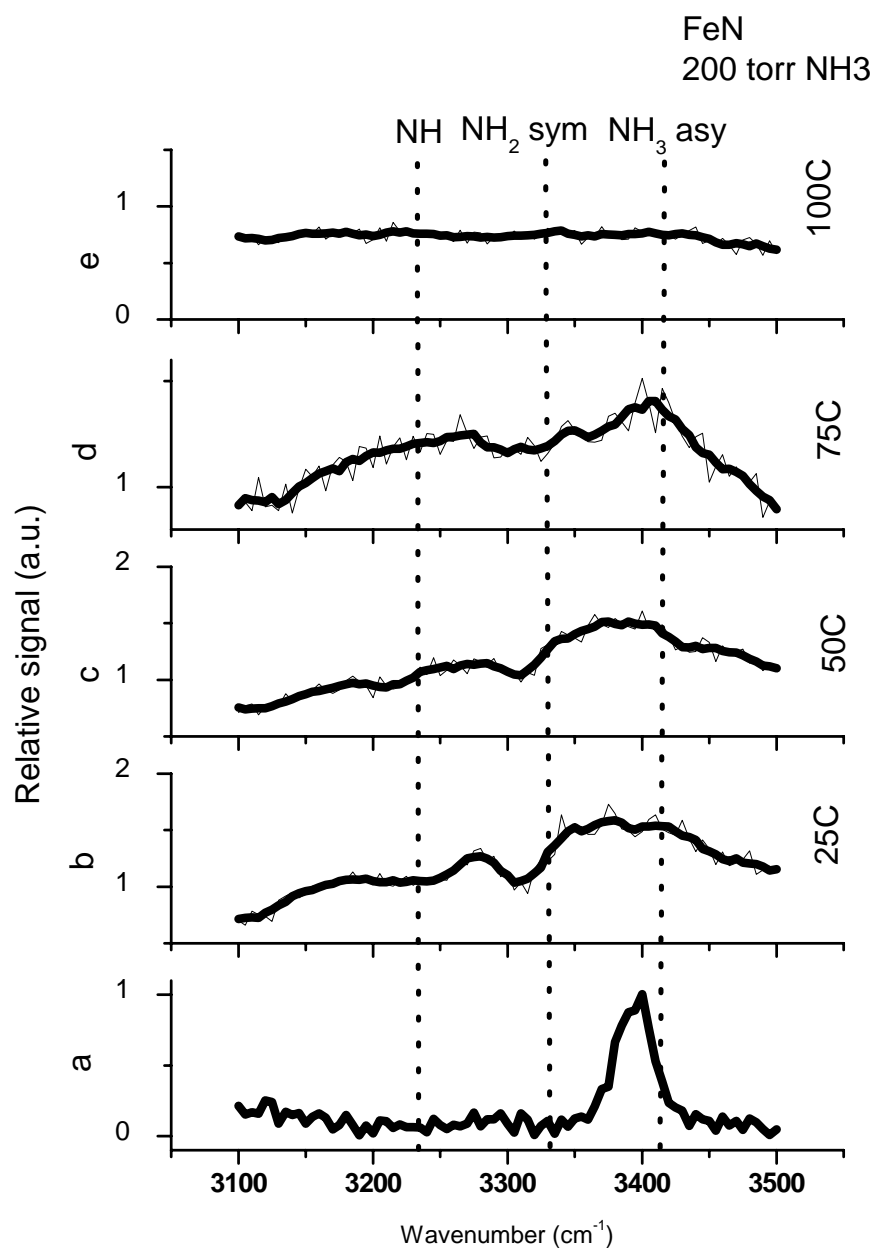
Figure 2.7 – Temperature dependant SFG spectra of 200 Torr ammonia on ammonia

pretreated Fe(111). Experimental data are shown with light lines and then smoothed

to the darker line. (a) Fe(111) at 210K exposed to 10 Langmuirs of ammonia,

(b) 25 ℃,(c) 50 ℃, (d) 75 ℃, (e) 100 ℃.

After the ammonia-pretreated surface was heated to 150 ºC, the surface was cooled to 25 ºC and another spectrum was taken. The spectrum taken after the heating is different than the spectrum taken prior to heating. There is no noticeable change in the NH stretching frequency, but the NH_2 symmetric stretch blue shifts 20 cm^{-1} in the cool down spectrum relative prior to heating. One possible explanation for this deals with the reversal of the reducing effects of ammonia to the iron surface. Figure 2.8 plots the spectra before and after heating.
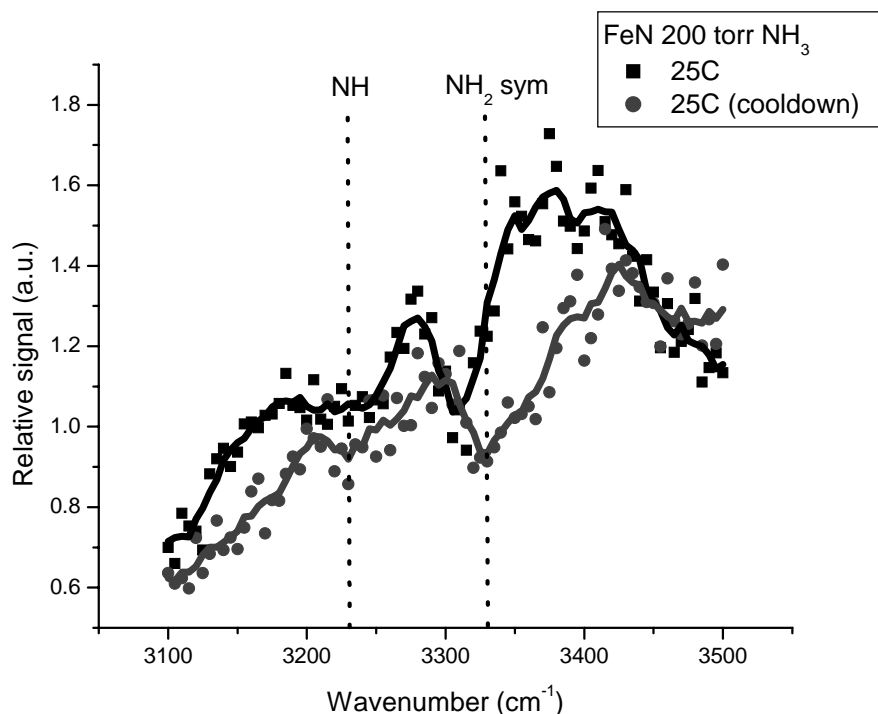
Figure 2.8 –SFG spectra of 200 Torr ammonia on ammonia treated Fe(111) at 25 ºC. Both before and after heating spectra are plotted together. Experimental data are shown with light lines and then smoothed to the darker line.

The SFG non-resonant background signal from the iron also changed dramatically when potassium was added to the surface. In general, the SFG background intensity increases as the surface is reduced and decreases when the surface is oxidized. Figure 2.9 shows the background intensities of the different iron surfaces relative to clean Fe(111). The surface with the highest background is Fe(111) with two tenths of a monolayer of potassium added. As different exposures of oxygen are added, first 20 Langmuir, then 100 and 1000, the signal steadily decreases until the surface is completely oxidized. The data were taken at 3300 cm^{-1} for the input infrared laser beam.
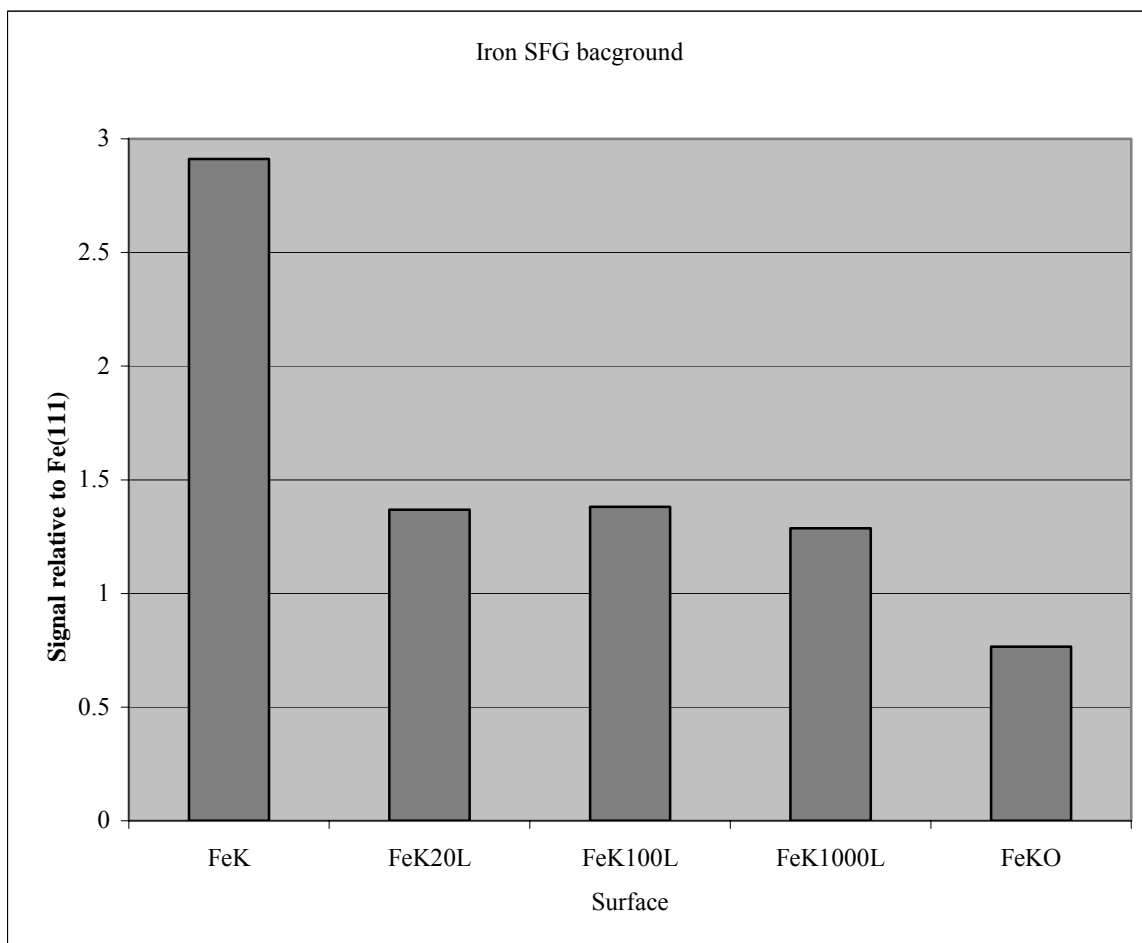
Figure 2.9 – Iron SFG background. The x axis describes the surfaces studied with exposures to oxygen in Langmuirs (L). The signal intensity is normalized to the background of clean Fe(111). FeK denotes Fe(111) promoted with potassium and FeKO denotes Fe(111) promoted with potassium oxidized.

Surface	NH	NH_2 sym
Fe(111)	3245 cm^{-1}	3330 cm^{-1}
FeOK	3220 cm^{-1}	3305 cm^{-1}
FeN	3230 cm^{-1}	3310 cm^{-1}
FeN(cool)	3230 cm^{-1}	3330 cm^{-1}
FecoO$_2$	3220 cm^{-1}	3310 cm^{-1}
FeKOcoO$_2$	3220 cm^{-1}	3310 cm^{-1}

Table 2.1 – Summary of SFG vibrational spectroscopy results.

Discussion:

When ammonia is adsorbed on all of the surfaces studied, it decomposes to NH and NH_2 reactive intermediates. The minima for the surface spectral features for all the surfaces studied are red shifted relative to clean Fe(111). Both the oxidized and reduced surfaces exhibit this red shift. This red shift leads us to conclude that the nitrogen and hydrogen bonds are weakened in the NH and NH_2 surface species for those surfaces. The Fe(111) surface pretreated with ammonia behaves differently. After the ammonia pretreated Fe(111) surface is heated to 100 ºC in the presence of 200 Torr ammonia and cooled down to room temperature, the HN$_2$ symmetric stretch blue shifts 20 cm^{-1}, but the NH stretch does not change after heating. Perhaps heating in high-pressure takes away some of the reduction of the surface by ammonia strengthening the hydrogen-nitrogen bonds in NH_2 resulting in a blue shift of the spectral feature. All of the spectra presented here are reversible, except the ammonia-pretreated surface, so heating and cooling the surface to the specified temperature will yield the same spectrum. If oxygen is included in the mix gas, then there is a phase shift in the spectrum for both the clean Fe(111) and promoted Fe(111) surfaces.

The order in which the oxygen and potassium are added does not matter on the promoted surface. Potassium will stick onto an oxidized Fe(111) surface and yield the same SFG vibrational spectrum as putting potassium on clean Fe(111) then oxidizing it. It seems that there is some surface restructuring after the ammonia is added, most prominent for the surface prepared by oxidizing clean Fe(111) then adding the potassium. Potassium will not stick to Fe(111) surfaces that have surface carbon or nitrogen atoms. The surface atoms were confirmed by AES.

On the promoted surfaces, the spectral features persist longer. As the temperature increases, the spectral features may leave due to either desorption or from disordering at the surface. The fact that more energy needs to be put into the system to either cause desorption or disorder show that the bond between the iron and the nitrogen atoms is stronger for both species on the promoted iron. A phase shift is also visible on promoted surfaces when oxygen gas is co adsorbed. The phase change is visible on both clean Fe(111) and the promoted surface.

The SFG vibrational spectroscopy is similar, but different than the work performed by Nakata and coworkers[11-13]. On the iron surface, Nakata and coworkers found NH, NH_2 symmetric and NH_2 asymmetric stretching frequencies of the reactive intermediates using infrared spectroscopy. For the surface infrared spectroscopy, the NH spectral became more visible as the temperature was increased to 150 ºC and decreased in intensity as the heating progressed; whereas, the SFG vibrational spectrum NH spectral feature was most intense at room temperature and decreased as the temperature was increased. In fact, no spectral features are seen at 150 ºC for the iron surface. This example shows the limitation of SFG vibrational

spectroscopy due to the fact that the sum frequency signal will both decrease by disorder of the surface species and from desorption of the surface species. For the NH spectral feature, it is clear that the sum frequency signal decreases from disorder because there is complimentary data on the relative amount of the NH intermediate on the surface. However, the decrease in signal intensity from the NH_2 reactive intermediate cannot be specifically determined because the infrared spectrum shows evidence of desorption. Also, the intensity of the sum frequency signal is fairly weak from the low coverage of surface intermediates. Taking that into consideration, combined with the fact that SFG is a second order nonlinear process, it is not surprising that the sum frequency signal decreases more rapidly than the infrared spectroscopy signal. Another limitation of the comparison is that Nakata and coworkers worked under low pressures. The pressure in the current study is much higher. As such, the surface may behave differently for the current study.

Unlike the other surfaces, the ammonia pretreated surface showed a growth of a spectral feature as the temperature was increased. This feature is most prevalent at 75 ºC. This feature is close to the asymmetric stretch of ammonia. Staffan Westerberg collected an SFG vibrational spectrum in 2003 of Fe(111) exposed to 20 Langmuirs of ammonia at 210K. Those data are presented in Figure 2.7 (a). The peak is centered around 3995 cm^{-1} and is close to the asymmetric stretch of ammonia. The NH_2 asymmetric stretch is not visible in the SFG vibrational spectrum because the change in dipole is in a plane horizontal to the surface. The metal surface will generate an image dipole that will cancel out the dipole from the NH_2 asymmetric stretch assuming that the molecule orients perpendicular to the surface. The NH_3 asymmetric

48

stretch does have a component in the change in the dipole moment that is perpendicular to the surface. This would then be further enhanced by an image dipole. The feature at 3995 cm^{-1} is then assigned to the asymmetric stretch of surface ammonia. The other surfaces: clean, promoted and oxidized Fe(111) do not contain any surface ammonia. The ammonia may appear at a higher temperature because the surface may need to open up vacancies. Clearly more experimentation is necessary to pinpoint exactly what is occurring on this surface. This surface is difficult to examine for promoted iron because if the iron were to be heated to 500 ºC, any potassium on the surface would desorb. Similarly, potassium will not stick to an Fe(111) surface with nitrogen atoms on it.

The non-resonant SFG background for the iron surface also changes when potassium is added to the surface. The SFG non-resonant background for metals can be in general related to the electronic structure of the metal and more specifically to the density of states of the electrons and the excitations of those electrons[17]. It was found in our previous study that the non-resonant signal for iron was related to how the surface substrate changed the work function of the metal surface[14]. Potassium was shown to decrease the work function of the surface of iron[18]. Potassium should then increase the SFG non-resonant background signal. The potassium promoted Fe(111) surface was then exposed to oxygen where the oxygen reacted at the surface and increased the work function. So the SFG non-resonant background signal should steadily decrease until it reaches a value where all the metal sites have been oxidized. This is exactly what happens in Figure 2.9. The potassium promoted Fe(111) surface has almost three times as much SFG non-resonant background signal as clean

49

Fe(111). After an exposure of twenty Langmuirs of oxygen, the SFG non-resonant

background signal decreases by about a half and steadily decreases until it is about

three-fourths as intense as clean Fe(111). The value for the SFG non-resonant

background signal for oxidized Fe(111) was found to be about one fourth of clean

Fe(111). This discrepancy between the SFG non-resonant background signals for

these two surfaces can again be explained in terms of the work function. The work

function for oxidized iron is higher than that of oxidized potassium promoted

iron[19]. So the potassium promoted Fe(111) surface behaves as expected by

increasing the SFG non-resonant background signal when the work function is

reduced by potassium and then steadily decreasing the SFG non-resonant background

signal as the surface is oxidized, increasing the work function.

Conclusions:

SFG vibrational spectroscopy has been used to study the temperature effects

of the clean Fe(111) and promoted Fe(111) surfaces in 200 Torr pure ammonia gas

and in 200 Torr ammonia gas with 0.5 Torr oxygen gas. Ammonia was found to

decompose on the surfaces and form the NH and NH_2 reactive intermediates. The

spectral features for these intermediates are red shifted on the promoted surface

indicating that the bonding between the nitrogen and hydrogen atoms is weakened.

The promoted surface also retained the spectral features at higher temperatures than

for the clean Fe(111) surface. The spectral features intensity decreases due to

desorption and/or disordering of the surface intermediates. The fact that the promoted

surfaces can retain the intermediate spectral features may indicate that the bonding

between the iron and nitrogen atoms is strengthened by the presence of potassium. No

surface ammonia was found on the clean Fe(111) or promoted iron surfaces in this study. Surface ammonia may be found on the Fe(111) surface pretreated with ammonia at higher temperatures. The iron non-resonant background signal behaved as expected by increasing when it was reduced by potassium and decreasing upon oxidation.

References:

1. Somorjai, G.A., *Introduction to Surface Chemistry and Catalysis*. 1994, New York: John Wiley & Sons Inc.

2. Spencer, N.D., R.C. Schoonmaker, and G.A. Somorjai, *Iron single crystals as ammonia synthesis catalysts: Effect of surface structure on catalyst activity.* Journal of Catalysis, 1982. **74**(1): p. 129-135.

3. Strongin, D.R., *Surface Science and Catalytic Studies on the Effects of Aluminum Oxide and Potassium on Ammonia Synthesis over Iron Single Crystal Surfaces*, in *Chemistry*. 1983, University of California: Berkeley.

4. Strongin, D.R., S.R. Bare, and G.A. Somorjai, *The effects of aluminum oxide in restructuring iron single crystal surfaces for ammonia synthesis.* Journal of Catalysis, 1987. **103**(2): p. 289-301.

5. Strongin, D.R., et al., *The importance of C7 sites and Surface Roughness in the Ammonia Synthesis Reaction over Iron.* Journal of Catalysis, 1987. **103**: p. 213-215.

6. Strongin, D.R. and G.A. Somorjai, *Effects of potassium on ammonia synthesis over iron single-crystal surfaces.* Journal of Catalysis, 1988. **109**(1): p. 51-60.

7. Ertl, G., et al., *Interactions of nitrogen and hydrogen on iron surfaces.* Surface Science, 1981. **8**(4): p. 373-386.

8. Ertl, G., S.B. Lee, and M. Weiss, *Kinetics of nitrogen adsorption on Fe(111).* Surface Science, 1982. **114**(2-3): p. 515-526.

9.   Ertl, G., S.B. Lee, and M. Weiss, *Adsorption of nitrogen on potassium promoted Fe(111) and (100) surfaces.* Surface Science, 1982. **114**(2-3): p. 527-545.

10.   Stoltze, P. and J.K. Norskov, *An interpretation of the high-pressure kinetics of ammonia synthesis based on a microscopic model.* Journal of Catalysis, 1988. **110**(1): p. 1-10.

11.   Nakata, T. and S. Matsushita, *The analysis of the surface reactions of ammonia synthesis on iron using infrared spectroscopy. II.* Journal of Chemical Physics, 1984. **76**(12): p. 6335-6341.

12.   Nakata, T. and S. Matsushita, *Infrared Studies of Intermediates of the Ammonia Synthesis on Iron.* Journal of Physical Chemistry, 1968. **72**(2): p. 458-464.

13.   Nakata, T., *The analysis of the surface reactions of ammonia synthesis on iron using infrared spectroscopy. I.* Journal of Chemical Physics, 1982. **76**(12): p. 6328-6334.

14.   Staffan Westerberg, C.W., Keng Chou, Gabor Somorjai, *High-Pressure Ammonia Adsorption and Dissociation on Clean Fe(111) and Oxygen-Precovered Fe(111) Studied by Sum Frequency Generation Vibrational Spectroscopy.* The Journal of Physical Chemistry B, 2004. **108**: p. 6374-6380.

15.   Westerberg, S., *Catalyzed Hydrogenation of Nitrogen and Ethylene on Metal (Fe, Pt) Single Crystal Surfaces and Effects of Coadsorption: a Sum Frequency Generation Vibrational Spectroscopy Study*, in *Chemistry*. 2004, University of California: Berkeley.

16.   Bowker, M., I. Parker, and K.C. Waugh, *The application of surface kinetic data to the industrial synthesis of ammonia.* Surface Science, 1988. **197**(1-2): p. L223-L229.

17.   Dreesen, L., et al., *Influence of the metal electronic properties on the sum-frequency generation spectra of dodecanethiol self-assembled monolayers on Pt (111), Ag (111) and Au (111) single crystals.* Applied Physics B: Lasers and Optics, 2002. **74**(7 - 8): p. 621-625.

18.   G.Broden and H.P. Bonzel, *Potassium Adsorption on Fe(110).* Surface Science, 1979. **84**: p. 106-120.

19.   Pirug, G., G. Broden, and H.P. Bonzel, *Coadsorption of potassium and oxygen on Fe(110).* Surface Science, 1980. **94**: p. 323-338.

Chapter 3.   Studies of promoted and unpromoted iron under equilibrium conditions

Introduction:

Iron has been used as the primary catalyst for ammonia synthesis since the early twentieth century. As a result of the common use of iron in ammonia synthesis, the role that iron plays in the reaction has been studied extensively[1]. Industrial conditions for ammonia synthesis include high pressure, tens to hundreds of atmospheres of pressure, and high temperature circa 500 ºC. Most of the studies done on the surfaces of the catalyst are done in ultra-high vacuum (UHV) and at low temperatures, so the analog to the catalyst in true industrial conditions may not be entirely accurate. The application of sum frequency generation (SFG) vibrational spectroscopy to model catalyst systems, like for ammonia synthesis, may help to elucidate the function of the catalyst under reaction conditions.

For most studies on the surface science of catalysts, electrons are used to probe the surfaces. These techniques such as Auger electron spectroscopy (AES), low energy electron diffraction (LEED), ultraviolet electron spectroscopy (UPS), x-ray electron spectroscopy (XPS), temperature programmed desorption (TPD) and high resolution electron energy loss spectroscopy (HREELS) have lead to a wealth of information. In particular to ammonia synthesis, Somorjai and coworkers[1-6], Ertl and coworkers[7-16] and King and coworkers[17, 18] have studied ammonia synthesis with those techniques. Those techniques have the drawback that as the background pressure of the study is increased, the mean free path of the electrons becomes increasingly small making studies at higher pressures much more difficult.

55

One way around this problem is to use photons instead of electrons as a probing media like in SFG vibrational spectroscopy. SFG vibrational spectroscopy has the ability to probe surfaces in more industrially applicable temperatures and pressures than available previously. Of particular interest is to see how the catalyst behaves in the environment of the synthesis conditions. Not just the temperature and pressure of the industrial synthesis, but at equilibrium concentrations of reactants and products.

In the previous chapter, the effects of specific surface adsorbates were studied. In this chapter, the iron catalyst is exposed to an equilibrium concentration mixture. Temperature dependent SFG spectra will be presented and the role of co adsorption of oxygen and the promoter effect of potassium will be discussed. The surfaces will be prepared in a UHV environment and then placed into a high-pressure cell where they will be probed by SFG vibrational spectroscopy.

Experimental:

The UHV/high-pressure system used in this study has been described previously[19, 20]. Briefly, it is an UHV system combined with a high-pressure cell. The UHV part of the apparatus is used to clean and characterize the surface studied and then the sample is placed into a high-pressure cell where it is exposed about an atmosphere of gas. The sample is heated by means of a resistive heater. Temperature is measured by a type K thermocouple welded on top of the sample.

Potassium is added to the iron single crystal by a SAES getter source. The getter source allows a specific deposition of potassium. For this study, the potassium was added at two tenths of a monolayer to the iron surface. If the study included an oxidized surface, the surface was oxidized for ten minutes in the presence of 1×10^{-5}

Torr O_2 gas. The formation of the surface to be studied is performed in the UHV portion of the chamber.

The conditions inside the reaction cell are used to approximate the reaction conditions during ammonia synthesis. Using thermodynamic data[21], the ratio the gasses ammonia to nitrogen to hydrogen was chosen to be 2:3:9 or 14% ammonia, 21% nitrogen and 65% hydrogen. The total pressure in the reaction cell was around 850 Torr.

After the surface to be studied is prepared, the sample is placed into a high-pressure cell. The surface was probed by SFG vibrational spectroscopy. The two laser beams are generated in a Laservision OPG/OPA pumped by a 20 picosecond Nd:YAG Continuum Leapard. The infrared light is tunable from 2000 to 4000 cm^{-1} with a bandwidth of 7 cm^{-1}. The visible beam is 532 nm generated from a doubling crystal from a discarded 1064 nm laser beam from the OPG stage. The two laser beams are then overlapped in space and time on the single crystal. The sum frequency light is then sent through a monochromator and collected via a photo multiplier tube connected to a gated integrator to ensure only the sum frequency light is detected. The infrared light is collected after the sample. The spectra are normalized by dividing the output voltage of the gated integrator by the square root of the infrared intensity before and after the high-pressure cell. The temperature may also be varied to explore the evolution of spectral features at different temperatures.

To aid in the analysis of the spectra, the data were fit with the following equation:

$$I(\omega_{sum}) \propto \left| \chi_{NR} + \sum_q \frac{A_q e^{i\vartheta_q}}{\omega_{IR} - \omega_q + i\Gamma_q} \right|^2 \qquad (3.1)$$

where χ_{NR} is the nonresonant contributions, A_q is the vibrational mode strength, Γ_q is the damping term and θ_q is the relative phase between the nonresonant contribution and the qth vibrational mode. The second part of equation 3.1 is maximized when frequency of the incident infrared laser beam, ω_{IR}, matches a vibrational mode of a surface species, ω_q.

Results:

The experiment is probing the reactive intermediates for the ammonia synthesis reaction. The majority of the species on all surfaces studied are nitrogen and hydrogen atoms. Only about one or two percent of all surface sites are covered by the reactive intermediates[22]. Atomic nitrogen has surface vibrational frequencies of 500-1100 cm^{-1} depending on the bonding geometry, and hydrogen has a surface vibrational frequency of 1950 cm^{-1}. Both species have frequencies too low to probe with the current SFG setup. Another factor that could make the reaction intermediates hard to detect with SFG is that if there is disordering at the surface. SFG vibrational spectroscopy presents an average of all the species probed in the area that the visible and infrared laser beams overlap. If there is no overall orientation at the surface, there will be no signal other than the nonresonant background. Also if the adsorbed species are tilted with respect to the surface normal, it may be difficult to detect the surface species with SFG vibrational spectroscopy due to the fact that the image dipole may cancel out the dipole at the surface.

The spectra for the equilibrium concentration of ammonia, nitrogen and hydrogen on clean Fe(111) is shown in Figure 3.1. The observed spectral features are the NH stretch and NH_2 symmetric stretch and compare well with values reported in the literature. The NH_2 asymmetric stretch is not seen in the spectra and may be due to the image dipole from the surface of the iron canceling out the change in dipole that is parallel to the surface. For all of the spectra, there are valleys. This is due to the interference between the resonant contributions of the surface species and the large non-resonant background of iron from equation 3.1. Similar to the previous study on the surface adsorbates, the spectra show two prominent features, one local minimum corresponding to the NH and NH_2 symmetric stretching frequencies. The local minima of these two peaks are 3220 cm^{-1} for the NH stretch and 3305 cm^{-1} for the NH_2 symmetric stretch. Due to the interaction of the resonant and non-resonant nonlinear susceptibilities, it is difficult to exactly pinpoint where these modes are centered. The comparisons between the spectra will be made with the minima of these modes. The values of the surface intermediates correspond well with the reported values in the literature[23-25], although there is no evidence of the NH_2 asymmetric stretch in the SFG spectra which may be explained by the rapid ammonia dissociation on the clean Fe(111) surface at room temperature[20].

In these spectra, the NH spectral feature is the one that persists to higher temperatures. The NH_2 spectral feature only exists at room temperature and disappears as the surface is heated to 50 ℃. The NH feature persists to 50 ℃, but disappears at 75 ℃. These spectra are also irreversible. After the surface is heated and then cooled, the spectral features do not return.

The promoted surface was also studied under equilibrium concentration conditions. These data are presented in Figure 3.2. The local minima for the NH stretch and the NH_2 symmetric are 3215 cm^{-1} and 3295 cm^{-1} respectively. The spectral features persist longer for the promoted surface. The NH stretch disappears at 75 ℃ as it did for clean Fe(111), but the NH_2 symmetric stretch persists to 75 ℃ and disappears at 100 ℃. The spectra are also not reversible as they were for clean Fe(111), but after the surface is cooled to both 50 ℃ and 25 ℃, the spectra look exactly the same. A broad spectral feature appears from about 3160 cm^{-1} to 3340 cm^{-1} in those spectra.

The promoted surface was also studied under the equilibrium concentration of reactants and products co adsorbed with 0.5 Torr of oxygen gas. The spectral features are similar to the promoted surface. The local minima for the NH stretch and the NH_2 symmetric are 3215 cm^{-1} and 3310 cm^{-1} respectively. There also the phase shift that was seen before when oxygen was co adsorbed with ammonia on the iron surface[26]. This phase inversion is visible by a peak appearing around 3400 cm^{-1}. The phase shift results in the appearance of peaks when valleys appeared for the other spectra. The NH stretch disappears at 75 ℃ and the NH_2 symmetric stretch disappears at 100 ℃. Unlike the other spectra, when the promoted surface is co adsorbed with oxygen the spectral features return when the surface is cooled.
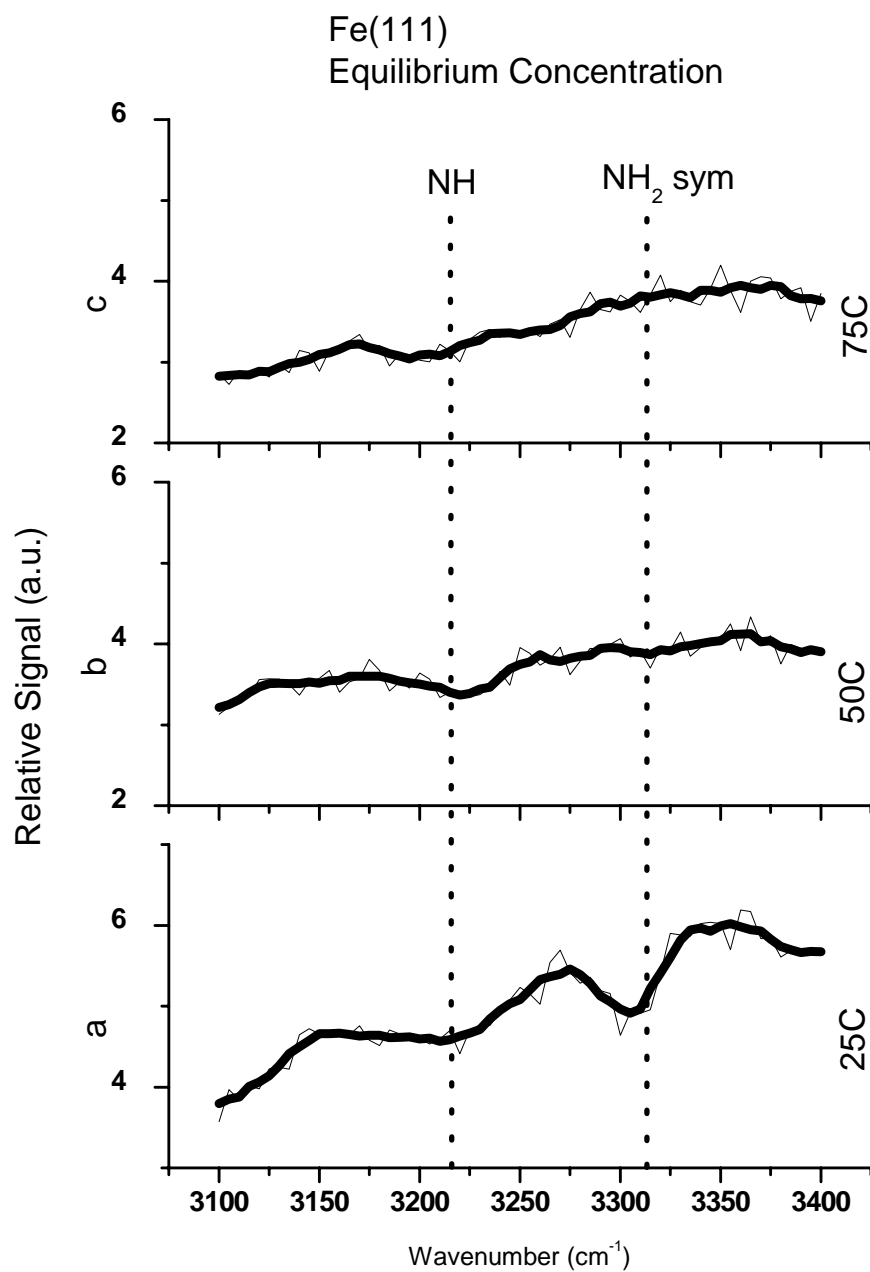
Figure 3.1 – Temperature dependant SFG spectra of an equilibrium concentration of reactants and products on Fe(111). Experimental data are shown with light lines and then smoothed to the darker line. (a) 25 ºC, (b) 50 ºC, (c) 75 ºC.

Figure 3.2 – Temperature dependant SFG spectra of an equilibrium concentration of reactants and products on oxidized and potassium promoted Fe(111). Experimental data are shown with light lines and then smoothed to the darker line. (a) 25 °C, (b) 50 °C, (c) 75 °C (d) 100 °C (e) spectrum after the surface is heated and then cooled down.
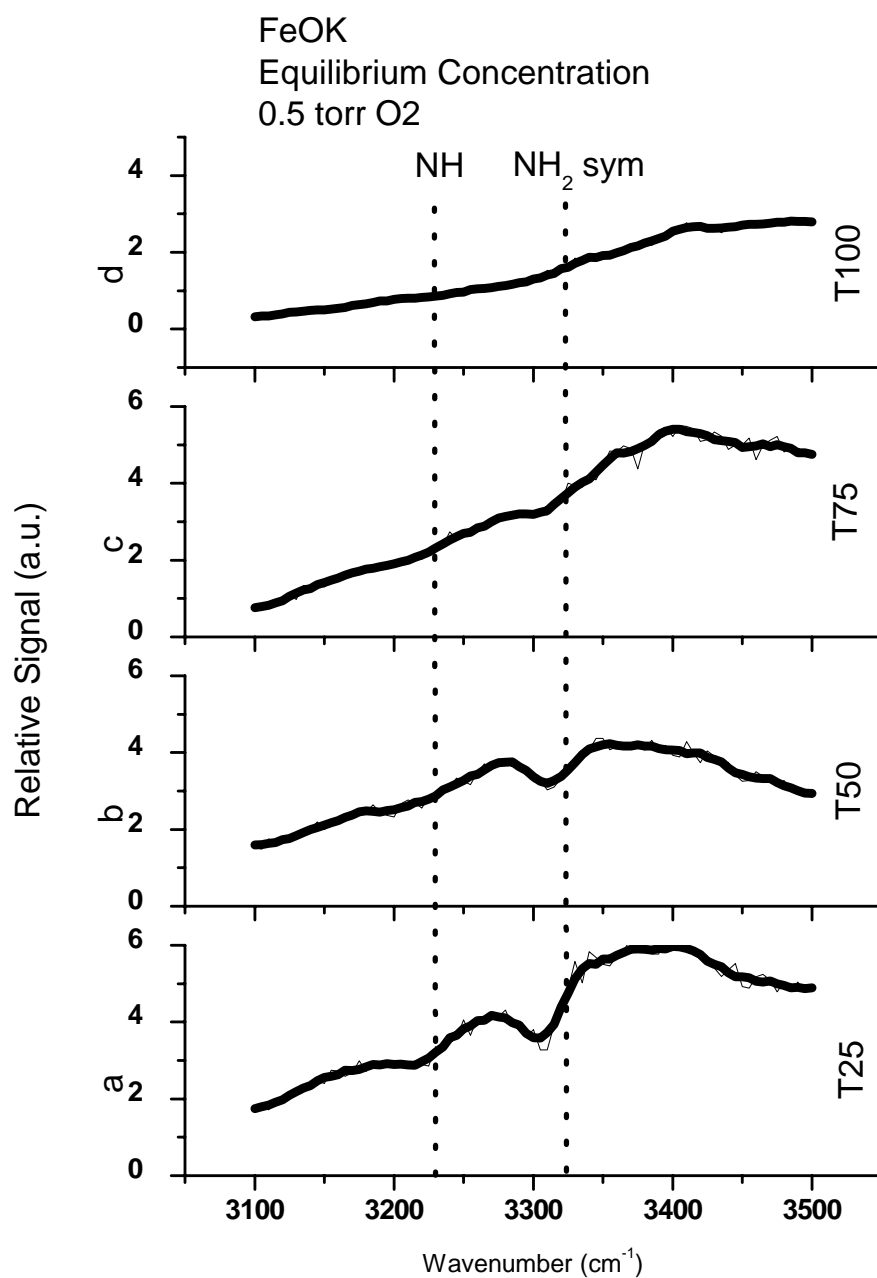
Figure 3.3 – Temperature dependant SFG spectra of an equilibrium concentration of reactants and products on oxidized and potassium promoted Fe(111) co adsorbed with oxygen. Experimental data are shown with light lines and then smoothed to the darker line. (a) 25 ºC, (b) 50 ºC, (c) 75 ºC (d) 100 ºC.

Discussion:

The most convenient way to analyze these spectra is to first compare them to the previous study where clean Fe(111) was placed in 200 Torr of ammonia gas. From the previous study of 200 Torr of ammonia on clean Fe(111), the NH stretching frequency is 3245 cm^{-1} and the NH$_2$ symmetric stretch is 3330 cm^{-1}. For the surfaces studied under equilibrium mixtures, both the NH and NH$_2$ symmetric stretching frequencies were red shifted. The covalent bond between the nitrogen and hydrogen atoms is weakened for these surfaces. For the clean Fe(111) exposed to equilibrium concentration, the values for the stretching frequencies are similar to that for the potassium promoted iron surface. The stretching frequencies most likely change because the Fe(111) surface is being reduced by the hydrogen, ammonia or both hydrogen and ammonia.

The promoted surface shifts the stretching frequencies even further. The stretching frequencies shift from either the surface being reduced or from electrostatic effects of the potassium. In the previous study, it was found that the stretching frequencies were red shifted when the Fe(111) surface was reduced by pretreating it with ammonia. Heating helped to reverse some of this effect. Similarly, the surface can be reduced by either hydrogen or ammonia, which may cause the red shifting of the stretching frequencies. The potassium may add even more electrons to the iron surface red shifting the frequencies even further. The promoter effect of the potassium is electrostatic in origin[27]. The electrostatic effect of the potassium may also cause the stretching frequencies to red shift. If the bonds red shift from the electrostatic effect of potassium, it will be similar to the effect potassium has on the

64

nitrogen triple bond. When oxygen is co adsorbed with the equilibrium mixture on the potassium promoted surface, the stretching frequencies blue shift 15 cm^{-1} for the NH_2 symmetric stretch spectral feature. The oxygen may oxidize the surface taking away some of the surface electrons that the potassium, ammonia and hydrogen added causing the nitrogen, hydrogen bond in the NH_2 reactive intermediate to strengthen and the NH_2 symmetric stretch to blue shift.

The behavior of the spectra upon heating is very different. For the clean Fe(111) surface, the NH spectral feature persists the longest, which is very unique to that system. For all the other systems, the NH_2 symmetric stretch spectral feature is the one that persists the longest. The SFG vibrational spectroscopy signal decreases from either disorder or desorption of the surface species. The signal of the reactive intermediates is already weak from the low concentration of the species on the surface. A small change in the ordering or in the amount adsorbed will greatly affect the signal. The fact that the NH spectral feature persists longer suggests that the NH intermediate is more stable than the NH_2 intermediate. For the potassium promoted surface, the NH_2 symmetric stretch spectral feature persists longer. Comparing the clean Fe(111) to the potassium promoted Fe(111) suggests that the bond between the iron and nitrogen atoms is stronger for the NH_2 reactive intermediate for the promoted surface. The spectra also suggest that the NH_2 reactive intermediate is more stable for the promoted surface.

The lack of reversibility of the spectra are also are of interest. After heating, no spectral features were visible for the clean Fe(111) surface exposed to the equilibrium mixture. Similarly for the potassium promoted surface, after cooling

down, the NH and NH_2 symmetric stretch spectral features did not return. A broad spectral feature did appear at 25 ºC and 50 ºC. A similar feature appeared in the similar study with the pressure affects of ammonia on the potassium promoted Fe(111) surface. At a lower pressure, 20 Torr, a similar broad spectral feature appeared. For the pressure study, as the pressure increased, the NH and NH_2 spectral features returned. For the promoted surface, the surface is different for the lower pressure. When ammonia is adsorbed on the potassium promoted surface, it decomposes. At lower pressures, nitrogen may control the surface chemistry cause this unique spectral feature. Similarly for the potassium promoted surface in the equilibrium concentration of reactants and products, this broad spectral feature may be from nitrogen. When oxygen is included in the equilibrium gas mixture, the reversibility of the spectra return. Perhaps oxygen is preventing some surface passivation by the nitrogen or some other species. Oxygen also causes a phase shift as was seen earlier[26]. The presence of oxygen in the mix gas clearly changes what is occurring on the potassium promoted surface. The fact that the spectral features return upon cooling shows that there is a process in equilibrium and the oxygen gas is a player in this process. Further experimentation may help to indicate exactly what role the gaseous oxygen play in the surface chemistry.

Conclusions:

SFG vibrational spectroscopy has been used to probe the clean Fe(111) and potassium promoted Fe(111) surfaces under an equilibrium concentration mixture of ammonia, nitrogen and hydrogen. Spectral features corresponding to the NH and NH_2 symmetric stretch were found on the surfaces studied. The values of the stretching

frequencies were found to be red shifted relative to earlier studies of ammonia on clean Fe(111) due to reduction on the surface by either ammonia or hydrogen. The presence of potassium on the surface helped to stabilize the NH_2 reactive intermediate by strengthening the iron, nitrogen bond. The spectra were reversible only after oxygen was included in the gas mixture. This oxygen then played a role in an equilibrium process preventing surface passivation and allowing the spectral features to return.

Summary:

The past two chapters have shown the experimental portion of this thesis on ammonia synthesis. In general, what was learned from this study is that potassium affects the reactive intermediates of ammonia synthesis by strengthening the iron-nitrogen bonds and weakening the nitrogen-hydrogen bonds. Ammonia may also cause the surface of the promoted catalyst to reconstruct. In the studies where the equilibrium concentrations of reactants and products are introduced into the high-pressure cell, the surface of the catalyst was reduced even more than for the studies introducing 200 Torr of ammonia into the high-pressure cell. Also for the equilibrium studies, co-adsorbing oxygen gas allowed the spectral features to return after heating.

What is left unanswered by these studies is the role of nitrogen in the ammonia synthesis. Some spectral features exist in low pressures that may indicate that nitrogen affects the reaction, but are not accurately explained. Further experimentation may be necessary to elucidate these results. Also, the surface reconstruction of the catalyst by ammonia is my interpretation of the data. This result would be better explained by a more structure-sensitive technique like high-pressure

STM. The role of water is also left unanswered for the system. The next chapter may help to explain how water may affect ammonia synthesis.

References:

1. Somorjai, G.A., *Introduction to Surface Chemistry and Catalysis*. 1994, New York: John Wiley & Sons Inc.

2. Spencer, N.D., R.C. Schoonmaker, and G.A. Somorjai, *Iron single crystals as ammonia synthesis catalysts: Effect of surface structure on catalyst activity.* Journal of Catalysis, 1982. **74**(1): p. 129-135.

3. Strongin, D.R., *Surface Science and Catalytic Studies on the Effects of Aluminum Oxide and Potassium on Ammonia Synthesis over Iron Single Crystal Surfaces*, in *Chemistry*. 1983, University of California: Berkeley.

4. Strongin, D.R., S.R. Bare, and G.A. Somorjai, *The effects of aluminum oxide in restructuring iron single crystal surfaces for ammonia synthesis.* Journal of Catalysis, 1987. **103**(2): p. 289-301.

5. Strongin, D.R., et al., *The importance of C7 sites and Surface Roughness in the Ammonia Synthesis Reaction over Iron.* Journal of Catalysis, 1987. **103**: p. 213-215.

6. Strongin, D.R. and G.A. Somorjai, *Effects of potassium on ammonia synthesis over iron single-crystal surfaces.* Journal of Catalysis, 1988. **109**(1): p. 51-60.

7. Bozso, F., G. Ertl, and M. Weiss, *Interaction of ammonia with Fe(111) and Fe(100) surfaces.* Applications of Surface Science, 1978. **1**(2): p. 241-265.

8. Grunze, M., et al., *Interaction of ammonia with Fe(111) and Fe(100) surfaces.* Applications of Surface Science, 1978. **1**(2): p. 241-265.

9. Ertl, G., et al., *Interactions of nitrogen and hydrogen on iron surfaces.* Surface Science, 1981. **8**(4): p. 373-386.

10.   Ertl, G., S.B. Lee, and M. Weiss, *The influence of potassium on the adsorption of hydrogen on iron.* Surface Science Letters, 1981. **111**(2): p. L711-L715.

11.   Lee, S.B., M. Weiss, and G. Ertl, *Adsorption of Potassium on Iron.* Surface Science, 1981. **108**: p. 357-367.

12.   Ertl, G., S.B. Lee, and M. Weiss, *Kinetics of nitrogen adsorption on Fe(111).* Surface Science, 1982. **114**(2-3): p. 515-526.

13.   Ertl, G., S.B. Lee, and M. Weiss, *Adsorption of nitrogen on potassium promoted Fe(111) and (100) surfaces.* Surface Science, 1982. **114**(2-3): p. 527-545.

14.   Tsai, M.C., et al., *A vibrational spectroscopy study on the interaction of N2 with clean and K-promoted Fe(111) surfaces: p-bonded dinitrogen as precursor for dissociation.* Surface Science, 1985. **155**(2-3): p. 387-399.

15.   Weiss, M., G. Ertl, and F. Nitschke, *Adsorption and decomposition of ammonia on Fe(110).* Applications of Surface Science, 1979. **2**(4): p. 614-635.

16.   Christmann, K. and G. Ertl, *Surface studies with bimetallic model catalyst systems.* Journal of Molecular Catalysis, 1984. **25**(1-3): p. 31-49.

17.   Escott, D.K., *Elementary steps in catalytic ammonia synthesis and decomposition on Fe{111}*, in *Chemistry*. 2003, Cambridge University: Cambridge.

18.   Escott, D.K., S.J. Pratt, and D.A. King, *Evidence for a nitrogen-induced reconstruction of Fe(1 1 1).* Surface Science, 2004. **562**(1-3): p. 226-236.

19.   Staffan Westerberg, C.W., Keng Chou, Gabor Somorjai, *High-Pressure Ammonia Adsorption and Dissociation on Clean Fe(111) and Oxygen-Precovered Fe(111) Studied by Sum Frequency Generation Vibrational Spectroscopy.* The Journal of Physical Chemistry B, 2004. **108**: p. 6374-6380.

20.   Westerberg, S., *Catalyzed Hydrogenation of Nitrogen and Ethylene on Metal (Fe, Pt) Single Crystal Surfaces and Effects of Coadsorption: a Sum Frequency Generation Vibrational Spectroscopy Study*, in *Chemistry*. 2004, University of California: Berkeley.

21.   Jennings, J.R., *Catalytic Ammonia Synthesis Fundamentals and Practice*. Fundamental and Applied Catalysis, ed. M.S.S. M. V. Twigg. 1991, New York: Plenum Press.

22.   Bowker, M., I. Parker, and K.C. Waugh, *The application of surface kinetic data to the industrial synthesis of ammonia.* Surface Science, 1988. **197**(1-2): p. L223-L229.

23.   Nakata, T. and S. Matsushita, *Infrared Studies of Intermediates of the Ammonia Synthesis on Iron.* Journal of Physical Chemistry, 1968. **72**(2): p. 458-464.

24.   Nakata, T., *The analysis of the surface reactions of ammonia synthesis on iron using infrared spectroscopy. I.* Journal of Chemical Physics, 1982. **76**(12): p. 6328-6334.

25.   Nakata, T. and S. Matsushita, *The analysis of the surface reactions of ammonia synthesis on iron using infrared spectroscopy. II.* Journal of Chemical Physics, 1984. **76**(12): p. 6335-6341.

26.	Westerberg, S., et al., *High-Pressure Ammonia Adsorption and Dissociation on Clean Fe(111) and Oxygen-Precovered Fe(111) Studied by Sum Frequency Generation Vibrational Spectroscopy.* The Journal of Physical Chemistry B, 2004. **108**: p. 6374-6380.

27.	Stoltze, P. and J.K. Norskov, *An interpretation of the high-pressure kinetics of ammonia synthesis based on a microscopic model.* Journal of Catalysis, 1988. **110**(1): p. 1-10.

Chapter 4. **Model catalysis study of the Fe(111) water interface by sum frequency generation vibrational spectroscopy**

Introduction:

Liquid water-solid interfaces are of great interest and importance since water is so abundant on our planet. In fact, about seventy percent of the earth's surface (i.e. lakes, rivers and oceans) is covered with water. Surface hydroxides are believed to play a central role in aqueous corrosion of iron and other 3d-metals[1] making more knowledge of the metal-water interface fruitful. The interface between mineral surfaces and water is of interest due to the vast number of water interfaces that exist. Many of these minerals in the earth's crust contain iron. Some of these minerals have been studied by infrared and Raman spectroscopy[2-8]. These studies have shed light into the hydroxide stretches both in the bulk material and on the surface. Sum frequency generation (SFG) vibrational spectroscopy has also been used to study water interfaces[9-19]. The SFG spectra of water interfaces have spectral features of water molecules interacting with each other and of hydroxyl stretches from free OH. A free OH is a hydroxyl group that does not engage in hydrogen bonding with another water molecule and signifies a hydrophobic surface.

Iron surfaces interacting with water have also been studied by ab initio local-spin-density functional calculations[20] and by electron energy loss spectroscopy (EELS)[21]. These studies found that water dissociates at low exposures for the Fe(100) and Fe(110) surfaces. The experimental studies are under low pressures and exposures of water. Using SFG, higher pressures can be probed than for the EELS study

73

The study presented in this chapter is an SFG vibrational spectroscopic study of H_2O and D_2O on the Fe(111) surface. This is for a model system of the interaction of water on an iron surface. The study uses an ultra-high vacuum (UHV) chamber connected to a high-pressure cell that allows a reproducible and well-characterized surface. The iron single crystal can also provide an analogue to corrosion studies by elucidating more of the interaction between water and an iron surface. Comparing the SFG spectra generated in this study to the spectroscopic data collected from the bulk minerals will also yield a better understanding of the interaction of water and iron in general.

Experimental:

The UHV/high-pressure system used in this study has been described previously[22, 23]. Briefly, it is an UHV system combined with a high-pressure cell. The UHV part of the apparatus is used to clean and characterize the surface studied. The sample is then placed into a high-pressure cell where it is exposed to 200 Torr of gas. The sample is heated by means of a resistive heater. Temperature is measured by a type K thermocouple welded on top of the sample. Water was incorporated on the Fe(111) surface by bubbling argon gas in light water or heavy water at 25 °C. The pressures of the gasses in the chamber are 23.7 Torr for H_2O and 20.5 Torr for D_2O combined with argon up to 200 Torr.

After the surface to be studied is prepared, the sample is placed into a high-pressure cell. The surface was probed by SFG vibrational spectroscopy. The two laser beams are generated in a Laservision OPG/OPA pumped by a 20 picosecond Nd:YAG Continuum Leopard. The infrared light is tunable from 2000 to 4000 cm^{-1}

with a bandwidth of 7 cm^{-1}. The visible beam is 532 nm generated from a doubling

crystal from a discarded 1064 nm laser beam from the OPG stage. The two laser

beams are then overlapped in space and time on the single crystal. The sum frequency

light is then sent through a monochromator and collected via a photo multiplier tube

connected to a gated integrator to ensure only the sum frequency light is detected.

The infrared light is collected after the sample. The spectra are normalized by

dividing the output voltage of the gated integrator by the square root of the infrared

intensity before and after the high-pressure cell. The temperature may also be varied

to explore the evolution of spectral features at different temperatures.

To aid in the analysis of the spectra, the data were fit with the following

equation:

$$I(\omega_{sum}) \propto \left| \chi_{NR} + \sum_q \frac{A_q e^{i\vartheta_q}}{\omega_{IR} - \omega_q + i\Gamma_q} \right|^2 \tag{4.1}$$

where χ_{NR} is the nonresonant contributions, A_q is the vibrational mode strength, Γ_q is

the damping term and θ_q is the relative phase between the nonresonant contribution

and the qth vibrational mode. The second part of equation 3.1 is maximized when the

frequency of the incident infrared laser beam, ω_{IR}, matches a vibrational mode of a

surface species, ω_q.

Results:

The data and the fit of the Fe(111) water system are presented in Figure 4.1.

The water peak is centered at 3690 cm^{-1} and is 70 cm^{-1} wide. There is a large spectral

feature centered at 3785 cm^{-1}. This feature is due to the large amount of infrared light

for that frequency. Figure 4.2 shows the infrared energy entering the high-pressure cell as a function of wavenumber.

To aid in the interoperation of the water study, a spectrum was taken with heavy water (D_2O). These data and corresponding fit are presented in Figure 4.3. The heavy water peak is centered at 2750 cm^{-1} and is 80 cm^{-1} wide. Since there is no similar spike in signal for the heavy water spectrum compared to the light water spectrum, the large spectral feature in the light water spectrum is attributed to the increase in infrared intensity for that spectral region. There is a decrease in signal for the heavy water spectrum from 2290-2385 cm^{-1}. This is due to adsorption of infrared intensity of ambient carbon dioxide.
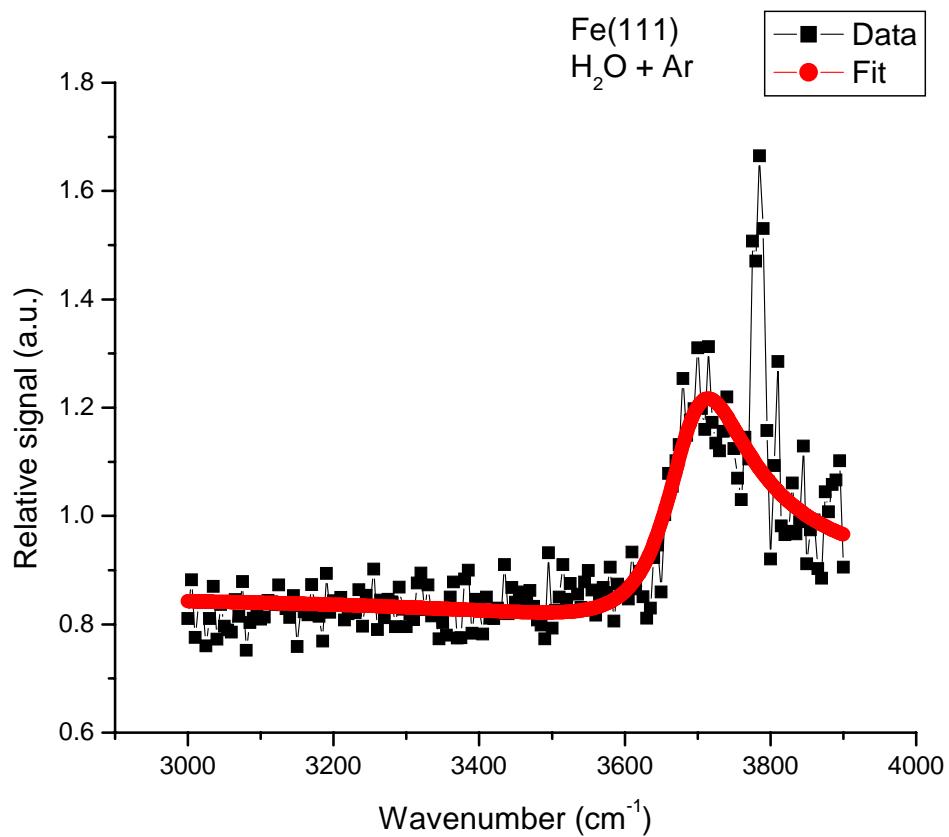
Figure 4.1 – SFG spectrum for 23.7 Torr of light water with background argon gas

on the Fe(111) surface. Both the data and the fit are presented.
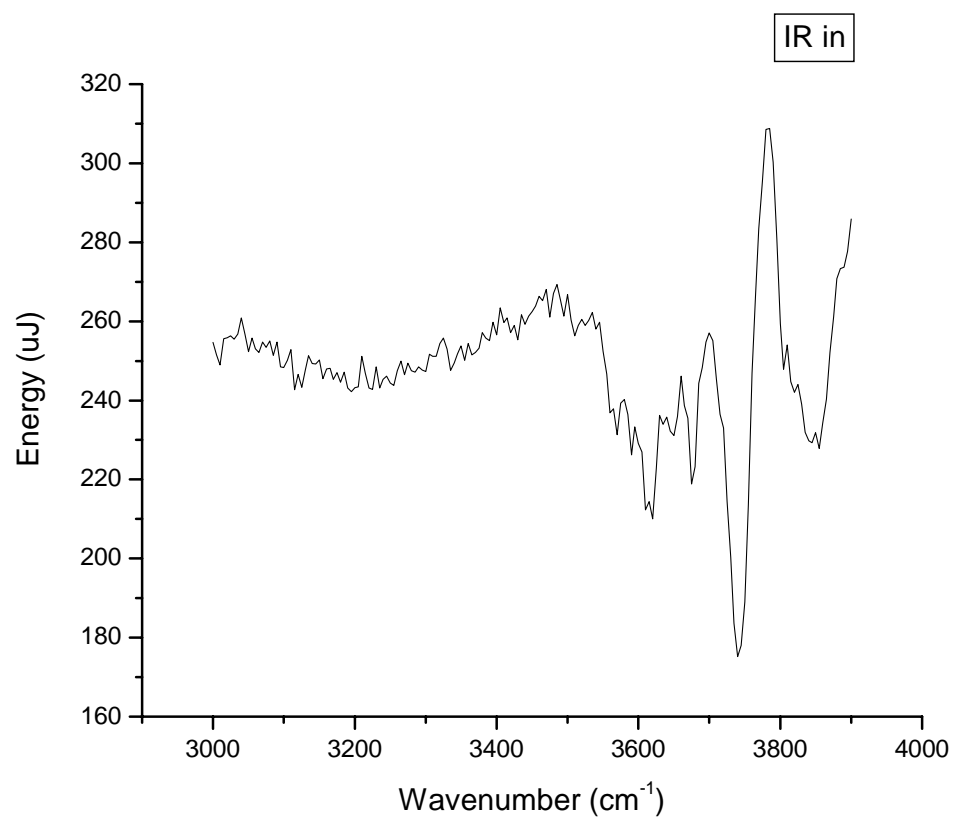
Figure 4.2 – Intensity of the input infrared light to the high-pressure cell.
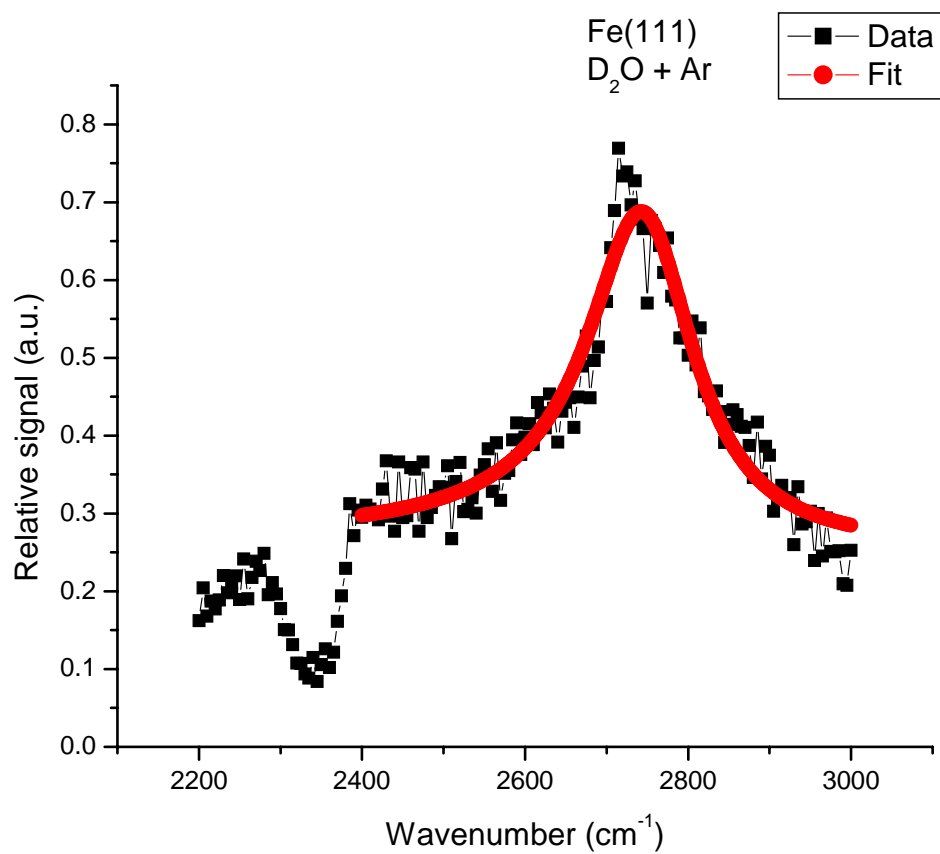
Figure 4.3 – SFG spectrum for 20.5 Torr of heavy water with background argon gas

on the Fe(111) surface. Both the data and the fit are presented.

Discussion:

The values for the spectral features for both the light and heavy water are similar to the free OH and free OD peaks corresponding to hydrophobic interfaces[9, 12, 15]. The main difference between the spectra in this study and the pervious SFG studies of water interfaces is that the current study lacks the spectral features corresponding to ice-like structure. The ice-like spectral features arise from interactions between the water molecules. It is possible that the iron surface may cause some of the ice-like spectral features to be decreased due to image effects. It is unlikely that the spectral features correspond to water monomers due to the fact the infrared spectrum of water monomers shows two features corresponding to the symmetric (3616 cm^{-1}) and asymmetric (3708 cm^{-1})[13, 15, 24, 25]. The current study shows only one spectral feature leading to the conclusion that water monomers are not responsible for the spectral features.

A more likely explanation of the physical interpretation of the SFG spectra is that surface hydroxides are being formed and are causing the spectral features. Iron is a reactive metal; it is used as a catalyst in ammonia synthesis and in Fisher-Tropsch synthesis. Under low exposures at low temperatures, water does dissociate to adsorbed H and OH species[20, 21]. Under high pressure, the interface may act similarly. FeOH has been studied using density functional theory[1]. The vibrational frequencies for the hydroxyl stretch were found to be 3735 cm^{-1} for the neutral species and 3702 cm^{-1} for the cation. These values are close to the spectral feature at 3690 cm^{-1} for the current study. The density functional calculations for a three atom system may not accurately describe the Fe(111) surface, which may account for the

values not being exact. SFG does not provide information of the charge of the adsorbed species. The iron and oxygen surface atoms could be of varying oxidation states. The mineral studies using infrared and Raman techniques have varying values for the hydroxide stretches reported[2-8]. The variation of hydroxides is due to in part because the different minerals studied have many different metal atoms nearby causing a range of hydroxide species. For instance Frost et al. [8] found bands centered at 3700, 3674 and 3626 cm^{-1} to be from hydroxide stretches of Mg_3OH, Mg_2FeOH and Fe_3OH respectively. This example illustrates how sensitive hydroxide stretches are to the electronic enviroment. The study performed by Frost et al. show that the spectral feature in the current study is range of iron hydroxide stretches. The Fe(111) surface initially has an oxidation number of zero. After the water is adsorbed, the oxidation number may change and the surface may restructure both of which may affect the hydroxyl stretch.

Conclusions:

SFG vibrational spectroscopy has been used to study the interaction of the Fe(111) surface with both light and heavy water. The SFG spectra that are generated show spectral features close to the free OH and free OD peaks assigned from previous SFG studies on hydrophobic surfaces. The current study shows no evidence of ice-like water structure also seen in water interface studies. This lack of the ice-like structure makes the formation of surface hydroxide groups a more plausible interpretation of the SFG spectra. Previous studies of minerals and theoretical calculations help support this conclusion.

The previous study on ammonia synthesis left the question of how water affects ammonia synthesis unanswered. This study shows that water does not cause the spectral features the previous spectra. Water was not included with the gas mixture introduced into the high-pressure cell for the studies of ammonia synthesis. That experiment may be fruitful to help elucidate the system more.

References:

1.   Gutsev, G.L., M.D. Mochena, and J. Bauschlicher, C.W., *Dissociative and associative attachment of OH to iron clusters.* Chemical Physics Letters, 2005. **407**(1-3): p. 180-185.

2.   Ruan, H.D., R.L. Frost, and J.T. Kloprogge, *The behavior of hydroxyl units of synthetic goethite and its dehydroxylated product hematite.* Spectrochimica Acta Part A: Molecular and Biomolecular Spectroscopy, 2001. **57**(13): p. 2575-2586.

3.   Ruan, H.D., et al., *Infrared spectroscopy of goethite dehydroxylation: III. FT-IR microscopy of in situ study of the thermal transformation of goethite to hematite.* Spectrochimica Acta Part A: Molecular and Biomolecular Spectroscopy, 2002. **58**(5): p. 967-981.

4.   Digne, M., et al., *Hydroxyl Groups on [gamma]-Alumina Surfaces: A DFT Study.* Journal of Catalysis, 2002. **211**(1): p. 1-5.

5.   Shoval, S., et al., *A Fifth OH-Stretching Band in IR Spectra of Kaolinites.* Journal of Colloid and Interface Science, 1999. **212**(2): p. 523-529.

6.   Farmer, V.C., *Transverse and longitudinal crystal modes associated with OH stretching vibrations in single crystals of kaolinite and dickite.* Spectrochimica Acta Part A: Molecular and Biomolecular Spectroscopy, 2000. **56**(5): p. 927-930.

7.   Morterra, C. and G. Magnacca, *A case study: surface chemistry and surface structure of catalytic aluminas, as studied by vibrational spectroscopy of adsorbed species.* Catalysis Today, 1996. **27**(3-4): p. 497-532.

8.   Frost, R.L., M.O. Adebajo, and K.L. Erickson, *Raman spectroscopy of synthetic and natural iowaite.* Spectrochimica Acta Part A: Molecular and Biomolecular Spectroscopy, 2005. **61**(4): p. 613-620.

9.   Du, Q., E. Freysz, and Y.R. Shen, *Surface Vibrational Spectroscopic Studies of Hydrogen Bonding and Hydrophobicity.* Science, 1994. **264**: p. 826-828.

10.   Du, Q., et al., *Vibrational spectroscopy of water at the vapor/water interface.* Physical Review Letters, 1993. **70**(15): p. 2313-2316.

11.   Uosaki, K., T. Yano, and S. Nihonyanagi, *Interfacial Water Structure at As-Prepared and UV-Induced Hydrophilic TiO₂ Surfaces Studied by Sum Frequency Generation Spectroscopy and Quartz Crystal Microbalance.* J. Phys. Chem. B, 2004. **108**(50): p. 19086-19088.

12.   Miranda, P.B., et al., *Icelike Water Monolayer Adsorbed on Mica at Room Temperature.* Physical Review Letters, 1998. **81**: p. 5876-5879.

13.   Scatena, L.F. and G.L. Richmond, *Orientation, Hydrogen Bonding, and Penetration of Water at the Organic/Water Interface.* J. Phys. Chem. B, 2001. **105**(45): p. 11240-11250.

14.   Scatena, L.F. and G.L. Richmond, *Aqueous solvation of charge at hydrophobic liquid surfaces.* Chemical Physics Letters, 2004. **383**(5-6): p. 491-495.

15.   Scatena, L.F., M.G. Brown, and G.L. Richmond, *Water at Hydrophobic Surfaces: Weak Hydrogen Bonding and Strong Orientation Effects.* Science, 2001. **292**(5518): p. 908-912.

16.   Conboy, J.C., M.C. Messmer, and G.L. Richmond, *Effect of Alkyl Chain Length on the Conformation and Order of Simple Ionic Surfactants Adsorbed at the D_2O/CCl_4 Interface as Studied by Sum-Frequency Vibrational Spectroscopy.* Langmuir, 1998. **14**(23): p. 6722-6727.

17.   Yeganeh, M.S., S.M. Dougal, and H.S. Pink, *Vibrational Spectroscopy of Water at Liquid/Solid Interfaces: Crossing the Isoelectric Point of a Solid Surface.* Physical Review Letters, 1999. **83**: p. 1179-1182.

18.   Ye, S., S. Nihonyanagi, and K. Uosaki, *Sum frequency generation (SFG) study of the pH-dependent water structure on a fused quartz surface modified by an octadecyltrichlorosilane (OTS) monolayer.* Physical Chemistry Chemical Physics, 2001. **3**: p. 3463-3469.

19.   Schnitzer, C., S. Baldelli, and M.J. Shultz, *Sum Frequency Generation of Water on NaCl, $NaNO_3$, $KHSO_4$, HCl, HNO_3, and H_2SO_4 Aqueous Solutions.* J. Phys. Chem. B, 2000. **104**(3): p. 585-590.

20.   Eder, M., K. Terakura, and J. Hafner, *Initial stages of oxidation of (100) and (110) surfaces of iron caused by water.* Phys. Rev. B, 2001. **64**: p. 115426-115432.

21.   Baro, A.M. and W. Erley, *The adsorption of H_2O on Fe(100) studied by EELS.* Journal of Vacuum Science and Technology, 1982. **20**(3): p. 580-583.

22.   Westerberg, S., *Catalyzed Hydrogenation of Nitrogen and Ethylene on Metal (Fe, Pt) Single Crystal Surfaces and Effects of Coadsorption: a Sum*

Frequency Generation Vibrational Spectroscopy Study, in *Chemistry*. 2004, University of California: Berkeley.

23. Westerberg, S., et al., *High-Pressure Ammonia Adsorption and Dissociation on Clean Fe(111) and Oxygen-Precovered Fe(111) Studied by Sum Frequency Generation Vibrational Spectroscopy.* The Journal of Physical Chemistry B, 2004. **108**: p. 6374-6380.

24. Page, R.H., et al., *Infrared predissociation spectra of water dimer in a supersonic molecular beam.* Chemical Physics Letters, 1984. **106**(5): p. 373-376.

25. Coker, D.F., R.E. Miller, and R.O. Watts, *The infrared predissociation spectra of water clusters.* The Journal of Chemical Physics, 1985. **82**(8): p. 3554-3562.

Chapter 5.   Introduction – Anion photoelectron spectroscopic study of selected anion clusters

Preface:

This thesis also contains some projects I worked on when I was in Professor Daniel M. Neumark's research group for my first three years of graduate school. The technique used was anion photoelectron spectroscopy (PES). Anion PES is a very powerful technique that allows for very short-lived species like transition states to be probed. Unlike the previous chapters, my research in the Neumark group covered only material in the gas phase. There were two main focuses in the laboratory I worked in: one dealing with short-lived complexes like van der Waals wells and the other dealing with how semiconductor clusters evolved as a function of size. This introductory chapter into the work in the Neumark group starts with an explanation of the technique used. The scope of the projects and a description of the experiment follow.

Anion photoelectron spectroscopy:

Anion PES is a technique that combines laser spectroscopy with anion molecular beams. An anion is selected and then photodetached with a laser and the generated photoelectrons are collected. The photoelectrons are then analyzed for their energy. PES probes the neutral potential energy surface, more specifically the Franc-Condon overlap of the anion and neutral wave functions. The most powerful feature of the technique is that short-lived species, like transition states and van der Waals wells, may be probed[1-3]. Transition states often occur at the saddle points of potential energy surfaces and as such experimentation on them proves very difficult.

Through anion PES, the transition state of certain reactions may be directly probed gaining a better understanding of the potential energy surface. The properties of the transition state determine the reactivity of a chemical reaction as well as many more detailed attributes one measured in scattering experiments. These facts have made probing the transition state an important challenge in chemistry[3].

Figure 5.1 illustrates the photodetachment process for the anion. The photoelectron spectra are analyzed by means of Koopman's theorem which states the energy of the ejected photoelectron is the energy of the orbital it was bound. The signal of an anion PES is determined by the Franc-Condon overlap between the anion and neutral wave functions. The information gathered from a photoelectron spectrum may yield electron affinities and vibrational progressions. Simulating the spectra may also indirectly yield information of the geometry and symmetry of the molecule. If the anion is in an excited electronic state, excited vibrational state or in a higher-energy state, the result would appear as hot bands in the anion photoelectron spectrum.

In order for a system to be studied using anion PES, the anion has to be stable and the neutral species of interest needs to have good Franc-Condon overlap with the anion. The technique works by the fact that the photodetachment process is much faster than the movement of atoms within the cluster. The neutral cluster can then be in one of the available energy states. The energy of the photoelectron is described by equation 5.1:

$$eKE = h\nu - EA - T_0 - E_v^0 + E_v^- \tag{5.1}$$

where hv is the energy of the photons in the probe laser, EA is the electron affinity of the anion, T_0 is the term value of the various electronic states, E_v^0 is the vibrational energy state of the neutral species and E_v^- is the vibration energy state of the anion. Often time the photoelectron spectra are presented in terms of electron binding energy (eBE) instead of eKE. The two are related by equation 5.2.

$$eKE = hv - eBE \qquad\qquad (5.2)$$
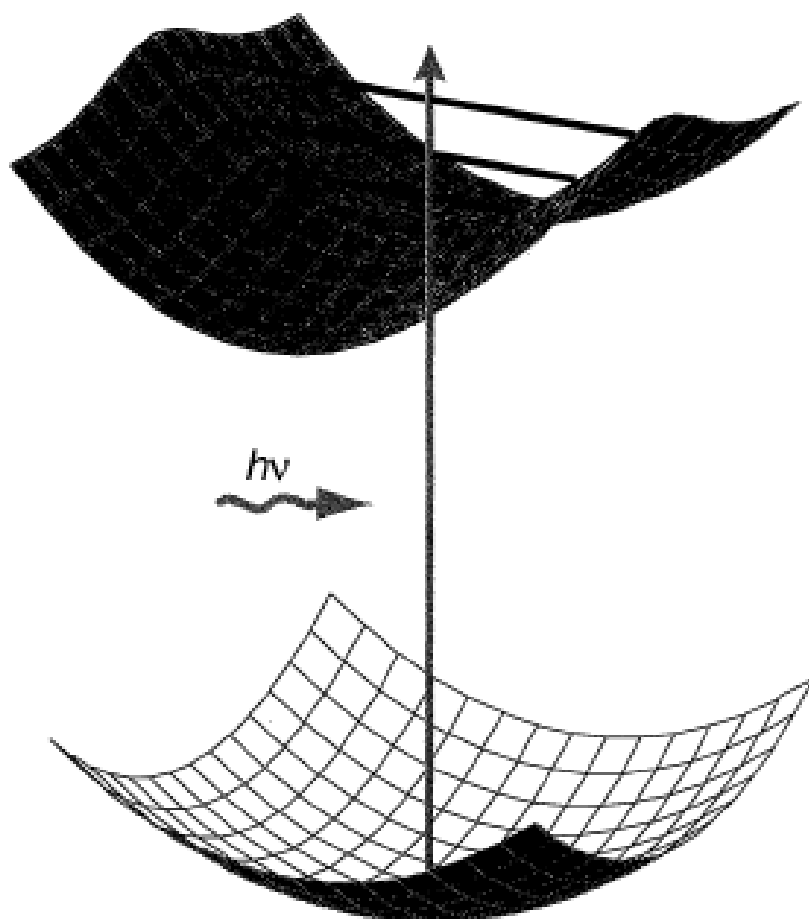
Figure 5.1 – Anion photoelectron spectroscopy. An anion is photodetached and the potential energy surface of the neutral species is probed[3].

Anion photoelectron spectroscopy of semiconductor clusters:

Besides studying transition states or van der Waals wells, anion PES can also be used to study gas phase semiconductor clusters. Semiconductors are of special interest because of their many applications in electronics including their use as transistors, thin films, light emitting diodes, sensors etc. As electronic components become increasingly small, it is only a matter of time until they are in the size regime of clusters[4]. Electronic structure of small clusters is well understood and can be described in terms of molecular orbitals[5]. Likewise, large clusters such as quantum dots and passivated nanocrystals are well understood in terms of perturbed bulk electronic properties; for instance, quantum confinement affects associated with the finite size of the clusters[6]. What is not very well understood is the size regime between the small clusters, containing ten atoms or less, and the larger quantum dots and nanocrystals, containing hundreds or thousands of atoms. Research in this area is of great interest mainly due to the electronics industry because the electronic structure of the clusters determines their optical and electronic properties[5]. Another aim of studying semiconductor clusters is to understand their growth patterns particularly dealing with thin-film growth. Anion PES may help to elucidate how the smaller clusters change size and geometry as they grow in size[7, 8].

Anion photoelectron spectrometer:

The anion photoelectron spectrometer used in the studies presented in this thesis consists of four parts: the ion source, mass spectrometer, electron analyzer and the laser. The spectrometer has been described previously[4], but will be briefly touched upon here. The ion source starts with a piezoelectric pulsed valve, operating

at 20 Hz. Ions are created by several ways. For the experiments probing the Cl + H_2 van der Waals well, ions were made by bubbling a 50% H_2 or D_2 50% Ar mixture over CCl_4 and bombarding the mixture with an electron gun. For the studies dealing with the semiconductor clusters, the ions were made by laser ablation. The ablation source consisted of a rotating and translating disk. The semiconductor is fixed in the disk and is ablated with the second harmonic (2.331 eV, 18 mJ/pulse) of a pulsed Nd: YAG laser. The laser pulses are focused onto the target with a 50 mm lense. The resulting plasma is entrained in a pulse of Ar carrier gas from the piezoelectric valve. The plasma is expanded through a clustering channel. The length of this clustering channel depends on the species studied.

After the ions are made, they pass through a skimmer into a differentially pumped vacuum chamber. Negative ions are extracted perpendicularly to their flow direction by a pulsed electric field. The extracted ions then enter a linear reflectron time of flight (TOF) mass spectrometer, where they are separated in time and space according to their mass-to-charge ratios. The TOF mass spectrometer resolution is m/Δm $\approx$ 2000.

Now the ion of interest can be selected and photodetached with a laser. The laser is timed so as to photodetach the ions of the desired mass. The photoelectrons are analyzed by TOF. The electrons can be analyzed by either a field-free flight tube or by a magnetic bottle. The difference between the two is that the field-free tube has higher resolution and low collection efficiency while the magnetic bottle has low resolution and high collection efficiency. The field-free tube is used when there is a

high signal-to-noise ratio, while the magnetic bottle is used when the signal-to-noise ratio is low.

For the field-free tube, the energy resolution is 8–10 meV for an eKE of 0.65 eV and degrades as $(eKE)^{3/2}$ at higher eKE. The PE spectra were taken at two laser polarization angles, 0° and 90° with respect to the direction of electron detection. The laser polarization can be rotated using a half-wave plate. The eKE of the photoelectrons may also be determined by a magnetic bottle TOF analyzer. For the magnetic bottle, photoelectron kinetic energies are determined by time-of-flight measurements using a magnetic bottle analyzer based on the designs by Cheshnovsky et al. [5] and Wang et al[6]. The mass-selected clusters are not decelerated before interaction with the laser. The magnetic bottle region consists of two parts: a strong permanent magnet adjustable in height below the photodetachment zone and a 1.2 m long solenoid. The distance of the permanent magnet from the ion beam and the strength of the magnetic field at the center of the solenoid were chosen to optimize the signal-to-noise ratio. All spectra shown here were background-subtracted to eliminate the contribution from electrons produced by stray photons interacting with surfaces near the interaction region.

The laser used for photodetachment is a Q-switched Nd:YAG laser with a pulse length of 7-9 nanoseconds. The second harmonic, 532 nm, was generated in a doubling crystal. The fourth harmonic, 266 nm, is formed also in a doubling crystal from the second harmonic. The third harmonic, 355 nm, is formed via sum frequency generation from the fundamental and the second harmonic. 299 nm light is generated by passing the fourth harmonic, 266 nm, through a high-pressure (350 psi) hydrogen

Raman cell. To probe deeper in the electronic structure of some semiconductor

clusters, a 157 nm fluorine excimer laser was employed. The laser was a GAM

EX50F laser, generating 157 nm light at 2 mJ/pulse, with unstable resonator optics.

References:

1. Neumark, D.M., Probing the transition state with negative ion photodetachment:
    experiment and theory. Physical Chemistry Chemical Physics, 2005. **7**: p. 433-442.

2. Neumark, D.M., *Spectroscopy of reactive potential energy surfaces.* Phys. Chem. Comm., 2002. **5**(11): p. 76-81.

3. Neumark, D.M., *Tranistion State Spectroscopy.* Science, 1996. **272**: p. 1446-1447.

4. Ho, K.-M., et al., *Structures of medium-sized silicon clusters.* Nature, 1998. **392**(6676): p. 582-585.

5. Xu, C., et al., *Vibrationally resolved photoelectron spectroscopy of silicon cluster anions Sin (n = 3-7).* Journal of Chemical Physics, 1998. **108**(4): p. 1395-1406.

6. Alivisatos, A.P., *Perspectives on the physical chemistry of semiconductor nanocrystals.* Journal of Physical Chemistry, 1996. **100**(31): p. 13226-13239.

7. Asmis, K.R., T.R. Taylor, and D.M. Neumark, *Anion photoelectron spectroscopy of B2N-.* The Journal of Chemical Physics, 1999. **111**(19): p. 8838-8851.

8. Asmis, K.R., T.R. Taylor, and D.M. Neumark, *Anion photoelectron spectroscopy of B3N-.* Journal of Chemical Physics, 1999. **111**(23): p. 10491-10500.

Chapter 6.   Anion photoelectron spectroscopy of the Cl + H$_2$ van der Waals well†

Introduction:

Recent experimental and theoretical studies have shown the "simplest Cl reaction[1]," Cl + H$_2$ → HCl + H, exhibits qualitatively new and complex features that raise fundamental issues in our understanding of chemical reaction dynamics. A combined theoretical and experimental study by Skouteris et al.[2] on the Cl + HD reaction showed that the presence of a shallow (0.51 kcal/mol) van der Waals well in the entrance valley was necessary to reproduce the experimental HCl:DCl product branching ratio as a function of collision energy, providing the first experimental evidence that such a well has a measurable effect on a chemical reaction, whereas quantum scattering calculations on the G3 surface predicted that HCl and DCl would be produced in equal amounts. In addition, there is considerable controversy regarding the reactivity of the spin-orbit excited Cl*($^2P_{1/2}$) state. Experiments by Liu[3] indicate that the Cl*($^2P_{1/2}$) + H$_2$ reaction cross section is comparable or greater that that for Cl($^2P_{3/2}$) + H$_2$, while multi-surface reactive scattering calculations by Alexander et al.[4] predict that the reactivity of Cl* is much smaller than that of Cl. In this chapter, the photoelectron (PE) spectrum of the ClH$_2^-$ and ClD$_2^-$ anions, an experiment that directly probes the neutral reactant van der Waals well as well as the Cl spin-orbit structure in the reactant valley are presented.

The results presented here represent a new application of anion PE spectroscopy to reaction dynamics. Previously, we have used negative ion PE spectroscopy to probe the transition state region of several bimolecular

† previously published as: J. Chem. Phys. **117** 8181 (2001).

reactions[5]. This "transition state spectroscopy" experiment requires good Franck-Condon overlap between the anion ground vibrational state and the neutral transition state. As an example, the geometry of the FH_2^- anion[6], which is essentially F^- clustered to H_2, is close to that of the relatively "early" barrier for the exothermic $F + H_2$ reaction.[7] The FH_2^- PE spectrum[8] then yields resolved vibrational structure characteristic of the neutral transition state. In contrast, the slightly endothermic $Cl + H_2$ reaction has a much later barrier. Based on the rotationally resolved IR spectrum of ClH_2^- by Bieske[9, 10] and electronic structure calculations of the $Cl + H_2$ surface[11], photodetachment of ClH_2^- should have poor overlap with the transition state but excellent overlap with the van der Waals well in the $Cl + H_2$ reactant valley, as shown in Figures 6.1 and 6.2. Hence, the PE spectrum of ClH_2^- should directly probe the reactant van der Waals well. The ClH_2^- complex is comparatively strongly bound compared to the FH_2^- anion geometry due to ion-induced dipole and quadrupole interactions which favor linear geometry. In addition, we have shown that negative ion photodetachment of rare-gas halide complexes such as $ArCl^-$[12] reveal how the spin-orbit levels of a free Cl atom are perturbed in the weakly bound ArCl open-shell complex. The PE spectrum of ClH_2^- should yield analogous information for the neutral ClH_2 complex, providing some insight into the controversy regarding Cl* reactivity.

Experiment:

The photoelectron spectrometer on which these experiments were performed has been described previously[13]. Briefly, negative ions are generated by crossing a pulsed molecular beam of the appropriate gas mixture with a 1 keV electron beam just downstream of the nozzle. To make ClH_2^- and ClD_2^-, a mixture of 50% H_2 or D_2 in Ar was passed over CCl_4 en route to the pulsed (piezoelectric)

96

valve. The backing pressure was 70 psig, the nozzle diameter was 0.1 mm, and the valve was operated at a repetition rate of 20 Hz. The pulsed beam passes through a skimmer into a differentially pumped region, and negative ions are extracted from the beam by pulsed electric fields and injected into a linear reflectron time-of-flight mass spectrometer with a mass resolution $m/\Delta m \cong 2000$. Mass-selected anions are photodetached at the spatial focus of the mass
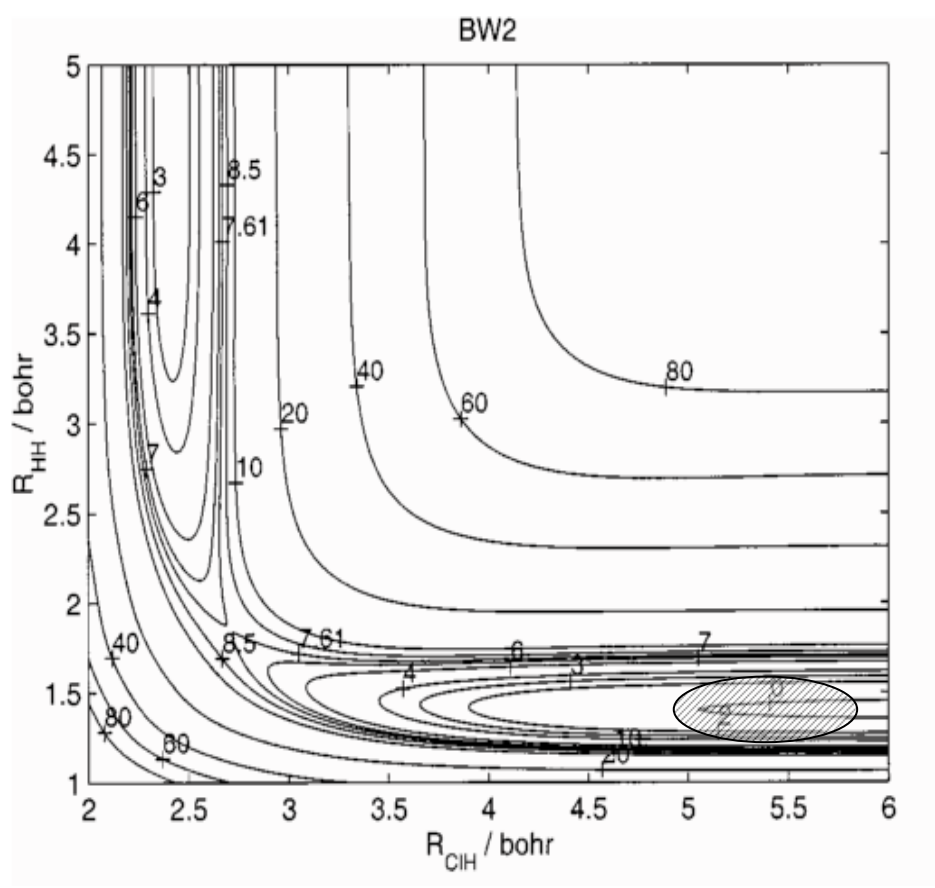
Figure 6.1 – ClH_2^- equilibrium geometry and ground state wavefunction (from Ref. [14]) superimposed on $Cl + H_2$ potential energy surface from Ref. [11]. Shows a collinear cut through the entrance valley, transition state and exit valley of this surface.
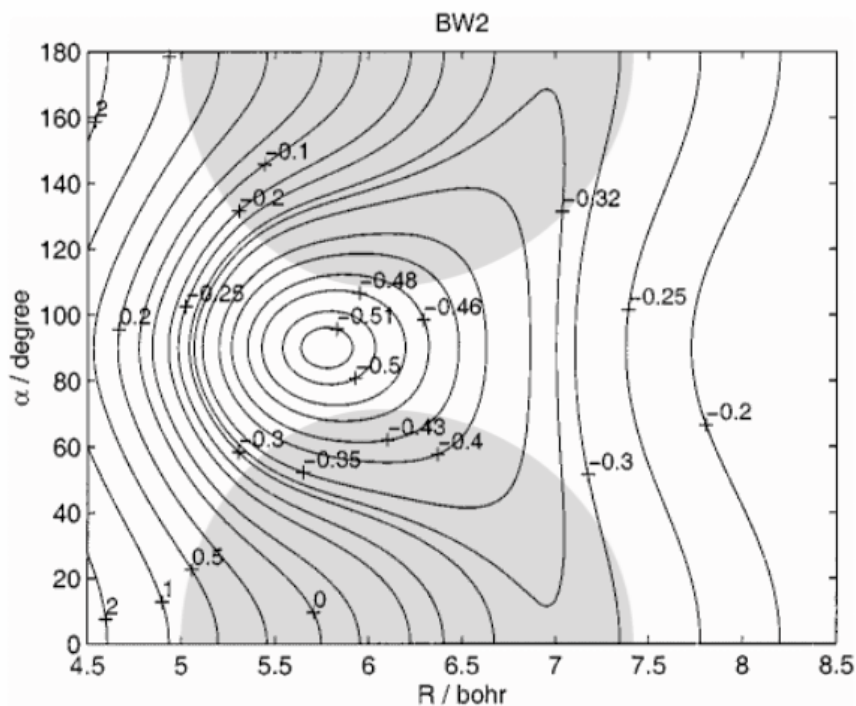
Figure 6.2 – ClH$_2^-$ equilibrium geometry and ground state wavefunction of the

reactant van der Waals well.

spectrometer by a pulsed laser at a wavelength of 299 nm (4.154 eV), generated

by Stokes-shifting the fourth harmonic (266 nm) of a Nd:YAG laser in a high

pressure H$_2$ Raman cell. PE spectra for ClH$_2^-$ were taken at m/e=39 to eliminate

background from ^{37}Cl$^-$ at the same mass as ^{35}ClH$_2$, while ClD$_2^-$ PE spectra were

taken at m/e=41. Photoelectrons were collected at the end of a 1 m long, field-

free flight tube and energy-analyzed by time-of-flight; the energy resolution is 8-

10 meV for the spectra shown here. The spectra were taken at a laser polarization

angle of 0° with respect to the direction of electron detection; spectra at 90° were

similar but much lower in intensity.

Results:

Figure 6.3 shows the PE spectra for ClH_2^- (top) and ClD_2^- (bottom). The spectra are plotted as a function of electron binding energy, eBE, given by

$$eBE = h\nu - eKE, \hspace{4cm} (8.1)$$

where hν is 4.154 eV is the photon energy and eKE is the measured electron kinetic energy. Each spectrum is dominated by two peaks labeled A(A') and B(B') in the ClH_2^- (ClD_2^-) spectrum. The small peaks at 3.613 eV in both spectra are from Cl^- that is presumably produced by photodissociation of the cluster followed by photodetachment. The small peak between A and B at 3.75 eV in the ClH_2^- spectrum is from $^{35}Cl(H_2)_2^-$ at the same mass; this was confirmed by measuring the PE spectrum of $^{37}Cl(H_2)_2^-$ at m/e=41. The maxima of peaks A and B occur at 3.683 and 3.793 eV, respectively, with peak widths (FWHM) of 26 and 23 meV. Peaks A' and B' in the ClD_2^- spectra are centered at 3.697 and 3.806 eV, respectively, and have FHWM widths of 52 and 40 meV, respectively. The onsets of peaks A and A' are at essentially the same energy, 3.666 eV, as are the onsets for peaks B and B' (3.778 eV). In addition, the maximum of peak A coincides with a shoulder on the rising edge of peak A'.
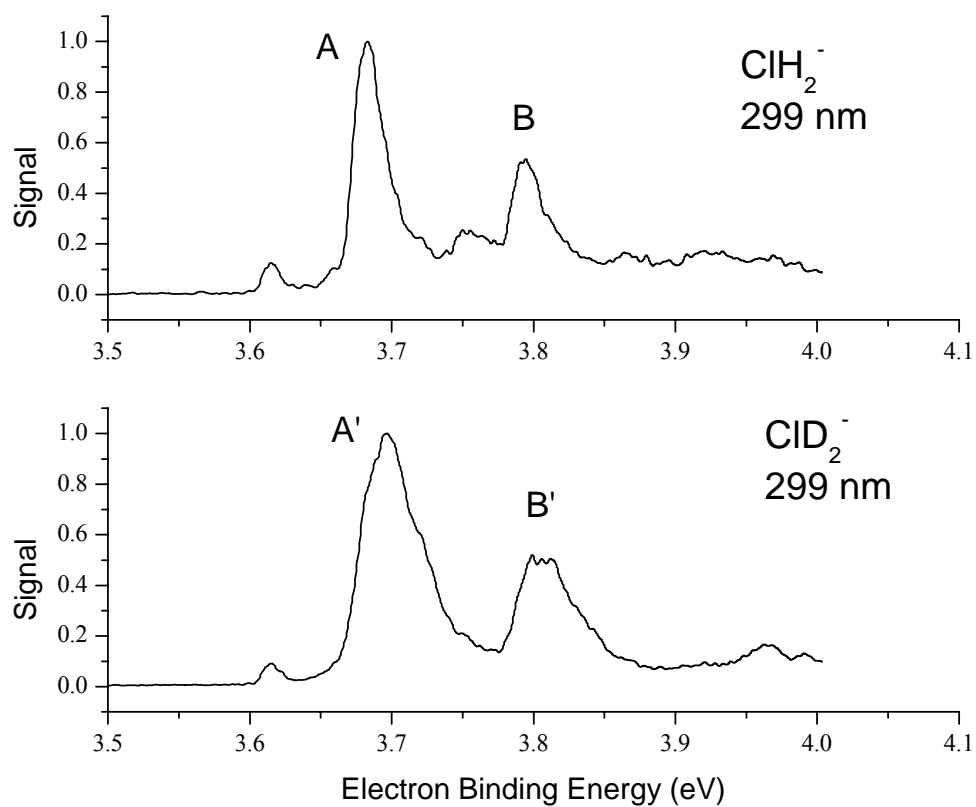
Figure 6.3 – Anion photoelectron spectra of ClH$_2^-$ (top) and ClD$_2^-$(bottom) at 299

nm (4.154 eV). The laser polarization angle was 0°.

Discussion:

The spacings between the maxima of peaks A and B, 0.111 eV, and peaks A' and B', 0.109 eV, are identical to the Cl spin-orbit splitting of 0.109 eV within our experimental resolution. We therefore assign peaks A and B as transitions to the neutral $Cl(^2P_{3/2}) \cdot H_2$ and $Cl*(^2P_{1/2}) \cdot H_2$ complexes, respectively, with the same assignments holding for the two peaks in the ClD_2^- PE spectrum. In more detail, the $Cl(^2P_{J=3/2})$ will be split by its interaction with the H_2 into P=1/2 (ground) and 3/2 (excited) states, where P is the projection of J onto the axis between Cl and the H_2 center-of-mass, while the interaction between Cl* and H_2 results in a single P=1/2 state. Since the separation of peaks A and B is so close to the Cl atomic spin-orbit splitting, perturbation of the Cl spin-orbit structure at the geometries probed in this experiment appears to be quite minor. As a result, peaks A and A' should be composed of transitions to the ground P=1/2 and P=3/2 states, whereas peaks B and B' arise solely from transitions to the upper P=1/2 state.

The peaks in the PE spectra can arise from transitions to the neutral van der Waals wells on the ground and spin-orbit excited neutral $Cl + H_2$ surfaces, and from transitions to $Cl + H_2$ continuum states. This partitioning between bound and continuum states is determined by the projection of the anion vibrational wavefunction onto the various neutral potential energy surfaces. From Bieske's analysis of the infrared spectrum of ClH_2^-,[10] the anion is linear with a vibrationally-averaged distance between Cl^- and the H_2 center-of-mass of R_0=3.195 Å for the ground vibrational state, and the radial component of the anion ground state wavefunction for ClH_2^- extends from R=2.9-3.5 Å.

Figure 6.2 shows the van der Waals well of the ground state (P=1/2) $Cl + H_2$ potential energy surface calculated by Bian and Werner (the BW2 surface).[11]

The minimum of the van der Waals well corresponds to a T-shaped, C_{2v} structure with R_e=3.058 Å. This value lies well within the range of the anion radial wavefunction.

There is a substantial displacement of θ, the angle between the H_2 axis and the axis joining the Cl to the H_2 center-of-mass, from 0° in the anion equilibrium geometry to 90° at the vdW minimum. However, recent calculations by Alexander[14] show that the ground state anion wavefunctions $\psi_0^{(-)}(R,\theta)$ for ClH_2^- and ClD_2^- are quite delocalized, with substantial amplitude covering nearly the entire available range of θ; the shaded regions in Figure 6.2 show a contour of $\psi_0^{(-)}(R,\theta)$ for ClH_2^-(*ortho*) for which the amplitude is 15% of the maximum. One therefore expects considerable overlap with the large-amplitude vibrational wavefunctions supported by the van der Waals well. The resolution of the PE spectrometer, however, is insufficient to resolve transitions to the individual van der Waals vibrational states.

Calculations by Aquilanti and co-workers[15] indicate that the excited P=3/2 and P=1/2 Cl + H_2 surfaces have collinear minimum energy geometries with shallow vdW wells (~ 5 meV) and R_e≅3.6 Å, with the P=3/2 state having a slightly deeper minimum at the collinear geometry than the ground P=1/2 state. As a result, there may be some overlap with the bound vdW states supported by the two excited state potentials, but vertical detachment from the anion (at R_0=3.195 Å) accesses the repulsive wall in both cases. This will lead to substantial overlap with continuum wavefunctions in the photodetachment transitions to the two excited states.

We are now in a position to consider the features and trends in the PE spectra in more detail, beginning with the energetics. The maxima of peaks A and

A' are shifted toward higher eBE from the maxima of atomic Cl⁻ peaks by 70

meV (565 cm⁻¹) and 85 meV (685 cm⁻¹), respectively, while the onsets of the two

peaks are shifted by 460 cm⁻¹ from the onsets of the atomic peaks. If there were

no interaction between the neutral Cl and H_2 in the FC region, these "solvent

shifts" would directly reflect the dissociation energy D_0 of ClH_2^- and ClD_2^-, but, as

discussed above, there are weak attractive and repulsive interactions on the neutral

surfaces that complicate this picture somewhat. Nonetheless, the solvent shifts of

the peak onsets and maxima bracket the dissociation energies D_0 of 499 cm⁻¹, 559

cm⁻¹, and 488 cm⁻¹ for ClD_2^-(*ortho*), ClD_2^-(*para*), and ClH_2^-(*ortho*), respectively,

estimated by Bieske from the effective radial potentials constructed with the help

of the anion IR spectrum, as well as the slightly larger values, 527 cm⁻¹, 604 cm⁻¹,

and 544 cm⁻¹, respectively, obtained in the recent calculation by Alexander[14].

The difference of 60 cm⁻¹ between the dissociation energies of ClD_2^-(*o*) and ClD_2^-

(*p*) is very close to energy interval between the Cl⁻ + D_2(j=0) and Cl⁻ + D_2(j=1)

dissociation asymptotes for the *ortho* and *para* species.

One striking feature of the PE spectra is the noticeably broader peaks in

the ClD_2^- spectrum compared to ClH_2^-. This may result in part from differing

H_2/D_2 nuclear spin populations in ClH_2^- vs. ClD_2^-. Bieske observed infrared

transitions originating from both ClD_2^-(*o*) and ClD_2^-(*p*), while only transitions

from ClH_2^-(*o*) were seen. The absence of ClH_2^-(*para*) was attributed to its

considerably *lower* D_0 compared to ClH_2^-(*o*), (110 cm⁻¹, according to Alexander's

calculation[14]) combined with the 3:1 *ortho:para* ratio in normal H_2.

The effect of anion nuclear spin populations on the photoelectron spectrum

was discussed previously in the context of FH_2^-[8, 16], and similar concepts can

be applied to ClH_2^-. We expect the bend wavefunctions for neutral Cl·H_2 in the

Franck-Condon region to be close to the H_2 free-rotor limit regardless of the neutral electronic state. The narrow peaks in the ClH_2^- PE spectrum suggest that photodetachment is dominated by a transition to a single H_2 rotor state; the $H_2(j=1)$ and $j=3$ levels, which would be the lowest rotor states accessible from $ClH_2^-(o)$, are separated by 0.050 eV (400 cm^{-1}), more than twice the width of peak A or A'. If photodetachment from $ClD_2^-(o)$ and $ClD_2^-(p)$ were dominated by transitions to the D_2 $j=0$ and 1 rotor levels, respectively, these transitions would be separated by 60 cm^{-1} (7.4 meV), and would presumably not be resolved in our PE spectrometer. The net result is a broadening of all ClD_2^- transitions due to the presence of two nuclear spin species, as opposed to only one in ClH_2^-.

The broadening may also have its origins in the excited state transitions. Bieske[10] has shown that the effective radial potential for ClD_2^- is deeper than that for ClH_2^-, and the radial wavefunction is shifted toward slightly smaller values of R. This results, for example, in a lower value of R_0 for ClD_2^-, 3.159 Å vs. 3.195 Å for ClH_2^-. Photodetachment of ClD_2^- therefore samples more of the repulsive wall and less of the van der Waals well for the neutral P=3/2 and 1/2 excited states, broadening peaks B' and A' with respect to peaks B and A. The relative importance of these two possible origins of the differential broadening can be determined in quantum mechanical simulations of the PE spectra, and these are currently being carried out by Alexander and Manolopoulos[17]. In addition, planned experiments in which $ClH_2^-(p)$ is generated using *para*-H_2 as the expansion gas will directly address the effect of nuclear spin statistics on the PE spectra.

Finally, we consider the results obtained here with our previous PE spectra of FH_2^-[8, 16]. There are two significant differences between the spectra. In the

FH$_2^-$ spectra, perturbation of the F atomic spin-orbit fine structure by the H$_2$ is significant; the spin-orbit excited states were found to be strongly repulsive in the Franck-Condon region and well-separated from the ground state transitions, even though the spin-orbit splitting in F is only about half that of Cl. This difference occurs because the FC region for FH$_2^-$ photodetachment overlaps the F + H$_2$ transition state, near which the spin-orbit excited states diverge significantly from the ground state[15].

The other important difference is that the FH$_2^-$ ground state spectrum is composed of partially resolved progressions in what are essentially H$_2$ nearly free-rotor levels, the envelope of which covers almost 0.2 eV, i.e. an order of magnitude broader than peak A in the ClH$_2^-$ spectrum, regardless of whether *para-* or *normal*-H$_2$ was used. These progressions resulted from a change of geometry between the linear FH$_2^-$ anion and bent FH$_2$ transition state, for which the F-H-H angle is 119°. In contrast, peak A in the ClH$_2^-$ shows no evidence for an analogous hindered rotor progression, even though there is a larger change in angle between the anion and vdW minimum. This somewhat surprising result may reflect the more delocalized bend wavefunction in ClH$_2^-$ compared to FH$_2^-$, resulting in part from the considerably higher dissociation energy of 0.20 eV for FH$_2^-$[6]. A more quantitative assessment of this effect will require full quantum mechanical simulation of the ClH$_2^-$ PE spectrum; these calculations are currently in progress[17].

Conclusions:

The ClH$_2^-$ and ClD$_2^-$ PE spectra presented here represent the first experimental probe of the Cl + H$_2$ pre-reactive van der Waals region and of the low-lying Cl + H$_2$ spin-orbit excited states, thus providing new information on

two key aspects of the Cl + H$_2$ reaction dynamics. The work described here represents the first step in the spectroscopic characterization of the potential energy surfaces of this benchmark reaction.

References:

1. Alagia, M., et al., *Dynamics of the Simplest Chlorine Atom Reaction - an Experimental and Theoretical Study.* Science, 1996. **273**(5281): p. 1519-1522.

2. Skouteris, D., et al., *van der Waals interactions in the Cl+HD reaction.* Science, 1999. **286**(5445): p. 1713-1716.

3. Dong, F., S.H. Lee, and K. Liu, *Direct determination of the spin-orbit reactivity in Cl(P-2(3/2),P-2(1/2))+H-2/D-2/HD reactions.* Journal of Chemical Physics, 2001. **115**(3): p. 1197-1204.

4. Alexander, M.H., G. Capecchi, and H.J. Werner, *Theoretical study of the validity of the Born-Oppenheimer approximation in the Cl+H-2 -> HCl+H reaction.* Science, 2002. **296**(5568): p. 715-718.

5. Neumark, D.M., *Spectroscopy of reactive potential energy surfaces.* PhysChemComm, 2002. **5**: p. 76-81.

6. Nichols, J.A., et al., *Theoretical studies of anion-molecule interactions...* Journal Of Physical Chemistry, 1991. **95**: p. 1074-1076.

7. Stark, K. and H.J. Werner, *An Accurate Multireference Configuration Interaction Calculation of the Potential Energy Surface For the F+H-2-]Hf+H Reaction.* Journal of Chemical Physics, 1996. **104**(17): p. 6515-6530.

8. Manolopoulos, D.E., et al., *The Transition State Of the F+H-2 Reaction.* Science, 1993. **262**(5141): p. 1852-1855.

9. Wild, D.A., et al., *Rotationally resolved infrared spectrum of the Cl--H-2 anion complex.* Journal of Chemical Physics, 2000. **113**(22): p. 10154-10157.

10.   Wild, D.A., et al., *The Cl-35(-)-H-2 and Cl-35(-)-D-2 anion complexes: Infrared spectra and radial intermolecular potentials.* Journal of Chemical Physics, 2001. **115**(2): p. 824-832.

11.   Bian, W.S. and H.J. Werner, *Global ab initio potential energy surfaces for the ClH2 reactive system.* Journal of Chemical Physics, 2000. **112**(1): p. 220-229.

12.   Lenzer, T., et al., *Zero electron kinetic energy spectroscopy of the ArCl- anion.* Journal of Chemical Physics, 1999. **110**(19): p. 9578-9586.

13.   Xu, C., et al., *Photoelectron spectroscopy of C_4^-, C_6^-, and C_8^-.* J. Chem. Phys., 1997. **107**: p. 3428-3436.

14.   Alexander, M.H., *Theoretical investigations of the lower bend-stretch states of the Cl-H2 anion complex and its isotopomers.* Journal Of Chemical Physics, submitted.

15.   Aquilanti, V., et al., *Potential energy surfaces for F-H-2 and Cl-H-2: Long-range interactions and nonadiabatic couplings.* Journal of Physical Chemistry A, 2001. **105**(11): p. 2401-2409.

16.   Bradforth, S.E., et al., *Experimental and Theoretical Studies Of the F+H-2 Transition State Region Via Photoelectron Spectroscopy Of Fh2.* Journal Of Chemical Physics, 1993. **99**(9): p. 6345-6359.

17.   Alexander, M.H. and D.E. Manolopoulos, *A simple theoretical study of the ClH2 photoelectron spectrum.* PCCP, 2004. **6**: p. 4984-4990.

Chapter 7.   Studies of silicon and germanium clusters

Introduction:

Studying silicon clusters is of interest both to industrial applications and to fundamental understanding. As the size of electronic components decrease, the possibility of devices on the molecular level becomes immanent. In that case, an understanding of silicon clusters on the molecular level is paramount to the ability to engineer such devices. Also, semiconductor thin films have industrial applications. Comprehension of the growth patters these semiconductors exhibit can lead to greater control of these types of thin films.

Much is known about bulk semiconductors, quantum dots, and small silicon clusters, but not much is know about when, in a size regime, do semiconductor clusters stop behaving like small molecules with discrete energy levels and start having more band-like structure. One of the goals in the Neumark group is to understand how small clusters of semiconductors evolve towards bulk-like properties. Recently the anion photoelectron (PE) spectroscopy studies on indium phosphide[1] showed that the electronic states contributing to the two bands in the photoelectron spectrum have similar orbital character to the bulk indium phosphide photoemission spectrum. Another issue worth exploring is how do surface atoms effect clusters compared to passivated nanocrystals of comparable size.

A large amount of what is known about silicon clusters experimentally is based off of ion mobility studies by Jarrold and coworkers[2-5]. An interesting result form their studies is that at clusters with nineteen atoms or more start to have more spherical cage-like geometries available whereas smaller clusters exhibit only prolate

geometries. A great deal of theoretical work has also been done. Jarrold and

coworkers used density functional theory with the local density approximation to

accompany their mobility measurements. Likewise, global geometry optimizations

have been done with different results. A large number of the medium-sized clusters

are based off of the tricapped trigonal prism (TTP). Muller et al.[6] confirmed the

existence of TTP motifs by anion photoelectron (PE) spectroscopy up to 20 atoms.

Tekin and Hartke[7] found that for Si_{14} to Si_{16} at ten atom building block consisting

of a sandwhich of a 4-membered and 6-membered ring was the basis of structure

rather than a TTP.

Several relatively small neutral and charged Sin clusters ($n \leq 10$) have been

investigated in detail through a combination of vibrationally resolved anion

photoelectron spectroscopy in the gas phase[8-10], infrared, Raman and electronic

spectra of matrix-isolated neutral and anionic clusters[11-13], and electronic structure

calculations[14-16], yielding information on the geometries and vibrational

frequencies of the ground and low lying electronic states. Studies of larger silicon

clusters are greatly complicated by the increasing occurrence of low-lying local

minima[7, 17-20]. In this chapter, spectra with detachment energy of 7.8 eV of silicon

clusters up to 35 atoms are presented.

Experimental:

The negative time-of-flight photoelectron spectrometer has been described

previously[21]. Silicon clusters were generated in a pulsed molecular beam/laser

ablation source where the second harmonic of an Nd:YAG (532 nm) vaporized

silicon from a rotating and translating pure silicon disk. The resulting plasma is

entrained in a pulse of argon carrier gas and expanded through a clustering channel.

Source conditions, including relative time between gas pulses, laser firing, and

extraction pulse, were chosen as to maximize the formation of the particular silicon

cluster studied. The nozzle diameter of the piezoelectric valve was 0.5 mm with a

backing pressure of 40 psig and a pulse width of 250 microseconds. Ions are extracted

perpendicularly to the expansion by means of a pulsed electric field to a linear

reflectron time-of-flight mass spectrometer with a resolution of $m/\Delta m \cong 2000$ and

average ion beam energy of 3750 eV. Mass selected anions are photodetached at the

spatial focus of the mass spectrometer by a 157 nm laser from a fluorine excimer

laser (GAM 250F) at 2 mJ/pulsle with unstable resonator optics. Signal electrons

were subtracted from background by taking 400 background shots off resonance from

the ion packet and then subtracting that from 400 photodetachment laser pulses.

Photoelectrons were analyzed from a magnetic bottle time-of-flight analyzer without

deceleration. All spectra are presented as the relative electron signal versus electron

kinetic energy.

Results:

The anion PE spectra for the silicon clusters are presented in Figures 7.1-7.3.

The data are presented with relative electron signal versus electron kinetic energy

(eKE) where

$$eKE = h\nu - EA - T_0^0 + T_0^- - E_v^0 + E_v^-$$ (9.1)

The photon energy for the probe laser is 7.8 eV. Figure 7.1 shows the PE spectra for

Si_n^- clusters from n=4 to n=16. As the clusters increase in size, the first band of the

spectra seems to converge toward a second band at low eKE. This effect is furthered

in Figure 7.2 where the spectra for n=14-19 are presented. At n=19, the bands seem to have a "filling in" effect. This trend continues in Figure 7.3 up until the spectral features for Si_{32} and Si_{35} become more undefined and blob-like. The anion PE spectra of germanium clusters up to sixteen germanium atoms are presented in Figure 7.4. There is a close, but not exact analogue to the silicon clusters with germanium.

For most of the spectra, there is a large amount of signal at low electron kinetic energy. At first glance, it may look like thermionic emission is taking place in these silicon clusters, but that is not the case. The signal at low eKE is real because for Si4 and Si5 there is not a large amount of signal at low eKE and similarly, in our studies of InP, some ions went to zero signal at low eKE. If thermionic emission to occurs in clusters, its presence is independent of photodetachment wavelength. For the studies of silicon clusters at 6.4 eV photodetachment energy, there was no large signal at low eKE.

In order to understand the spectra more, density functional calculations using the B3LYP level of theory with the double zeta basis set 6-31G were carried out. Starting geometries were based off of the work by Jarrold and coworkers and Yoo et. al.[22] Geometry optimizations, orbital eigenvalues, and frequency calculations were employed using the Gaussian 98 computational package[23]. The final geometries are shown in Figures 7.5-7.7 for Si_{18}, Si_{19} prolate and Si_{19} spherical respectively. For all geometries shown, they possess all real vibrational frequencies, so they are local minima on their respective silicon cluster potential energy surface. Both the anion and neutral species were calculated, so the adiabatic electron affinity for each cluster can be estimated.
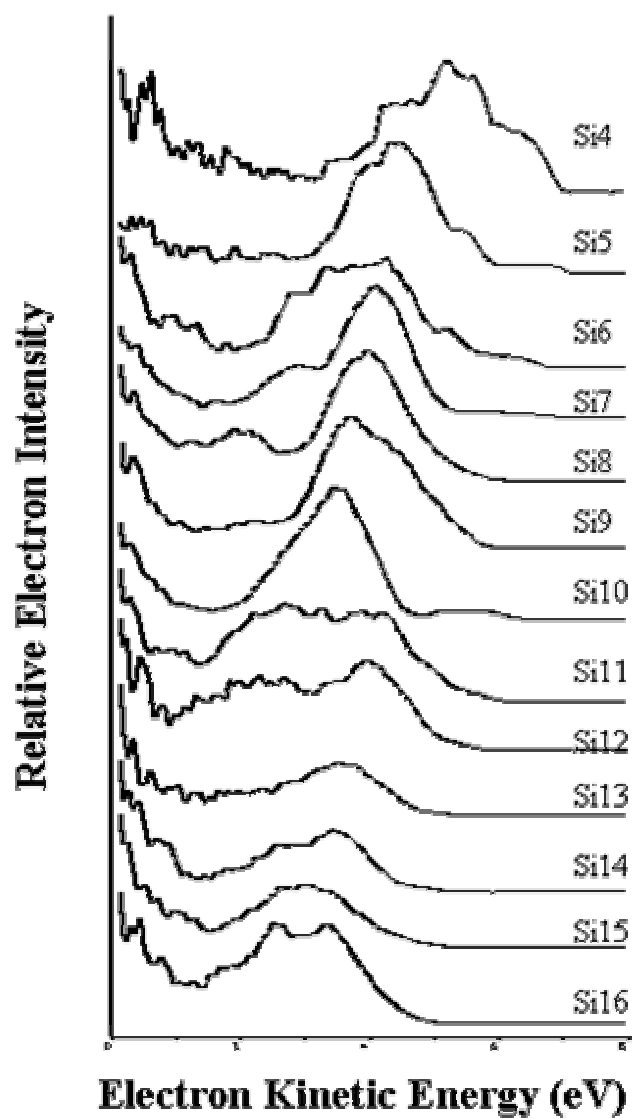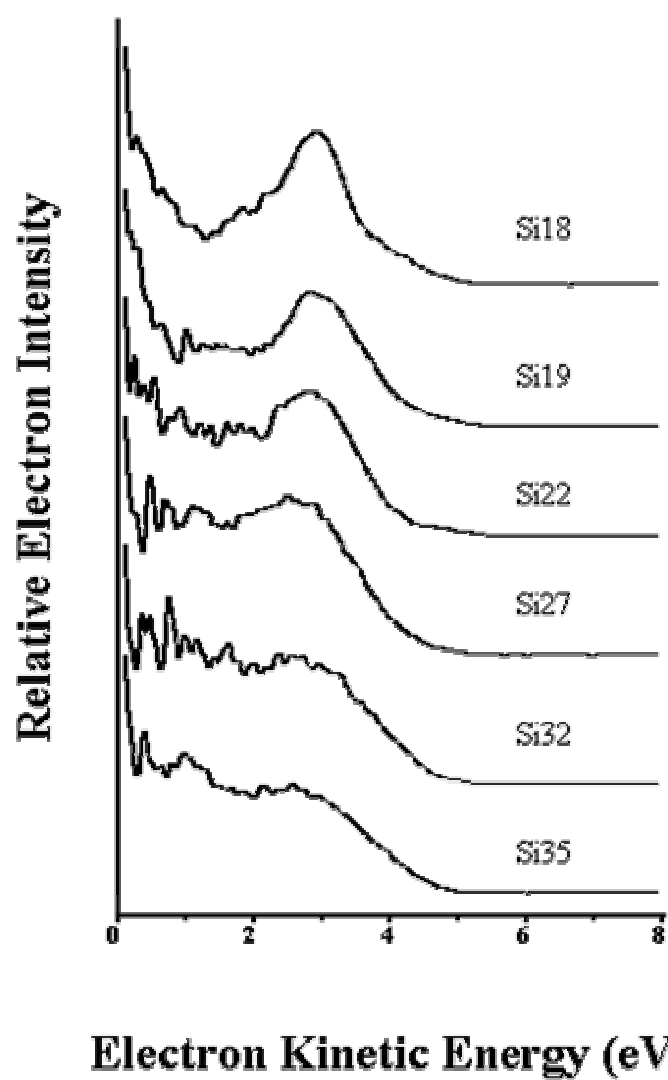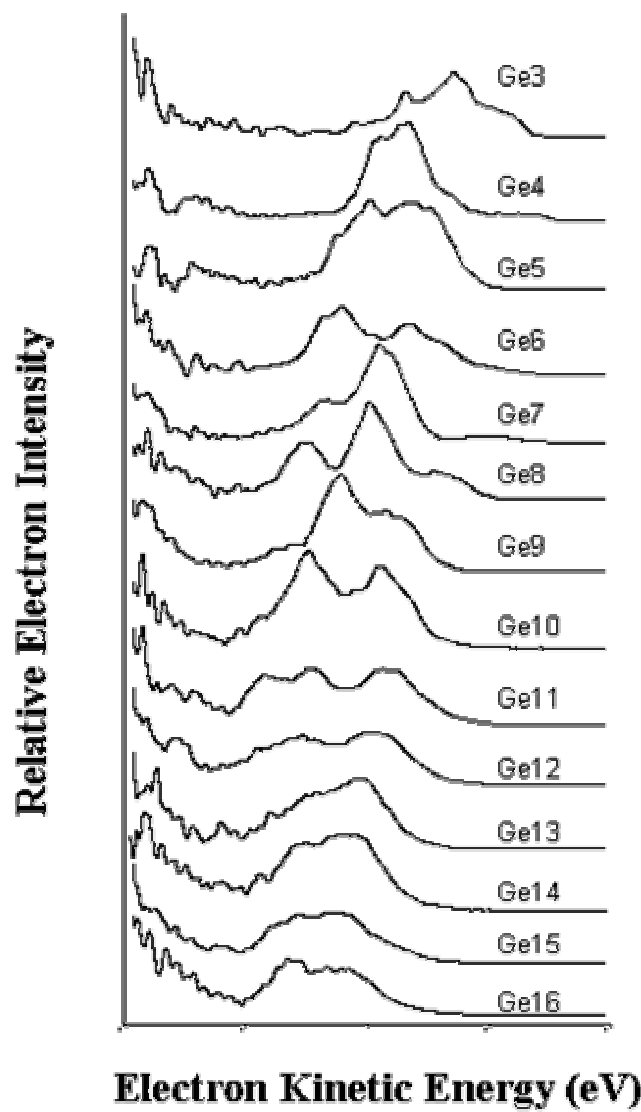
Figure 7.1 – Anion photoelectron spectra of silicon clusters from Si_4^- to Si_{16}^-.
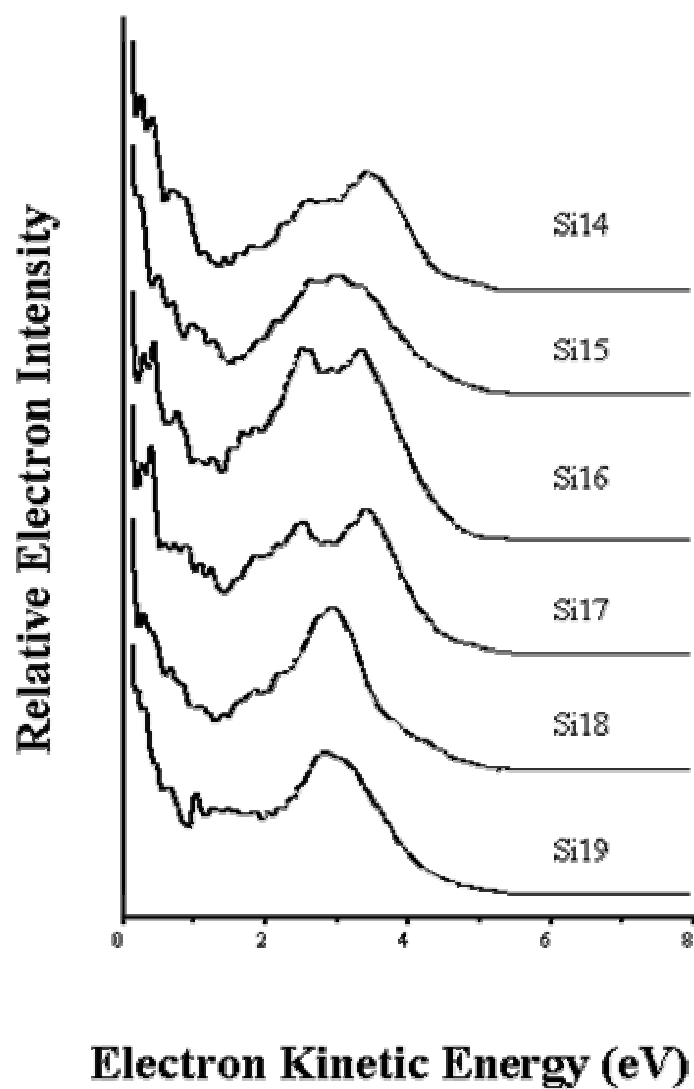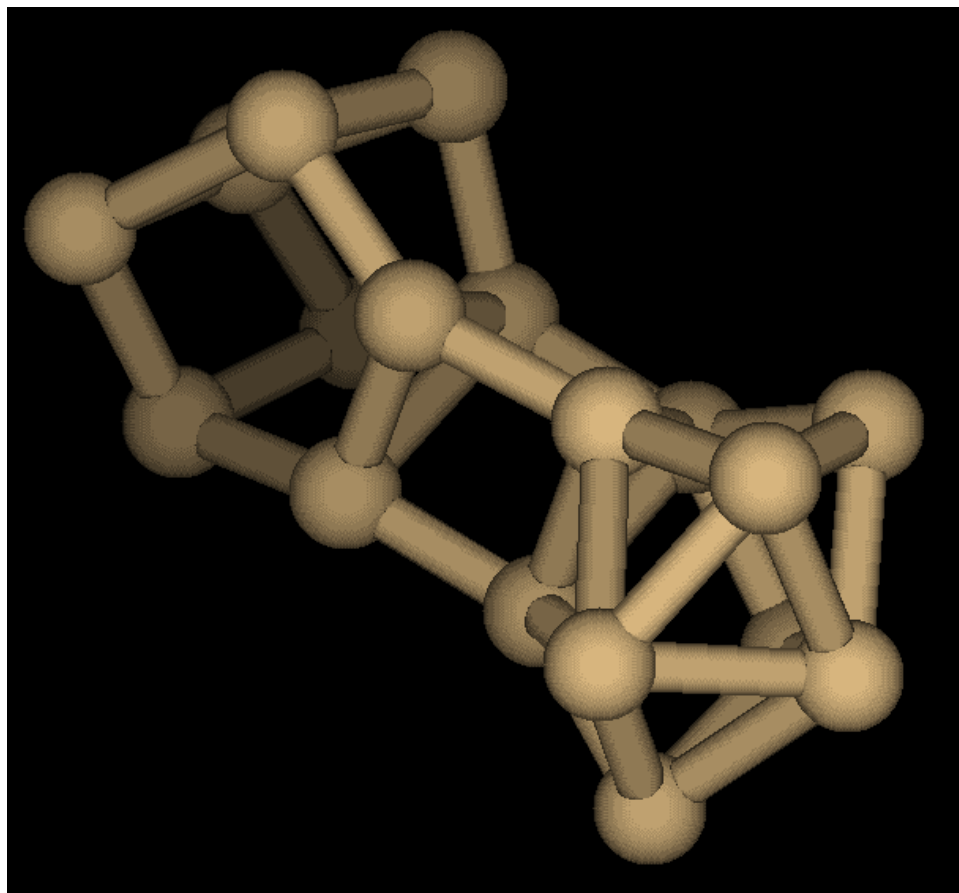
Figure 7.2 – Anion photoelectron spectra of silicon clusters from Si_{14}^- to Si_{19}^-.
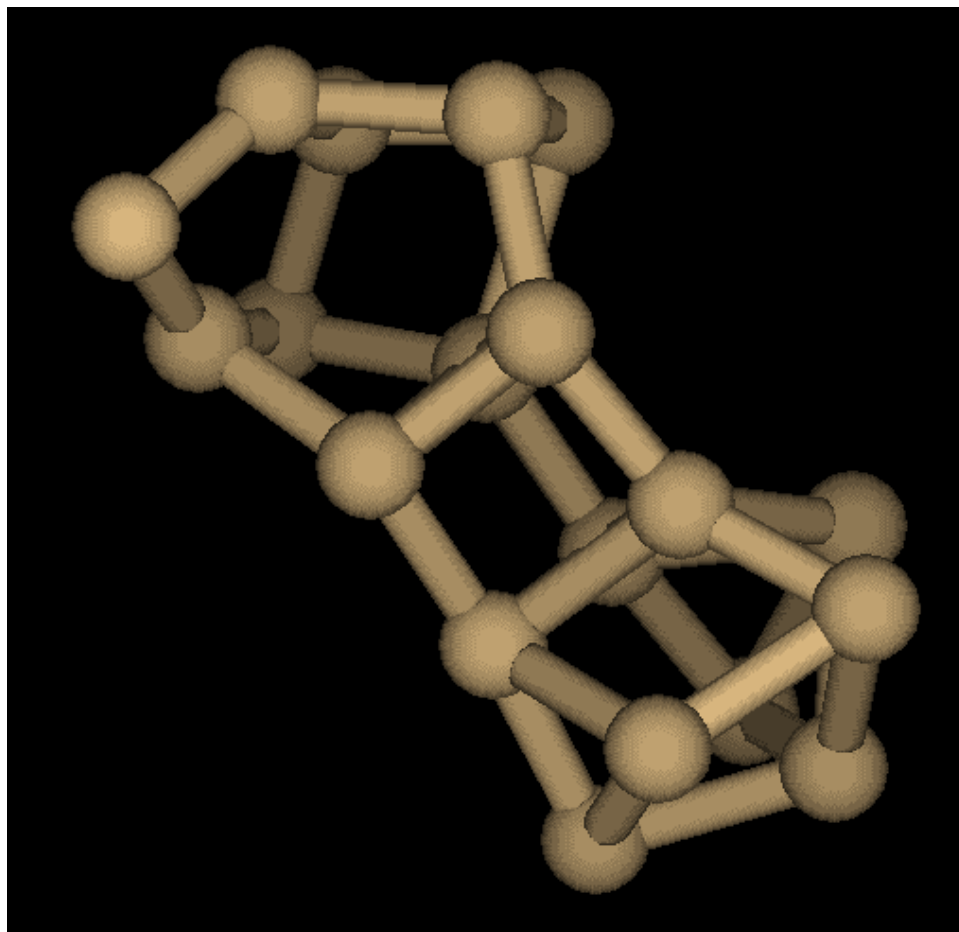
Figure 7.3 – Anion photoelectron spectra of silicon clusters from Si_{18}^- to Si_{35}^-.
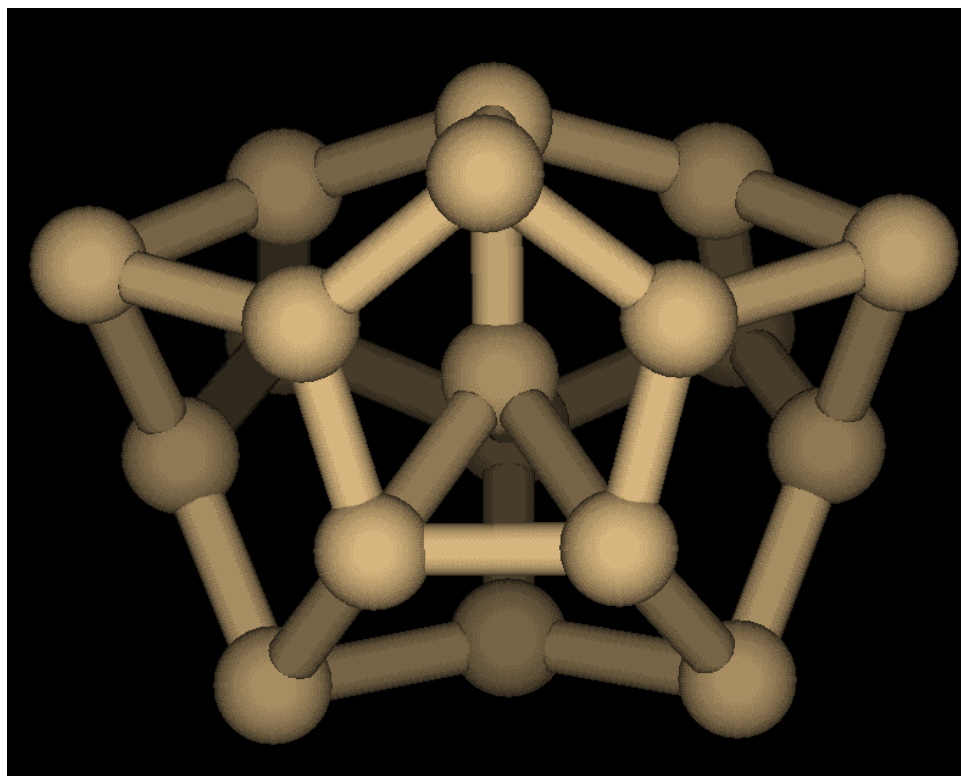
Figure 7.4 – Anion photoelectron spectra of germanium clusters from Ge_3^- to Ge_{16}^-.

**Figure 7.5 –** Geometry of the Si$_{18}$ prolate cluster.

Figure 7.6 – Geometry of the Si_{19} prolate cluster.

Figure 7.7 – Geometry of the Si$_{19}$ spherical cluster.

Stick spectra were generated to look at the electronic states of the spectra. These spectra were generated by taking the eigenvalues of the orbitals of the anion geometries and applying Koopman's theorem to get the energy of an electron leaving that orbital. Further, the molecular orbital coefficients were squared and summed for each orbital in order to get the atomic orbital character. These stick spectra are overlaid on the experimental spectra and presented in Figures 9.8-9.10 for the Si_{18}, Si_{19} prolate and Si_{19} spherical respectively. A combined spectrum showing both the prolate and spherical stick spectra overlaid on the Si_{19} experimental spectrum is presented in Figure 9.11. There is a general trend that the first orbital states are of p-character and then they more to a combination of s and p character and then electrons in the low eKE range come from orbitals of primarily s character alone.
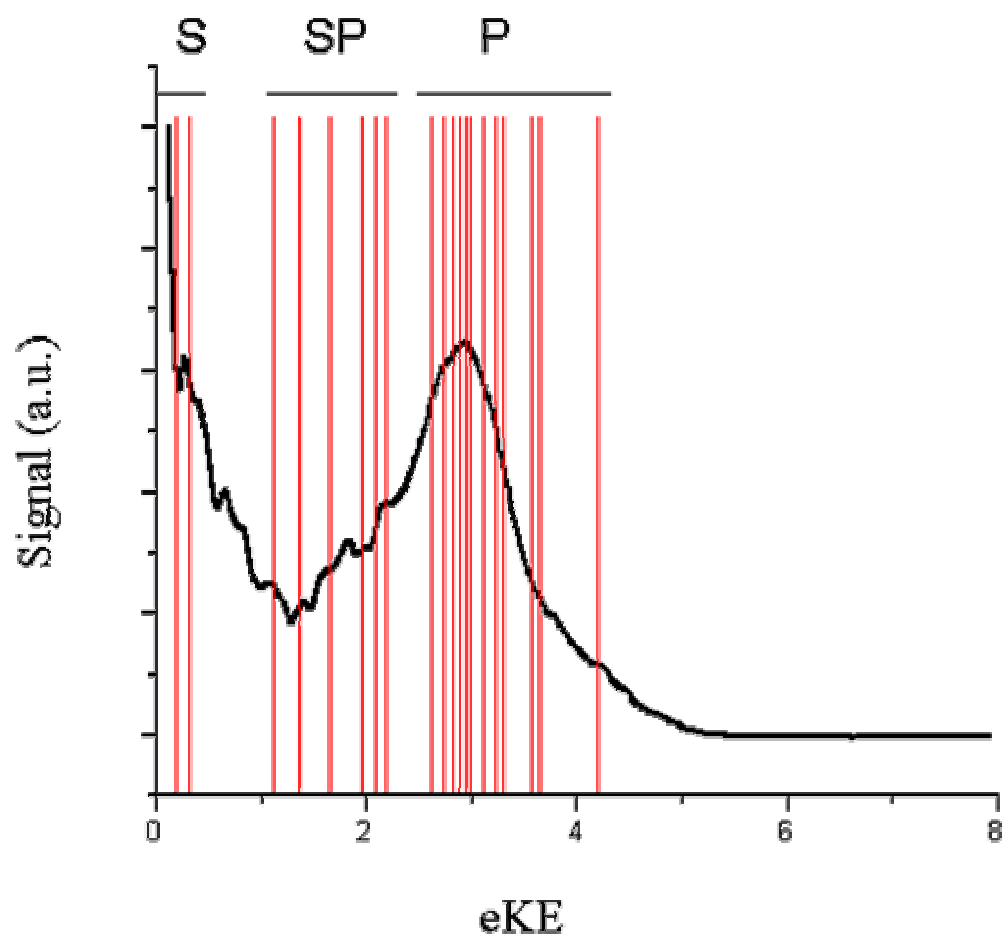
Figure 7.8 – Stick spectra from the calculated prolate geometry of Si_{18} overlaid on the experimental spectrum.
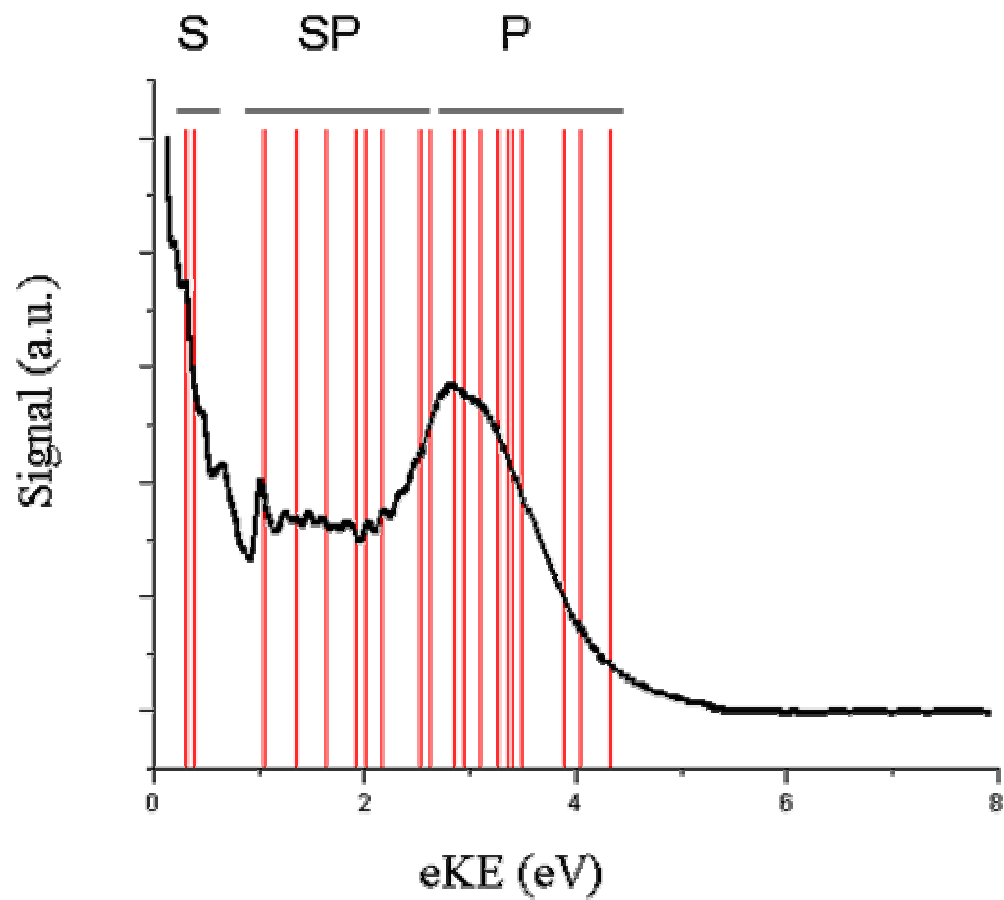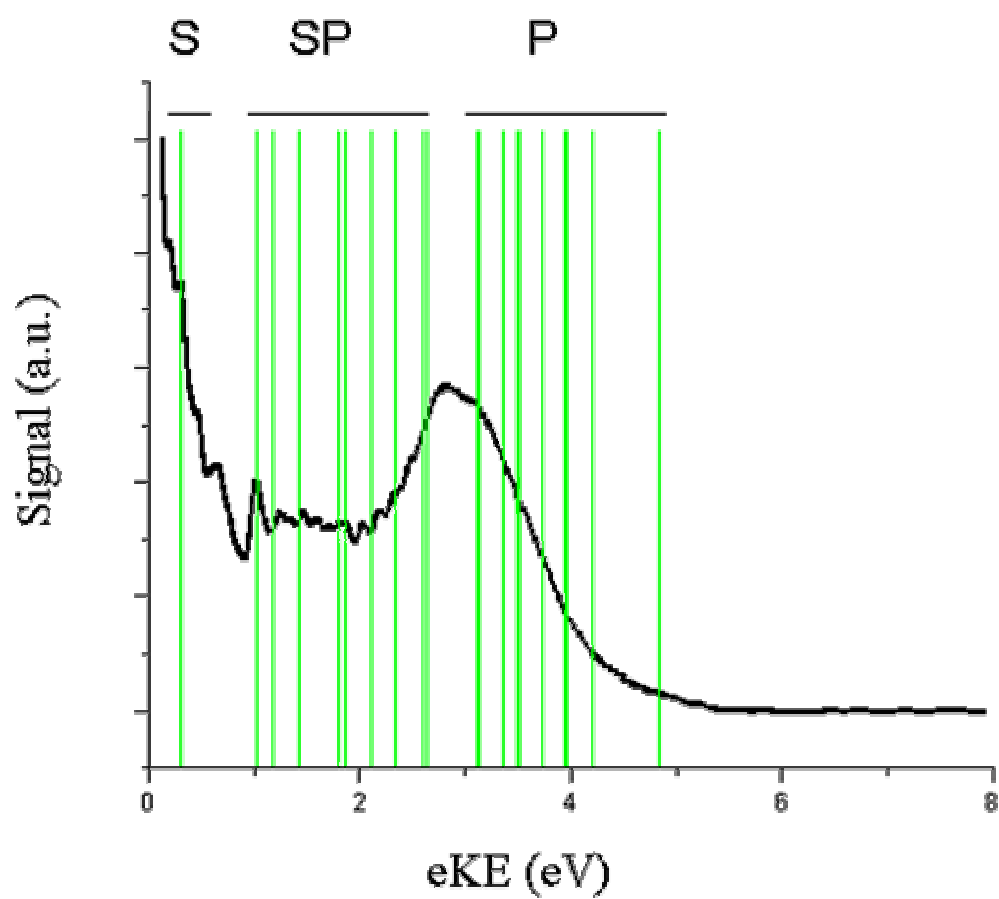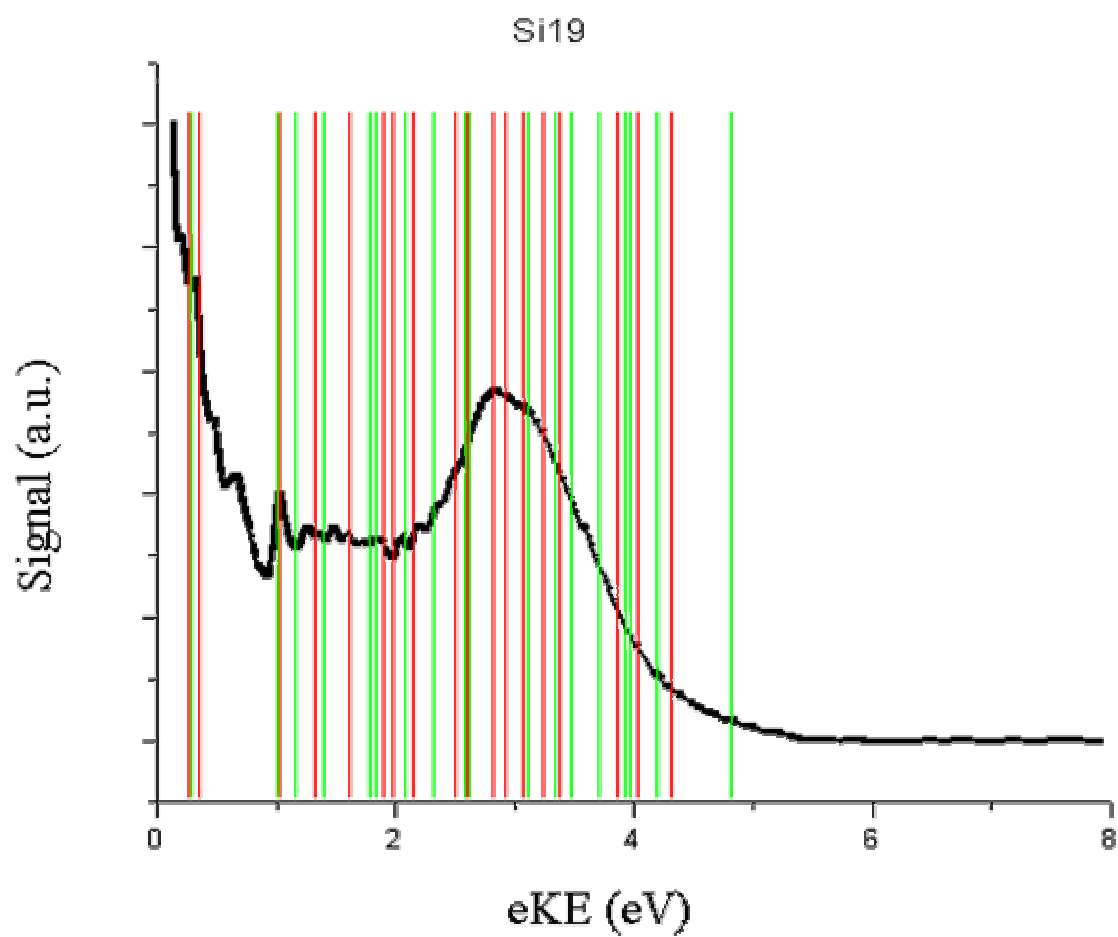
Figure 7.9 – Stick spectra from the calculated prolate geometry of Si_{19} overlaid on the experimental spectrum.

Figure 7.10 – Stick spectra from the calculated spherical geometry of Si_{19} overlaid on the experimental spectrum.

Figure 7.11 – Stick spectra from the calculated prolate and spherical geometry of Si_{19}

overlaid on the experimental spectrum.

Discussion:

There is a fairly clear change in the overall shape of the spectra going from Si_{18} to Si_{19}. This "filling in" trend in the spectra seems to correspond to the studies of Jarrold and coworkers in their ion mobility studies where after Si_{19}, a change from prolate geometries being the lowest energy structures to more spherical cage-like geometries dominating[2]. The stick spectra for Si_{18} and Si_{19} show the energies of the electronic states over that range. For Si_{19}, the spectra for both prolate and spherical geometries can be present. This may be the cause of the filling in of states and is explored more in Figure 9.11. Sieck et. al. found in their studies of silicon clusters containing 25, 29, and 35 atoms that as the number of atoms increased, the most stable clusters become less prolate and more spherical[24]. It seems that in our spectra as the clusters increase in size, they begin to loose the first hump in the spectra. This may be in part due to the prolate isomers becoming less common. As the number of atoms increases, the possibility for multiple isomers close in energy also increases. This may explain why the spectra for clusters containing more atoms are so cluttered. The number of close-lying geometries increases leading to many states close in energy.

The orbital character of the clusters is also of interest. In bulk crystalline silicon, the first band is from p orbitals alone, the second band is from s and p character, and the third band is from s orbital character. The density of states calculations for bulk silicon[25] are also similar to the anion PE spectra of larger silicon clusters. This is not an exact comparison because many of the eigenvalues

presented in the stick spectra have combined orbital character. There is a general trend and shows in part how the clusters are starting to emulate the bulk-like material.

Conclusion:

Anion PE spectra of silicon clusters up to 35 atoms have been taken. As the number of silicon atoms in a cluster increases, the bands start to have a "filling-in" effect. This can be in part explained by the geometry shift from prolate to more spherical clusters. The clusters containing more atoms may have many close lying isomers causing the spectra to be more cluttered appearing blob-like. The orbital character of the clusters is similar to the bulk-like crystalline material in a general sense, although the orbital character is not as well defined as it is in the bulk photoemission spectra.

References:

1. Meloni, G., et al., *Probing the connection between cluster and bulk electronic structure of InP using vacuum ultraviolet anion photoelectron spectroscopy.* Chemical Physics Letters, 2004. **392**(1-3): p. 90-94.

2. Ho, K.-M., et al., *Structures of medium-sized silicon clusters.* Nature, 1998. **392**(6676): p. 582-585.

3. Hudgins, R.H., et al., *High-resolution ion mobility measurements for silicon cluster anions and cations.* Journal of Chemical Physics, 1999. **111**(17): p. 7865-7870.

4. Jarrold, M.F. and V.A. Constant, *Silicon cluster ions: evidence for a structural transition.* Physical Review Letters, 1991. **67**(21): p. 2994-2997.

5. Shvartsburg, A.A., et al., *Structural information from ion mobility measurements: applications to semiconductor clusters.* Chemical Society Reviews, 2000. **30**(1): p. 26-35.

6. Muller, J., et al., *Spectroscopic evidence for the tricapped trigonal prism structure of semiconductor clusters.* Physical Review Letters, 2000. **85**(8): p. 1666-1669.

7. Tekin, A. and B. Hartke, *Global geometry optimization of small silicon clusters with empirical potentials and at the DFT level.* Physical Chemistry Chemical Physics, 2004. **6**(3): p. 503-509.

8. Kitsopoulos, T.N., et al., *Vibrationally resolved photoelectron spectra of Si3 and Si4.* Journal of Chemical Physics, 1990. **93**(8): p. 6108-6110.

9.   Arnold, C.C. and D.M. Neumark, *Study of Si4 and Si4 using threshold photodetachment (ZEKE) spectroscopy.* Journal of Chemical Physics, 1993. **99**(5): p. 3353-3362.

10.   Xu, C., et al., *Vibrationally resolved photoelectron spectroscopy of silicon cluster anions Sin (n = 3-7).* Journal of Chemical Physics, 1998. **108**(4): p. 1395-1406.

11.   Honea, E.C., et al., *Raman spectra of size-selected silicon clusters and comparison with calculated structures.* Nature, 1993. **366**(6450): p. 42-44.

12.   Li, S., et al., *Si3---Si7. Experimental and theoretical infrared spectra.* Chemical Physics Letters, 1995. **243**(3-4): p. 275-280.

13.   Fulara, J., et al., *Electronic absorption spectra of Sin and Sin (n=2-4) in neon matrices.* Journal of Physical Chemistry, 1996. **100**(46): p. 18042-18047.

14.   Raghavachari, K. and C. McMichael Rohlfing, *Bonding and stabilities of small silicon clusters: a theoretical study of Si7-Si10.* Journal of Chemical Physics, 1988. **89**(4): p. 2219-2234.

15.   Raghavachari, K. and C.M. Rohlfing, *Electronic structures of the negative ions Si2-Si10: electron affinities of small silicon clusters.* Journal of Chemical Physics, 1991. **94**(5): p. 3670-3678.

16.   Rohlfing, C.M. and K. Raghavachari, *Electronic structures and photoelectron spectra of Si[sup -][sub 3] and Si[sup -][sub 4].* The Journal of Chemical Physics, 1992. **96**(3): p. 2114-2117.

17.   Rothlisberger, U., W. Andreoni, and M. Parrinello, *Structure of nanoscale silicon clusters.* Physical Review Letters, 1994. **72**(5): p. 665-668.

18.   Mitas, L., et al., *Silicon clusters of intermediate size: energetics, dynamics, and thermal effects.* Physical Review Letters, 2000. **84**(7): p. 1479-1482.

19.   Rata, I., et al., *Single-parent evolution algorithm and the optimization of Si clusters.* Physical Review Letters, 2000. **85**(3): p. 546-549.

20.   Zhu, X.L., et al., *Structures and stability of medium silicon clusters. II. Ab initio molecular orbital calculations of Si12-Si20.* Journal of Chemical Physics, 2004. **120**(19): p. 8985-8995.

21.   Xu, C.S., et al., *Photoelectron spectroscopy of C-4(-), C-6(-), and C-8(-).* Journal of Chemical Physics, 1997. **107**(9): p. 3428-3436.

22.   Yoo, S., et al., *Endohedral Silicon Fullerenes SiN (27 N 39).* J. Am. Chem. Soc., 2004. **126**(42): p. 13845-13849.

23.   Frisch, M.J., et al., *GAUSSIAN 98.* 1998, Gaussian Inc.: Pittsburg, PA.

24.   Sieck, A., T. Frauenheim, and K.A. Jackson, *Shape transition of medium-sized neutral silicon clusters.* Physica Status Solidi B, 2003. **240**(3): p. 537-548.

25.   Tsay, Y.F., D.K. Paul, and S.S. Mitra, *Electronic Structure and Optical Properties of Amorphous Ge and Si.* Physical Review B, 1973. **8**: p. 2827-2832.

Chapter 8.   Studies of aluminum oxide clusters†

Introduction:

Amorphous aluminum oxide based catalysts are among the most widely employed solid acid catalysts. They are used in the isomerization of olefins, paraffins, and alkyl aromatics, alkylation of aromatics with alcohols and olefins, and olefins oligomerization and catalytic cracking[1]. They serve as supports or catalytic components for other reactions, such as combustion of methane[2], denitrogenation of nitrogen-containing heteroaromatic compounds[3], and dimerization of olefins[4]. The importance of these catalysts has motivated a large number of experimental and theoretical studies to understand the interaction of aluminum with oxygen from a molecular point of view. Recently, the identification of the presence of corundum (Al_2O_3) in stellar grains[5] has stimulated a new interest in aluminum oxide species and how these are formed from the reaction $Al + O_2$. These considerations have motivated a series of experiments in which the photoelectron (PE) spectra of size-selected $Al_xO_y^-$ anions have been measured in order to characterize the structural motifs and trends in the anion and neutral clusters, in particular their dependence on size and stoichiometry. In this chapter, additional studies of this type, covering $Al_xO_y^-$ clusters with as many as seven aluminum atoms are presented. This study represents the continuation of our investigations to understand the electronic and vibrational structure of group 13 element-containing clusters, such as B_xN_y[6, 7], Al_xP_y[8], Ga_xP_y[9], Ga_xAs_y[10] and In_xP_y[11, 12].

Wang and coworkers[13, 14] reported the first PE spectra of aluminum oxide

† published previously as: PCCP **5** 4073 (2003).

cluster anions, specifically $Al_xO_y^-$ ($x = 1$–2, $y = 1$–5) and $Al_3O_y^-$ ($y = 0$–5). These spectra yielded mainly unstructured bands corresponding to transitions between various anion and neutral electronic states, with partially-resolved vibrational structure seen only for $Al_3O_3^-$. Varying the ion source conditions caused the relative intensities of the two lowest energy bands in the PE spectra of $Al_3O_2^-$ and $Al_3O_3^-$ to change considerably, suggesting that these bands originate from different anion isomers. A somewhat higher resolution PE spectrum of $Al_3O_3^-$ was measured by Akin and Jarrold[15], who also confirmed the presence of multiple isomers of $Al_3O_3^-$ in a hole-burning experiment[16].

Electronic structure calculations by Ghanty and Davidson[17], Martinez *et al.*[18, 19], and Cui et al.[20] have proved invaluable in interpreting the PE spectra. These calculations showed that Al_3O_2 and Al_3O_3 each have two nearly degenerate isomers with rather different geometries: planar "V" and "kite" structures for Al_3O_2, and kite and "book" structures for Al_3O_3. These structures are shown in Figure 8.1. Density functional theory (DFT) calculations by Ghanty and Davidson[17] find the V isomer to be the ground state for $Al_3O_2^-$ and Al_3O_2, while for Al_3O_3 the energy ordering is reversed in the anion and neutral; the book is the lowest energy structure for $Al_3O_3^-$, while the kite is the ground state for Al_3O_3. The most recent calculation by Martinez *et al.*[18], a B3LYP/6-311+G(2d,p) DFT calculation with further optimization at the quadratic configuration interaction (QCISD) level, predicts the energy ordering of the isomers to be reversed in the anion and neutrals of both species. The kite is the global minimum for $Al_3O_2^-$, while the V is the ground state for Al_3O_2, and for Al_3O_3 the orderings are the same as those found by Ghanty and Davidson[17]. These energy

131

reversals are attributed to less positive charge and hence less Coulombic repulsion between the Al atoms in the anions.
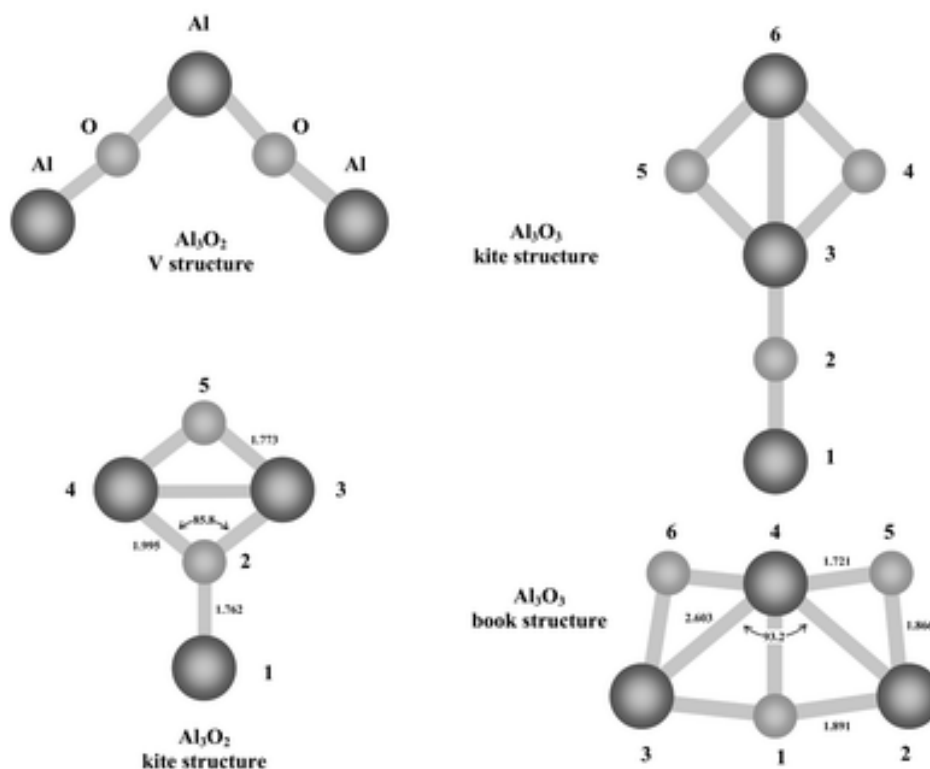
Figure 8.1 – Structures of the Al_3O_2 and Al_3O_3 clusters optimized at the B3LYP/cc-pVDZ level of theory. The bond lengths, in Å, and angles, in °, are for the $^2A_1$ excited electronic states.

For both anions, the calculated energy differences between the two isomers are less than 1 kcal mol^{-1}, with considerably larger splittings ($\sim$10 kcal mol^{-1}) for the neutral isomers. As a result, for each species, both anion isomers should be populated in the PE spectroscopy experiments, and the lowest energy bands in the PE spectra should correspond to transitions between the higher energy anion isomers to the ground state neutral structures (i.e. V–V for $Al_3O_2^-$ and kite-kite for $Al_3O_3^-$). In the experimental spectra[13-16], the relative intensities and the vibrational structure of

132

the lowest energy band for $Al_3O_3^-$ are consistent with the proposed assignments, but a more definitive assignment of the $Al_3O_2^-$ spectrum would be aided by the observation of resolved vibrational structure.

In this paper, we report the first vibrationally resolved PE spectra of $Al_3O_2^-$ at photodetachment energies of 3.493 and 4.661 eV, and somewhat better-resolved PE spectra of $Al_3O_3^-$ than previously. Electronic structure calculations at the Gaussian 2 (G2) level are carried out in order to refine the energetics of the anion and neutral isomers. Franck–Condon simulations of the vibrational structure in the spectra yield information on the anion and neutral vibrational frequencies and the geometric changes that occur upon photodetachment. We also present the first PE spectra of the $Al_4O_x^-$ and $Al_5O_x^-$ cluster series and of the $Al_6O_5^-$ and $Al_7O_5^-$ clusters, using what we have learned from the smaller clusters to assign some of the features in these spectra.

Experimental:

The negative ion photoelectron spectrometer used in this investigation has been described in detail previously[21, 22]; only a brief description will be given here. $Al_xO_y^-$ anions were produced in a pulsed laser vaporization molecular beam source using argon as carrier gas. A rotating and translating disk of AlN ceramic (>95% dense) or Al is ablated with the second harmonic (2.331 eV, 18 mJ/pulse) of a pulsed Nd:YAG laser. The laser pulses are focused onto the target with a 50 mm lens. The presence of $Al_xO_y^-$ clusters in the molecular beam arises from surface oxidation of the AlN or Al targets. The resulting plasma is entrained in a pulse of Ar carrier gas from a piezoelectric valve. The plasma is expanded through a 19 mm long clustering channel and then passes through a skimmer into a differentially pumped region.

Negative ions formed during the expansion are extracted perpendicularly to their flow direction by a pulsed electric field and accelerated to a beam energy of 2.5 keV. The extracted ions enter a linear reflectron time of flight (TOF) mass spectrometer, where they are separated in time and space according to their mass-to-charge ratios. The TOF mass spectrometer resolution is m/Δm $\approx$ 2000. For this particular experiment the instrument is operated at a repetition rate of 18 Hz.

Mass-selected anions are selectively photodetached with a fixed frequency Q-switched Nd:YAG probe laser. The third (355 nm, 3.493 eV) and fourth (266 nm, 4.661 eV) harmonics were used in this study. The laser is timed so as to photodetach ions of the desired mass. The photoelectron kinetic energy (eKE) is then analyzed by time-of-flight using a 1 m, field-free flight tube. The eKE scale is calibrated using the PE spectra of Cl^-, Br^-, and I^- at 266 nm and O_2^- at 355 nm. The energy resolution is 8–10 meV for an eKE of 0.65 eV and degrades as $(eKE)^{3/2}$ at higher eKE. The PE spectra were taken at two laser polarization angles, 0° and 90° with respect to the direction of electron detection. The laser polarization can be rotated using a half-wave plate.

All photoelectron spectra presented here are plotted as a function of the electron binding energy (eBE) defined as

$$EBE = h\nu - eKE = EA + E^{(0)} - E^{(-)} \tag{10.1}$$

where $h\nu$ = 3.493 and 4.661 eV is the photodetachment energy, EA is the electron affinity of the neutral cluster, and $E^{(0)}$ and $E^{(-)}$ are the internal (electronic + vibrational) energies of the neutral and anion, respectively.

Results:

The 355 and 266 nm PE spectra of $Al_3O_2^-$ and $Al_3O_3^-$ are shown in Figure 8.2 and 8.3, respectively. The 266 nm PE spectra of $Al_4O_x^-$ and $Al_5O_x^-$ ($x = 3–5$) are presented in Figure 8.4 and those of $Al_6O_5^-$ and $Al_7O_5^-$ in Figure 8.5. We report only the PE spectra taken at a laser polarization angle of 0° with respect to the flight tube axis; spectra at 90° are similar but lower in intensity. The photoelectron signal is plotted as a function of eBE. At 266 nm, three distinct spectral features are revealed by photodetachment of the $Al_3O_2^-$ and $Al_3O_3^-$ clusters and are labeled X', X, and A. The 266 nm PE spectra of the larger clusters exhibit several unresolved bands, labeled in alphabetical order.

The 355 nm PE spectrum of $Al_3O_2^-$ shows a weak band, band X', followed by a much stronger band, band X. Band X', beginning around 1.5 eV, shows no obvious vibrational structure, but band X shows a partially resolved vibrational progression with a peak spacing of approximately 430 cm^{-1}. The apparent origin of this band is at 2.17 eV. Band A, seen at 266 nm, shows a well-resolved vibrational progression with an apparent origin of 3.40 eV and a frequency of 410 cm^{-1}. Although all three bands were seen previously, no vibrational structure was observed in either band X or A.
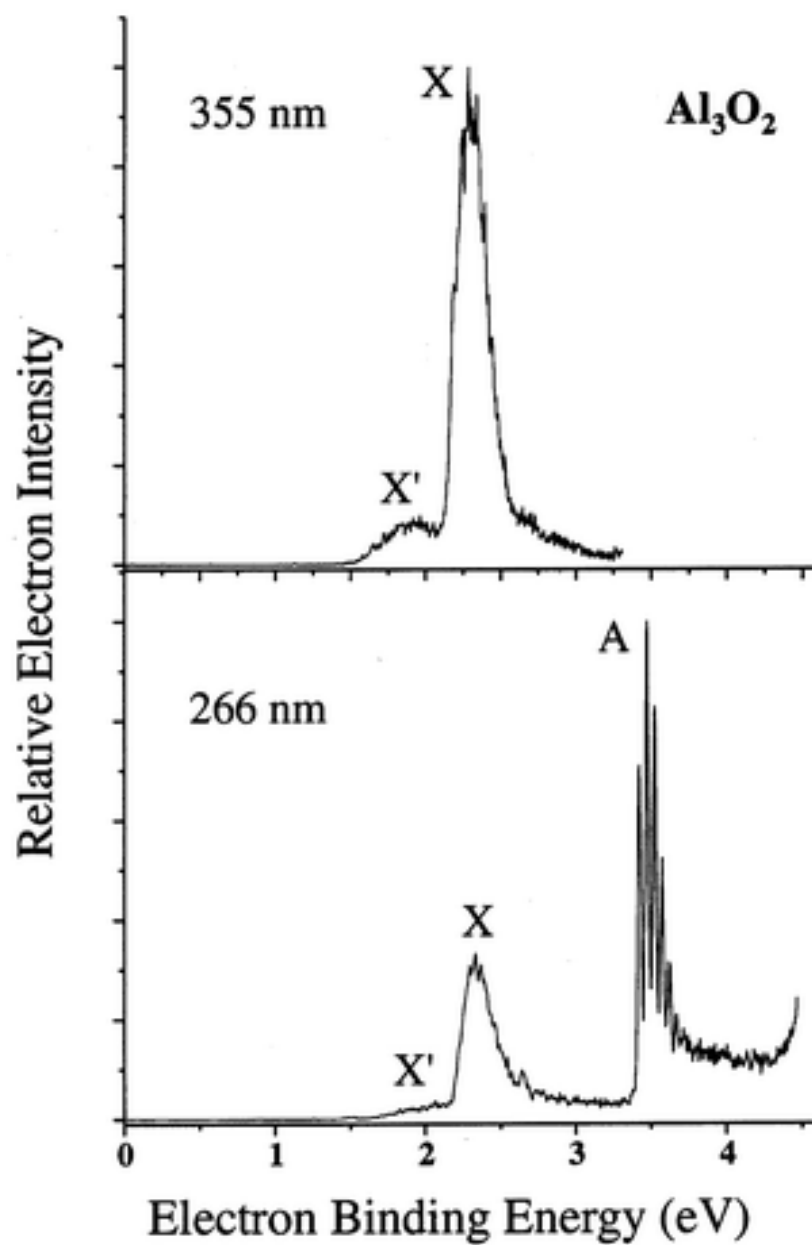
Figure 8.2 – Photoelectron spectra of $Al_3O_2^-$ at 355 nm (top) and 266 nm (bottom).

The laser polarization angle was 0°.
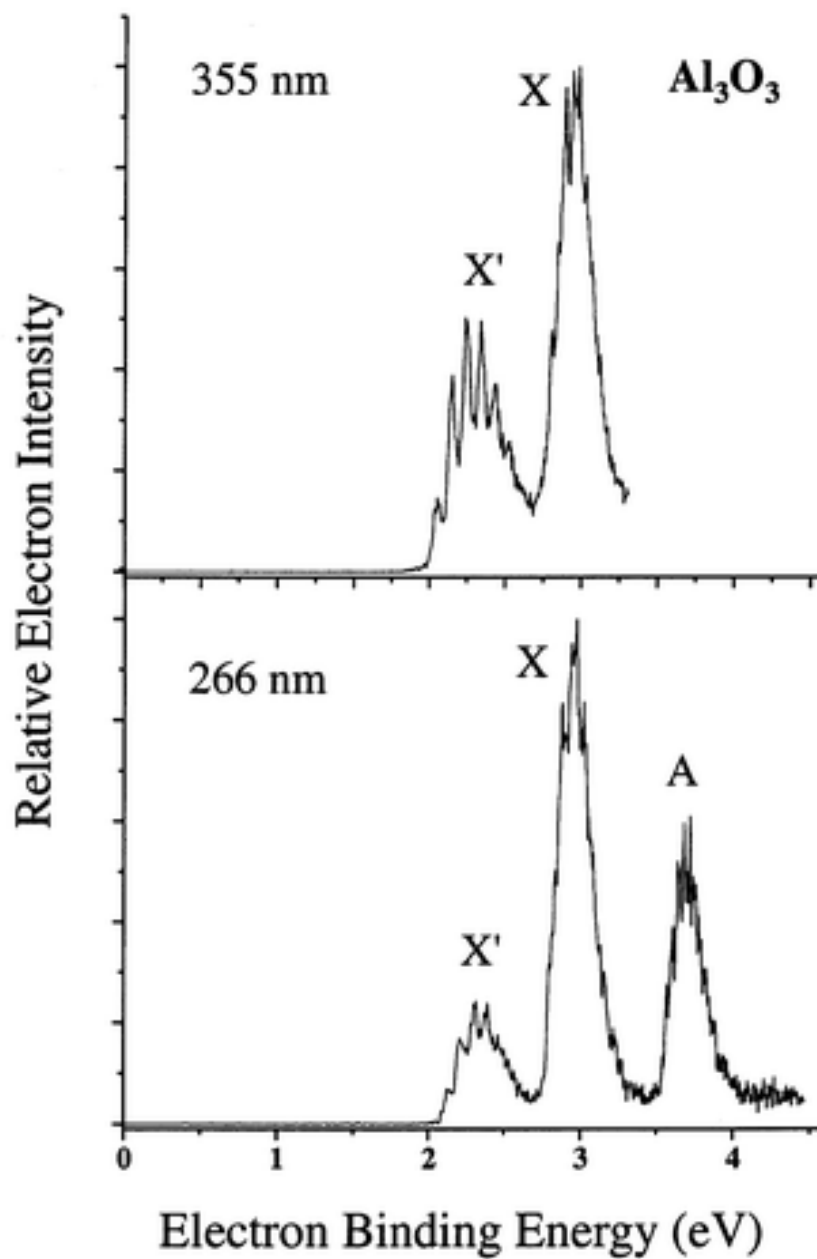
Figure 8.3 – Photoelectron spectra of Al$_3$O$_3^-$ at 355 nm (top) and 266 nm (bottom).

The laser polarization angle was 0°.
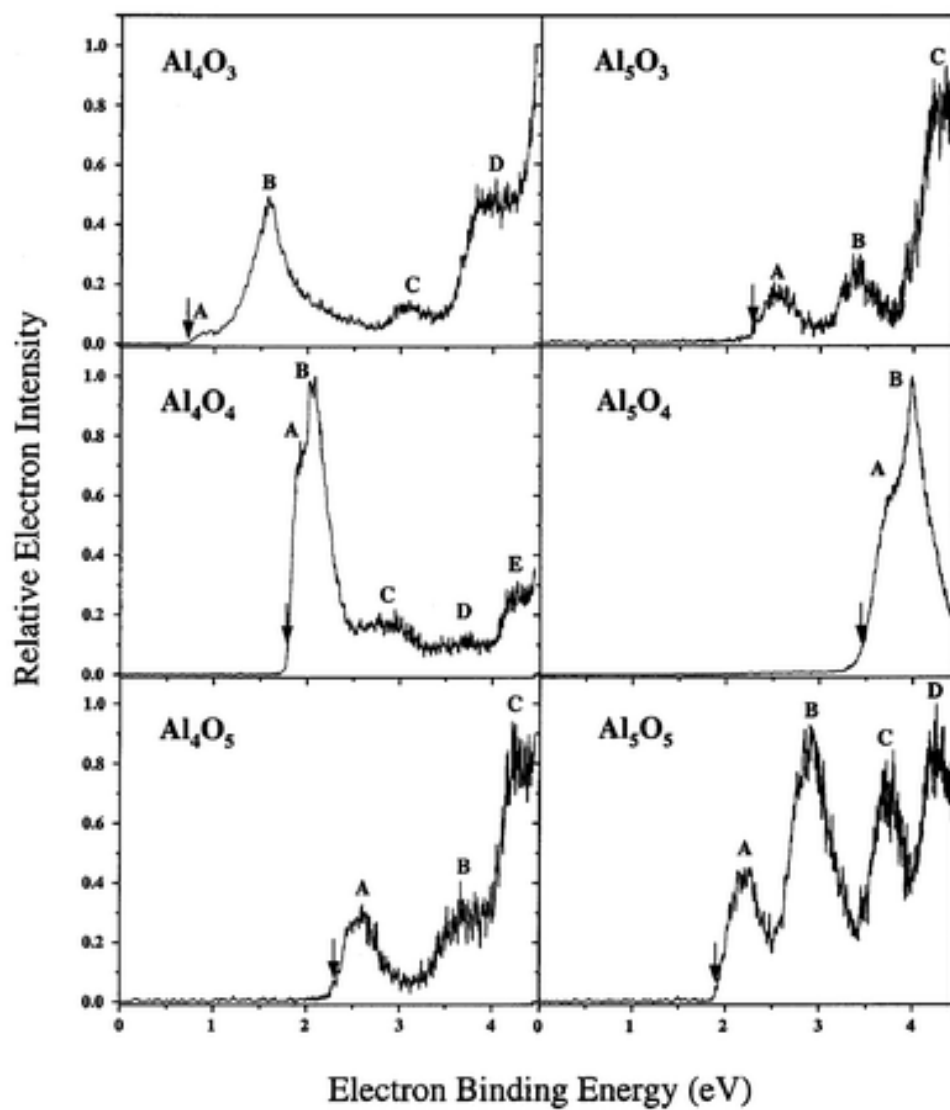
Figure 8.4 – Photoelectron spectra of $Al_4O_x^-$ and $Al_5O_x^-$ ($x = 3-5$) at 266 nm. The

laser polarization angle was 0°.

Figure 8.5 – Photoelectron spectra of $Al_6O_5^-$ and $Al_7O_5^-$ at 266 nm. The laser polarization angle was 0°.

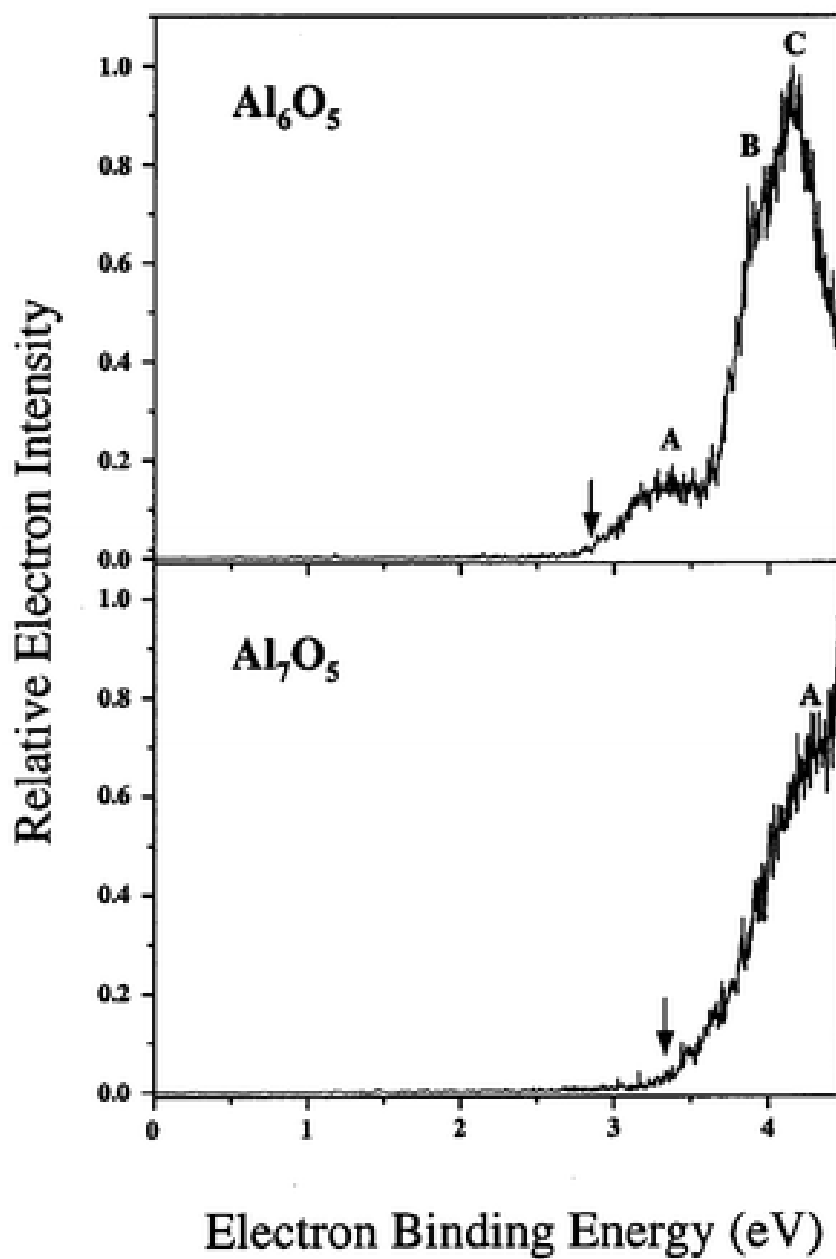All three bands in the PE spectra of $Al_3O_3^-$ show partially-resolved vibrational progressions. The apparent vibrational origin for band X′ is at 2.06 eV, and the spectrum shows a single vibrational progression with a frequency of approximately 770 cm^{-1}. The vibrational structure of band X is more complex; multiple modes appear to be active with partially resolved features spaced by approximately 400 cm^{-1}. Band A exhibits a 300 cm^{-1} progression with its origin at 3.60 eV. Vibrational structure in bands X′ and X was seen previously, but no structure in band A was observed in the earlier work. The X″/X intensity ratio is considerably larger in the $Al_3O_3^-$ spectra than in the $Al_3O_2^-$ spectra.

The 266 nm PE spectra of the larger clusters, $Al_4O_x^-$, $Al_5O_x^-$ ($x = 3–5$), $Al_6O_5^-$, and $Al_7O_5^-$ do not show vibrationally resolved spectral features. Several structureless bands are revealed by photodetachment and labeled in alphabetical order. The vertical detachment energies (VDE) for each band, corresponding to the band maxima, are listed in Table 10.1, as are the lowest adiabatic detachment energies (ADE), the apparent origins for the lowest energy bands. The ADEs increase within a cluster series with the exception of Al_5O_5, for which band A occurs at lower eBE than the corresponding band for Al_5O_4 and Al_4O_5. The photoelectron spectrum of $Al_7O_5^-$ obtained with 4.661 eV photon energy shows only the onset of band A.

140

Cluster	VEDE	ADE[a]
Al_4O_3	0.94 (A), 1.58 (B), 3.10 (C), 4.09 (D)	0.73(15)
Al_4O_4	1.93 (A), 2.05 (B), 2.83 (C), 3.73 (D), 4.31 (E)	1.78(6)
Al_4O_5	2.59 (A), 3.80 (B), 4.32 (C)	2.30(15)
Al_5O_3	2.56 (A), 3.39 (B), 4.31 (C)	2.20(15)
Al_5O_4	3.83 (A), 3.99 (B)	3.44(10)
Al_5O_5	2.22 (A), 2.91 (B), 3.74 (C), 4.26 (D)	1.89(15)
Al_6O_5	3.40 (A), 4.04 (B), 4.15 (C)	2.82(10)
Al_7O_5	4.35 (A)	3.36(15)
[a] This is the adiabatic detachment energy of band A.		

Table 8.1 – Vertical and adiabatic electron detachment energies, in eV, of larger

aluminum oxide clusters.

To aid in interpretation of the measured PE spectra, we carried out DFT

electronic structure calculations on four structural isomers: the V and kite

configurations for Al_3O_2 and $Al_3O_2^-$ species, and the kite and book structures for

Al_3O_3 and $Al_3O_3^-$. We calculated the optimized geometry, energetics, and vibrational

frequencies for the lowest electronic states of each of the anion and neutral isomers,

and for the first excited states of the Al_3O_2 kite and Al_3O_3 book isomers.

The computations were performed using the GAUSSIAN98 program suite[23]. The level of theory employed was the DFT method using the Becke three-parameter exchange functional with the Lee, Yang, and Parr correlation functional (B3LYP). The correlated consistent polarized valence double-ζ basis set (cc-pVDZ) was used for optimizing geometries and vibrational frequencies, and the consistent polarized valence triple-ζ basis set (cc-pVTZ) was used for the energetics of the optimized geometries. We also used the G2 model to perform high accuracy energy calculations on the ground states of the two most stable isomers of $Al_3O_2^-/Al_3O_2$ and $Al_3O_3^-/Al_3O_3$ to gain reliable isomerization energies (ΔE_{isom}). The G2 method is known for its reliability in evaluating thermochemical data[24] of molecules composed of first- and second-row atoms.

Results from the B3LYP and G2 calculations are summarized in Table 8.2. All calculated structures are planar and have C_{2v} symmetry. The B3LYP geometries calculated for the lowest electronic states of each anion and neutral isomer are essentially identical to those calculated previously by Ghanty and Davidson[17] and Martinez et al.[18], and are not enumerated here. However, the geometries of the first excited states of the Al_3O_2 kite and Al_3O_3 book isomers were not reported previously and are shown in Figure 8.1. Molecular orbital (MO) energy diagrams for the two lowest energy structures of $Al_3O_2^-$ and $Al_3O_3^-$ are similar to those reported by Ghanty and Davidson[17].

Species	Structure	State	B3LYP[a]			G2		
			ADE_e	ΔE_{isom}[b]	T_e	ADE_e	ΔE_{isom}[b]	T_e
$Al_3O_2^-$	Kite-shape	$^1A_1$			0.000			0.000
	V-shape	$^1A_1$		–0.065	–0.056		0.145	0.125
Al_3O_2	V-shape	$^2A_1$	1.393		0.000	1.601		0.000
	Kite-shape	$^2B_2$	1.894	0.562	0.557	2.442	0.605	0.716
	Kite-shape	$^2A_1$	3.026		1.689			
$Al_3O_3^-$	Book-shape	$^1A_1$			0.000			0.000
	Kite-shape	$^1A_1$		0.051	0.046		0.104	0.090
Al_3O_3	Kite-shape	$^2A_1$	1.978		0.000	2.197		0.000
	Book-shape	$^2B_2$	2.518	0.508	0.495	3.044	0.717	0.757
	Book-shape	$^2A_1$	3.182		1.159			

[a] Using cc-pVTZ basis sets. [b] Including zero-point vibrational energy correction.

Table 8.2 – Results of the electronic structure calculations of $Al_3O_2^-$, Al_3O_2, $Al_3O_3^-$, and Al_3O_3. Adiabatic detachment energies, isomerization energies, and term energies are in eV.

The electronic term energy T_e is given for each anion and neutral state; ΔE_{isom} is the energy difference between the electronic and vibrational (assuming harmonic zero-point energy corrections) ground states of the two isomers for each anion and neutral species. For each neutral state, the ADE is listed; this is the energy difference between its vibrational ground state and that of the lowest energy anion isomer.

The results in Table 8.2 are similar to the previous DFT calculations by Ghanty and Davidson[17] and Martinez et al[18, 19]. In particular, we find the energetic ordering of the Al_3O_3 isomers to be reversed in the anion and neutral, with kite and book isomers being the lowest energy structures for $Al_3O_3^-$ and Al_3O_3, respectively, just as in the earlier work. However, the energetic ordering of the $Al_3O_2^-$ isomers depends on the method and basis set used. At the B3LYP/aug-cc-pVTZ level

of theory, the anion and neutral have the same energetic ordering with the anion V-shape 0.39 kcal mol^{-1} (17 meV) lower in energy than the kite-shape, similar to the results of Ghanty and Davidson. In the B3LYP/cc-pVTZ calculation, this difference is increased to 65 meV. With the smaller cc-pVDZ basis set, the ordering is inverted with the anion kite 83 meV lower in energy than the V, in agreement with the energy ordering found by Martinez et al[18, 19]. The G2 calculations, which are expected to yield more accurate energetics, predict the same energy orderings as those found by Martinez et al.[18, 19] for the Al_3O_2 and Al_3O_3 anions and neutrals, and predict that the splitting between the two $Al_3O_3^-$ isomers is smaller than that between the two $Al_3O_2^-$ isomers.

Discussion:

4.1. $Al_3O_2^-$

The electronic structure calculations described in the previous section leave some uncertainty regarding the ground state of $Al_3O_2^-$, and this uncertainty clearly affects the assignment of the experimental PE spectrum. If we assume that the energy orderings in the G2 calculations in Table 8.2 and reference 19 are correct, we can assign band X^s of the $Al_3O_2^-$ PE spectrum to the $^2A_1(V) \leftarrow {}^1A_1(V)$ transition, band X to the $^2B_2(\text{kite}) \leftarrow {}^1A_1(\text{kite})$ transition, and band A to the $^2A_1(\text{kite}) \leftarrow {}^1A_1(\text{kite})$ transition. The lower intensity of band X^s relative to bands X and A reflects the fact that band X^s originates from the slightly higher energy V anion isomer which is expected to be less populated than the kite isomer of $Al_3O_2^-$. If, on the other hand, the V isomer of $Al_3O_2^-$ is the ground state, then we would assign band X^s to the kite $\leftarrow$ kite transition originating from the excited anion isomer, and bands X and A to V $\leftarrow$

V transitions (the comparable intensities of bands X and A indicate that they both originate from the lowest energy anion isomer). The experimental splitting between bands X and A ($\approx$1.2 eV) supports the first assignment, because it is close to the calculated splitting between the ground $^2B_2$ and excited $^2A_1$ states of the neutral kite isomer; the calculated splitting between the ground and excited states of the neutral V isomer is much larger, 3.4 eV.

In order to test our preferred assignment, simulations of bands X^e, X, and A were performed within the Franck–Condon (FC) approximation. Using the B3LYP/cc-pVDZ force constants and optimized geometries for the initial state of the anion and the final state of the neutral, we determined the displacement in normal coordinates between the equilibrium structures of various states of $Al_3O_2^-$ and Al_3O_2, $Al_3O_3^-$ and Al_3O_3 within the parallel mode approximation assuming harmonic oscillator potentials. These normal mode displacements and the calculated vibrational frequencies served as the starting point in the simulations and were successively modified to reproduce the experimental PE spectra. Transition origins were taken from experiment and only the most active totally-symmetric modes were considered. The anion vibrational temperature used is 200 K for Al_3O_2 and 300 K for Al_3O_3. The parameters used in the simulations are listed in Table 10.3. Because some of the vibrational progressions are quite extended, we can obtain vibrational frequencies with higher accuracy than our experimental resolution. The simulated PE spectra are shown in Figure 8.6.
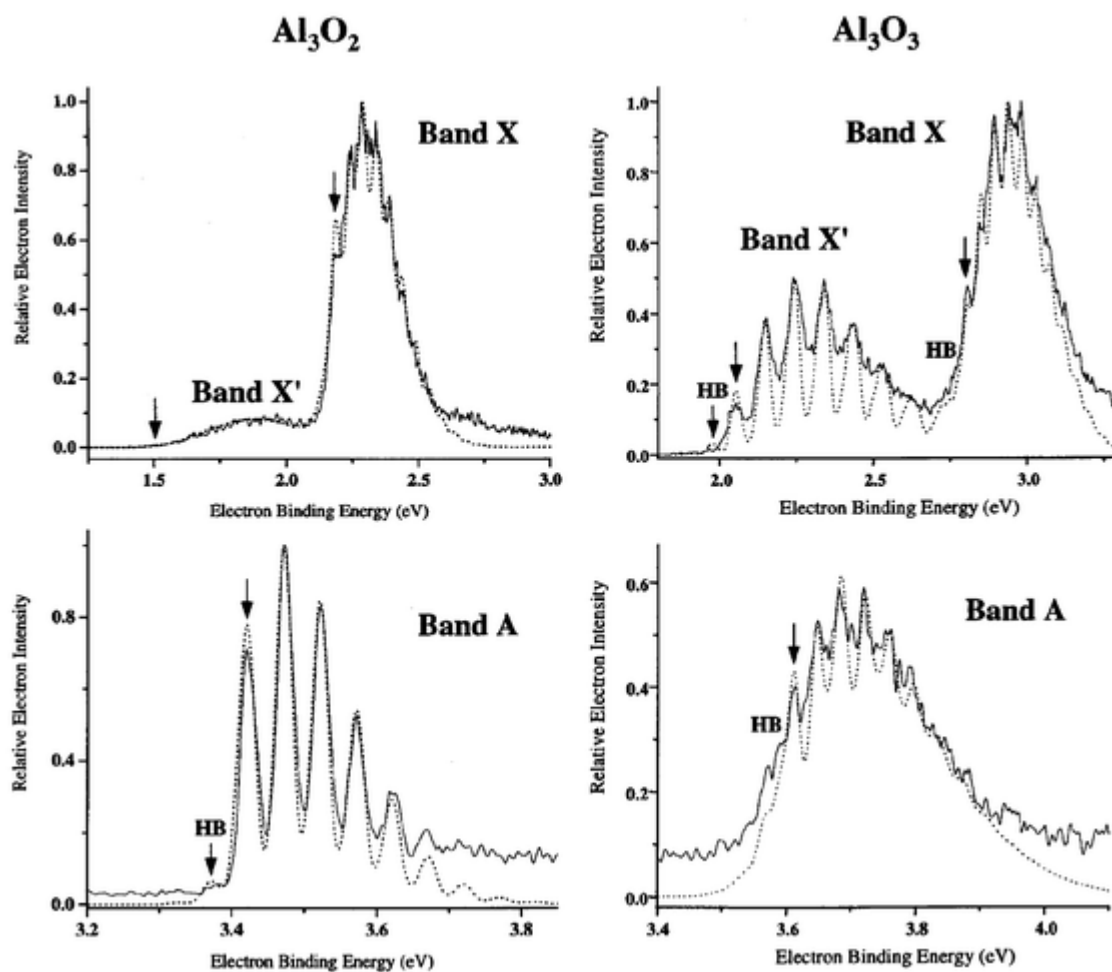
Figure 8.6 – Spectral simulations (dotted line) within the Franck–Condon

approximation superimposed to the experimental PE spectra.

No vibrational structure is observed for band X″ in the experimental PE spectrum, nor is any seen in the FC simulation of this band, assuming it is the V ⟵ V transition using the calculated normal coordinate displacements and vibrational frequencies. The reason for the absence of structure is seen in Table 8.3. There are substantial displacements in all four totally symmetric modes. In particular, ΔQ_4 is equal to 0.617 $amu^{1/2} \cdot Å$ for the low frequency vibrational mode $v^{(0)}_4$ (36 cm^{-1}), corresponding to the symmetric wag of the two terminal Al atoms. These displacements result from the large change in the ∠OAlO bond angle, from 99.8° for $Al_3O_2^-$ to 121.7° for Al_3O_2. As a result, there are overlapping extended progressions in a very low frequency mode, leading to an electronic band in the PE spectrum with no resolved vibrational structure.

At 355 nm, band X exhibits a partially resolved vibrational progression. From the Franck–Condon simulation we could fit band X using three vibrational active frequencies, in cm^{-1}: 329 ± 50 ($v^{(0)}_4$), 430 ± 30 ($v^{(0)}_3$), and 780 ± 50 ($v^{(0)}_1$). The most active mode is the $v^{(0)}_3$ mode, which can be described as the stretching of the two Al atoms in the ring of the kite, Al(3)–Al(4) in Figure 8.1. Activity in this mode results from a decrease in the Al(3)–Al(4) bond distance upon photodetachment, from 2.78 to 2.65 Å, according to the electronic structure calculations. The B3LYP computed vibrational frequencies agree well with those obtained in the simulation, and the normal coordinate displacements for the v_4 and v_1 modes used to simulate the spectrum are very close to those obtained from the electronic structure calculations. However, the value of ΔQ_3 needed to fit the progression is larger by a factor of 1.8 than the value from the calculated geometries.

147

Species	Band	Structure	State	$v^{(-)}$	$v^{(0)}$	ΔQ_i	ADE	T
Al_3O_2	X'	V-shape	$^2A_1$	v_4 = 41 (41)	36 (36)	0.617 (0.617)	1.50 ± 0.10	200
				v_3 = 235 (235)	237 (237)	0.886 (0.886)		
				v_2 = 436 (436)	444 (444)	1.138 (1.138)		
				v_1 = 954 (954)	962 (962)	0.045 (0.045)		
	X	Kite-shape	$^2B_2$	v_4 = 266 (266)	329 (329)	0.047 (0.040)	2.186 ± 0.010	200
				v_3 = 352 (352)	430 (417)	0.455 (0.258)		
				v_1 = 833 (833)	780 (780)	0.267 (0.238)		
	A	Kite-shape	$^2A_1$	v_3 = 352 (352)	415 (391)	0.473 (0.203)	3.419 ± 0.008	200
				v_2 = 671 (671)	663 (683)	0.077 (0.064)		
				v_1 = 833 (833)	768 (768)	0.134 (0.104)		
Al_3O_3	X'	Kite-shape	$^2A_1$	v_4 = 546 (546)	610 (573)	0.320 (0.223)	2.052 ± 0.010	300
				v_3 = 578 (578)	808 (726)	0.490 (0.447)		
	X	Book-shape	$^2B_2$	v_5 = 210 (210)	275 (245)	0.385 (0.275)	2.805 ± 0.012	300
				v_4 = 390 (412)	410 (427)	0.461 (0.329)		
				v_2 = 610 (664)	690 (623)	0.269 (0.095)		
				v_1 = 718 (718)	750 (699)	0.085 (0.055)		
	A	Book-shape	$^2A_1$	v_5 = 210 (210)	283 (256)	0.565 (0.421)	3.610 ± 0.015	300
				v_4 = 390 (412)	460 (439)	0.255 (0.212)		
				v_2 = 610 (664)	630 (630)	0.265 (0.201)		

Table 8.3 – Optimized parameters used in the spectral PE simulations within the Franck–Condon approximation. $v_i^{(-)}$, in cm^{-1}, is the ith vibrational frequency of the anion and $v_i^{(0)}$, in cm^{-1}, is the ith vibrational frequency of the neutral. The normal mode displacement ΔQ_i is in $amu^{1/2}$Å. ADEs are in eV and anion temperatures (T) in K. The values in parentheses are calculated at the B3LYP/cc-pVDZ level of theory.

The better-resolved vibrational structure in band A can be fit with a FC simulation using frequencies, in cm^{-1}, of 415 ± 30 ($v^{(0)}_3$), 663 ± 50 ($v^{(0)}_2$), and 768 ± 50 ($v^{(0)}_1$), with $v^{(0)}_3$ as the main active mode. The computed vibrational frequencies and normal coordinates for both the anion and the neutral are close to those that fit the spectrum, with the exception of ΔQ_3 which needed to be increased by a factor of 2.3 to fit the progression. A weak feature at 3.375 eV assigned as a hot band yields an anion vibrational frequency of $v_3^{(-)} = 350 \pm 80$ cm^{-1}.

Both simulations require that ΔQ_3 be increased by about factor of two over the calculated values based on the geometries obtained from the electronic structure calculations. This discrepancy can be reduced by adjusting the geometry of either the anion or both neutral states. The extent of the required geometry change was examined by modifying the geometry of the $^1A_1$ electronic state of $Al_3O_2^-$, keeping fixed the calculated geometries and force constants of the $^2B_2$ and $^2A_1$ states of Al_3O_2. Using a Al(3)–Al(4) bond distance of 3.02 Å, 0.18 Å longer than the optimized calculated value for the $^1A_1$ electronic state of $Al_3O_2^-$, we obtain normal mode displacements ΔQ_3 of 0.514 $amu^{1/2}$ Å for band X and 0.434 $amu^{1/2}$ Å for band A, in better agreement with the best-fit ΔQ_3 values in Table 8.3.

Overall, we find that all three bands in the $Al_3O_2^-$ PE spectra can be fit with relatively small adjustments to the calculated normal coordinate displacements, assuming the bands are assigned according to the energy ordering of the anion isomers yielded by the G2 calculations. Our analysis therefore confirms this assignment and energy ordering.

The electron affinity (EA) of Al_3O_2 is defined as the energy difference between the $v = 0$ levels of the anion and neutral electronic ground states, which in this case are the $^1A_1$ kite for $Al_3O_2^-$ and the $^2B_2$ V-structure for Al_3O_2. No transitions between these two different isomers are observed in the PE spectrum. We can, however, determine the EA from the experimental ADE for band X' and the calculated ΔE_{isom} for the anion isomers, or from the experimental ADE for band X and the calculated ΔE_{isom} for the neutral isomers, according to EA = ADE(X') + ΔE_{isom} (anion) or EA = ADE(X') − ΔE_{isom} (neutral). Using the values in Tables 8.2 and 8.3, these two determinations yield 1.65 and 1.58 eV, respectively, for the EA's. We select as our best estimate the average of the two values, (1.62 ± 0.12) eV for $EA(Al_3O_2)$. Here the overall error was estimated using the experimental resolution for bands X' and X together with the uncertainty of the computed value of ΔE_{isom}.

4.2. $Al_3O_3^-$

Based on their own electronic structure calculations and those by Ghanty and Davidson[17], Akin and Jarrold[15] assigned bands X' and X in their PE spectrum of $Al_3O_3^-$ to the $^2A_1$(kite) ← $^1A_1$(kite) and $^2B_1$(book) ← $^1A_1$(book) photodetachment transitions. Our electronic structure calculations are consistent with this assignment, and support the new assignment of band A in our spectrum to the $^2B_1$(book) ←

$^1A_1$(book) transition. The calculated G2 energetics in Table 8.2 indicate that the anion kite isomer is only 0.104 eV higher than book isomer of the anion. Hence, as in the $Al_3O_2^-$ PE spectrum, the lowest energy band does not originate from the anion ground state. However, the X'/X intensity ratio is clearly higher in the $Al_3O_3^-$ PE spectra than in the $Al_3O_2^-$ spectra, even though the ion source conditions were essentially the same when the PE spectra were taken for the two anions. This experimental observation is consistent with the G2 calculations, which show a smaller energy splitting between the two anionic isomers of Al_3O_3 than of Al_3O_2 ($\Delta E_{isom} = 0.145$ eV).

All three bands show resolved vibrational structure. The best-fit FC simulations are shown in Figure 8.6 and the parameters used in these simulations are listed in Table 8.3. Band X" comprises progressions in the two totally symmetric $v^{(0)}_4$ and $v^{(0)}_3$ modes with frequencies of 610 and 808 cm^{-1}, respectively, with most of the activity in the $v^{(0)}_3$ mode. The v_4 and v_3 modes correspond to symmetric stretch and distortion vibrations, respectively, of the kite "head". Activity in these mode results because the Al-O bond lengths in the "head" are longer and more asymmetric in the anion[17, 18]. The ADE for this band is found to be (2.052 ± 0.010) eV. The fitting parameters are all quite close to the calculated values, with the most notable difference being that $v^{(0)}_3$ frequency used to fit the band is 82 cm^{-1} higher than the calculated frequency.

A similar analysis for band X yields an ADE of (2.805 ± 0.012) eV. The FC simulation involved four vibrational active modes, in cm^{-1}: 275 ± 50 ($v^{(0)}_5$), 410 ± 30 ($v^{(0)}_4$), 690 ± 50 ($v^{(0)}_2$), and 750 ± 50 ($v^{(0)}_1$), with $v^{(0)}_4$, the symmetric stretching of Al(2) and Al(3) with respect to Al(4), as the main mode. The Al(2)–Al(3) bond

distance decreases from 2.52 Å to 2.34 Å upon photodetachment, according to the electronic structure calculations[17, 19]. The calculated frequencies agree with the best-fit values, but all of the calculated normal coordinate displacements are somewhat smaller than the best-fit values, indicating that the electronic structure calculations underestimate the geometry change upon photodetachment.

For band A, we find the ADE to be 3.610 eV, yielding a splitting between the neutral $^2A_1$ and $^2B_2$ "book" states of (0.805 ± 0.015) eV. This band was fit assuming three a_1 modes are the most active with the following frequencies, in cm^{-1}: 283 ± 30 ($v^{(0)}_5$), 460 ± 50 ($v^{(0)}_4$), and 630 ± 50 ($v^{(0)}_2$), with $v^{(0)}_5$ as the main mode. Two anion frequencies are derived as 210 ± 80 and 390 ± 80 cm^{-1} from the FC simulations; these frequencies yielded the best fit to the spectrum, but do not correspond to isolated transitions and are thus quite uncertain. The agreement for the calculated modes with the best-fit values is good. The normal mode displacement of $v^{(0)}_5$ is somewhat larger than the value obtained from the optimized geometries and force constants at the B3LYP/cc-pVDZ level of theory. The v_5 mode can be described as the bending of the two Al atoms with respect to the central Al(4). The ΔQ_5 underestimation suggests that the calculated $\angle$Al(2)-Al(4)-Al(3) angle change of $4.4°$ between the anionic ground state and the neutral excited state of Al_3O_3 is too small.

We can extract an approximate EA(Al_3O_3) using the G2 values for ΔE_{isom}(anions) and ΔE_{isom}(neutrals). Following the same approach as for the evaluation of EA(Al_3O_2), we obtained the values of 2.16 and 2.09 eV from the experimental ADE's associated with bands X' and X, respectively. We select as our best estimate for EA(Al_3O_3) the average of the two values yielding (2.12 ± 0.10) eV. Here the

overall error was estimated using the experimental resolution for bands X^x and X together with the uncertainty of the computed value of ΔE_{isom}.

4.3. Larger aluminum oxide clusters

The photoelectron spectra of $Al_4O_x^-$, $Al_5O_x^-$ ($x = 3$–5), $Al_6O_5^-$, and $Al_7O_5^-$ measured at 266 nm represent the first experimental results on these clusters. These spectra do not exhibit resolved vibrational structure. Determination of the VDE's for each band is straightforward, as each corresponds to a band maximum. The ADE of the first band of every spectrum, marked as an arrow in Figures 8.4 and 8.5, is determined from the measured electron binding energy spectrum by extrapolating the linear portion of the first leading edge in the PE spectrum to the energy axis[25]. The crossing between the axis and this line is our best estimate of the ADE. Using this method, the error bars are 60–150 meV. The adiabatic electron detachment and vertical electron detachment energies are reported in Table 8.1.

The lowest ADEs increase as the number of Al or O atoms is increased, with the exception of the $Al_5O_5^-$ PE spectrum, which has a lower ADE than the first band of either the $Al_5O_4^-$ or $Al_4O_5^-$ spectrum. Such a result suggests that neutral Al_5O_5 is particularly stable; further insight into why this might the case would be greatly facilitated by electronic structure calculations in this size regime. No *ab initio* or density functional calculations have been performed on these species, except for the neutral Al_4O_4 cluster[26]. The richness in different calculated low-lying energy isomers for the Al_4O_4 cluster is evidenced by five electronic transitions, A–E, observed in the PE spectrum.

In light of the results for Al_3O_2 and Al_3O_3, contributions from multiple anion isomers are expected in the PE spectra of the larger clusters. The likeliest candidates for such effects are the $Al_4O_3^-$ spectrum, where the weak band A could certainly arise from an anion excited structural isomer, and the $Al_4O_4^-$ and $Al_5O_4^-$ spectra, in which the overlapped bands A and B could originate from transitions from nearly degenerate anion isomers. The computations of Chang et al.[26] find that neutral Al_4O_4 has nearly degenerate singlet di-bridged kite (D_{2h}) and triplet cubic isomers 1 (T_d), so these may be the pairs of isomers leading to bands A and B in the $Al_4O_4^-$ PE spectrum. Finally, the appearance of bands A and B in the $Al_5O_3^-$, $Al_4O_5^-$, and $Al_5O_5^-$ spectra are similar to bands X and X'' in the $Al_3O_3^-$ spectra, so these bands in the larger clusters may also arise from different anion isomers.

The $Al_6O_5^-$ and $Al_7O_5^-$ PE spectra show features at high electron binding energy. Smaller $Al_6O_x^-$ or $Al_7O_x^-$ ($x < 5$) clusters were not observed in the mass spectrum; this together with the high ADE's suggests that $Al_6O_5^-$ and $Al_7O_5^-$ have high stability.

Conclusions:

The vibrationally resolved photoelectron spectra of $Al_3O_2^-$ and $Al_3O_3^-$ together with PE spectra of larger aluminum oxide clusters have been presented. Three electronic bands in the PE spectra of $Al_3O_2^-$ and $Al_3O_3^-$ are discussed in detail and analyzed with the aid of electronic structure calculations and Franck–Condon simulations of vibrational structure. In the $Al_3O_2^-$ PE spectrum, bands X and A are assigned to a transition originating from the lowest energy "kite" anion isomer, while band X' originates from the slightly higher energy "V" anion isomer. While these

assignments were proposed previously, they are confirmed by the intensities,

energetics, and vibrational structure seen in our experimental spectra. Similarly, in the

$Al_3O_3^-$ PE spectra, bands X and A originate from the lowest energy "book" anion

isomer, while band X′ originates from the slightly higher energy "kite" anion isomer.

Computations using the G2 method showed that ΔE_{isom} for the $Al_3O_3^-$ isomers

is lower than ΔE_{isom} for $Al_3O_2^-$, a result consistent with the relative intensities of band

X″ and X in the $Al_3O_2^-$ and $Al_3O_3^-$ photoelectron spectra. Using G2 values of ΔE_{isom}

for the anions and the neutrals, we could derive the EA(Al_3O_2) of (1.62 ± 0.12) eV

and EA(Al_3O_2) of (2.12 ± 0.10) eV.

References:

1. Corma, A., *Inorganic Solid Acids and Their Use in Acid-Catalyzed Hydrocarbon Reactions.* Chemical Review, 1995. **95**: p. 559-614.

2. Ahlstrom-Silversand, A.F. and C.U.I. Odenbrand, *Combustion of methane over a Pd---Al2O3/SiO2 catalyst, catalyst activity and stability.* Applied Catalysis A: General, 1997. **153**(1-2): p. 157-175.

3. Rajagopal, S., et al., *Denitrogenation of piperidine on alumina, silica, and silica-aluminas: The effect of surface acidity.* Journal of Catalysis, 1992. **137**(2): p. 453-461.

4. Kiessling, D., et al., *Dimerization of n-butenes on amorphous NiO-Al2O3/ SiO2 catalysts.* Applied Catalysis, 1991. **71**(1): p. 69-78.

5. Nittler, L.R., et al., *Stellar Sapphires: The Properties and Origins of Presolar Al2O3 in Meteorites.* The Astrophysical Journal, 1997. **483**: p. 475-495.

6. Asmis, K.R., T.R. Taylor, and D.M. Neumark, *Anion photoelectron spectroscopy of B2N-.* The Journal of Chemical Physics, 1999. **111**(19): p. 8838-8851.

7. Asmis, K.R., T.R. Taylor, and D.M. Neumark, *Anion photoelectron spectroscopy of B3N-.* Journal of Chemical Physics, 1999. **111**(23): p. 10491-10500.

8. Gomez, H., T.R. Taylor, and D.M. Neumark, *Anion photoelectron spectroscopy of aluminum phosphide clusters.* Journal of Physical Chemistry A. **105**(28): p. 6886-6893.

9.   Taylor, T.R., et al., *Evolution of electronic structure as a function of size in gallium phosphide semiconductor clusters.* Chemical Physics Letters, 1998. **297**(1-2): p. 133-140.

10.   Taylor, T.R., et al., *Photoelectron spectroscopy of GaX2, Ga2X, Ga2X2, and Ga2X3(X=P,As).* Journal of Chemical Physics, 2001. **115**(10): p. 4620-4631.

11.   Asmis, K.R., T.R. Taylor, and D.M. Neumark, *Electronic structure of indium phosphide clusters: anion photoelectron spectroscopy of InxPx- and Inx+1Px-(x=1-13) clusters.* Chemical Physics Letters, 1999. **308**(5-6): p. 347-354.

12.   Gomez, H., et al., *Spectroscopy of the low-lying states of the group III--V diatomics, AlP, GaP, InP, and GaAs via anion photodetachment spectroscopy.* The Journal of Chemical Physics, 2002. **117**(19): p. 8644-8656.

13.   Wu, H., et al., *Al[sub 3]O[sub y] (y = 0--5) clusters: Sequential oxidation, metal-to-oxide transformation, and photoisomerization.* The Journal of Chemical Physics, 1998. **109**(2): p. 449-458.

14.   Desai, S.R., et al., *A study of the structure and bonding of small aluminum oxide clusters by photoelectron spectroscopy: Al[sub x]O[sub y][sup -] (x = 1--2,y = 1--5).* The Journal of Chemical Physics, 1997. **106**(4): p. 1309-1317.

15.   Akin, F.A. and C.C. Jarrold, *Addition of water and methanol to Al[sub 3]O[sub 3][sup -] studied by mass spectrometry and anion photoelectron spectroscopy.* The Journal of Chemical Physics, 2003. **118**(13): p. 5841-5851.

16.   Akin, F.A. and C.C. Jarrold, *Separating contributions from multiple structural isomers in anion photoelectron spectra: Al[sub 3]O[sub 3][sup -] beam hole burning.* The Journal of Chemical Physics, 2003. **118**(4): p. 1773-1778.

17.   Ghanty, T.K. and E.R. Davidson, *Theoretical Interpretation of the Photoelectron Spectra of Al3O2- and Al3O3-*. Jounal of Physical Chemistry A, 1999. **103**(45): p. 8985-8993.

18.   Martinez, A., et al., *Al3On and Al3On- (n = 1-3) Clusters: Structures, Photoelectron Spectra, Harmonic Vibrational Frequencies, and Atomic Charges*. J. Phys. Chem. A, 2002. **106**(44): p. 10630-10635.

19.   Martinez, A., F.J. Tenorio, and J.V. Ortiz, *Electronic Structure of Al3On and Al3On- (n = 1-3) Clusters*. J. Phys. Chem. A, 2001. **105**(38): p. 8787-8793.

20.   Cui, X.-Y., I. Morrison, and J.-G. Han, *A computational study of photoisomerization in Al[sub 3]O[sub 3][sup -] clusters*. The Journal of Chemical Physics, 2002. **117**(3): p. 1077-1084.

21.   Metz, R.B., et al., *Probing the Transition State with Negative Ion Photodetachment: The CI + HCI and Br 4- HBr Reactions*. Jounal of Physical Chemistry, 1990. **94**: p. 1377-1388.

22.   Xu, C.S., et al., *Photoelectron spectroscopy of C-4(-), C-6(-), and C-8(-)*. Journal of Chemical Physics, 1997. **107**(9): p. 3428-3436.

23.   Frisch, M.J., et al., *GAUSSIAN 98*. 1998, Gaussian Inc.: Pittsburg, PA.

24.   Raghavachari, K. and L. A. Curtiss, *Quantum Mechanical Electronic Structure Calculations with Chemical Accuracy*, ed. S.R. Langhoff. 1995, Dordrecht, The Netherlands: Kluwer Academic.

25.   Xu, C., et al., *Anion photoelectron spectroscopy of small indium phosphide clusters (In[sub x]P[sup -][sub y]; x,y=1--4)*. The Journal of Chemical Physics, 1994. **101**(6): p. 5406-5409.

26.   Chang, C., et al., *Electronic structure investigation of the Al4O4 molecule.* Chemical Physics Letters, 2000. **324**(1-3): p. 108-114.

Chapter 9.   Studies of InP clusters†

Introduction:

Atomic and molecular clusters have attracted tremendous attention because of the unique role they play as bridge between isolated atoms and condensed matter[1]. Semiconductor clusters and nanocrystals are of particular interest because of their size-dependent electrical, optical, photocatalytic, and nonlinear optical properties[2-4]. A fundamental understanding of how the electronic states of such clusters vary with size is one of the central goals of cluster science. While the evolution of semiconductor electronic structure from the nanocrystalline to bulk regimes is now reasonably well understood[5], this size-dependence is more complicated in smaller clusters closer to the molecular limit. In this chapter, photoelectron spectra of size-selected InP cluster anions at 157 nm are presented in order to map out their electronic structure and to probe the size regime over which molecular features begin to resemble those of the bulk material.

Photoelectron spectroscopy (PES) has a rich history in the field of semiconductor physics. Much of our knowledge of valence and core band structure in semiconductors derives from ultraviolet and X-ray PES[6, 7], with angle-resolved measurements in particular playing a key role in elucidating band structure[8]. PES has also been used to examine size-dependent effects in the valence band of nanocrystals[9, 10], complementing information obtained from optical and tunneling spectroscopy[11]. In the gas phase, PES of semiconductor anion clusters has been shown to be a powerful means of mapping out the electronic structure of the neutral

† previously published as: Chem. Phys. Letters **392** 90 (2004).

clusters generated by photodetachment[12].

Anion photoelectron (PE) spectra of mixed group 13–15 clusters have been reported previously, including studies by Smalley's group[13] and the Neumark group of GaAs clusters[14], and experiments by our group on AlP[15], GaP[14, 16], and InP clusters[17, 18]. These investigations yielded size-dependent electron affinities, vertical detachment energies to neutral excited states, and, for the smaller clusters, vibrationally resolved features[14, 15] which could be compared directly with electronic structure calculations. However, the connection between experimental results on small semiconductor clusters and phenomena associated with bulk band structure has proved elusive. Early anion PES[17] and photodissociation experiments[19] on stoichiometric In_xP_x clusters yielded highest occupied molecular orbital – lowest unoccupied molecular orbital (HOMO–LUMO) gaps that were close to the bulk band gap, suggesting, for example, that the excess electron in the cluster anions resided in the cluster analog of the conduction band, but this result appears to have been fortuitous. It is more likely that the extra electron in the anion does not reside in a delocalized conduction band analog, but rather in a localized surface state. As a result, one cannot readily extract the analog of a bulk band gap from the PE spectra of InP cluster anions. A similar holds for silicon clusters[20], although negative ion PES does yield the cluster analog of the band gap in Hg_n and Mg_n clusters[21, 22].

Experimental:

In this chapter, a different approach is undertaken to connecting cluster PE spectra to bulk properties. By photodetaching InP cluster anions with as many as 26

161

atoms further into the vacuum ultraviolet (157 nm, or 7.9 eV, compared to our previous work at 266 nm), we can probe more tightly bound cluster orbitals and make a more detailed comparison with the valence band structure gleaned from bulk photoemission spectra. Wang and co-workers[23, 24] have demonstrated this approach to be quite productive in PES studies (at lower photon energies) of transition metal clusters.

Details of the PES apparatus have been discussed elsewhere[25]. We have, however, added a magnetic bottle electron energy analyzer[26] to expand the capabilities of the instrument. $In_xP_y^-$ ($x = y$ for stoichiometric clusters) clusters were produced by means of a pulsed laser ablation (at 532 nm) of an InP disk coupled to a pulsed supersonic beam of Ar carrier gas. The cluster anions were mass-analyzed with a linear reflectron time-of-flight mass spectrometer for which m/Δm $\approx$ 2000 at an average beam energy of 3.75 keV, and photodetached with a pulsed, fixed frequency, F_2 excimer laser (GAM EX50F), 157 nm and 2 mJ/pulse, with unstable resonator optics.

Photoelectron kinetic energies (eKE's) were determined by time-of-flight measurements using a magnetic bottle analyzer based on the designs by Cheshnovsky et al. [26] and Wang et al[27]. The mass-selected clusters are not decelerated before interaction with the laser. The instrumental resolution is estimated at 0.15 eV for $In_6P_6^-$ at an electron kinetic energy (eKE) of 1 eV. The magnetic bottle region consists of two parts: a strong permanent magnet adjustable in height below the photodetachment zone and a 1.2 m long solenoid. The distance of the permanent magnet from the ion beam and the strength of the magnetic field at the center of the

162

solenoid were chosen to optimize the signal-to-noise ratio. All spectra shown here were background-subtracted to eliminate the contribution from electrons produced by stray 157 nm photons interacting with surfaces near the interaction region.

Results:

Figure 9.1 shows the 157 nm PES spectra of stoichiometric In_xP_x clusters with $x = 2$–13. All PE spectra are plotted as a function of electron binding energy (eBE), defined as eBE = $h\nu$−eKE, where $h\nu$ is the photon energy (7.9 eV at 157 nm). The spectra show several distinct bands corresponding to different electronic states of the neutral cluster. They were calibrated by comparing the features at low eBE with those obtained in our previous study of InP clusters at 266 nm using a field free time-of-flight analyzer[18]. All features in Figure 9.1 at eBE > 4.7 eV (vertical line) are new features that could not be observed at 266 nm.

The $In_xP_x^-$ spectra in Figure 9.1 exhibit several size-dependent trends. The spectra for $x \leq 6$ show numerous discrete electronic features corresponding to various electronic states of the neutral cluster, and exhibit significant differences as the size of the cluster is varied. The number of resolved features drops for $x = 7$ and 8, and for $x \geq 9$, there is a coalescence of features, so that the PE spectra comprise two broad peaks whose shapes change only slightly with increasing cluster size. The main size effect from $x = 9$ to 13 is a small increase in vertical detachment energy (VDE), corresponding to the maximum of the peak at lower eBE; the VDE increases from 4.2 eV for $x = 9$ to 4.4 eV for $x = 13$. In this size regime, the PE spectra are also largely independent of stoichiometry; PE spectra taken for $In_9P_x^-$ ($x = 7,8$) and $In_{10}P_x^-$ ($x = 8,9$) are essentially the same as those for the stoichiometric clusters.

163
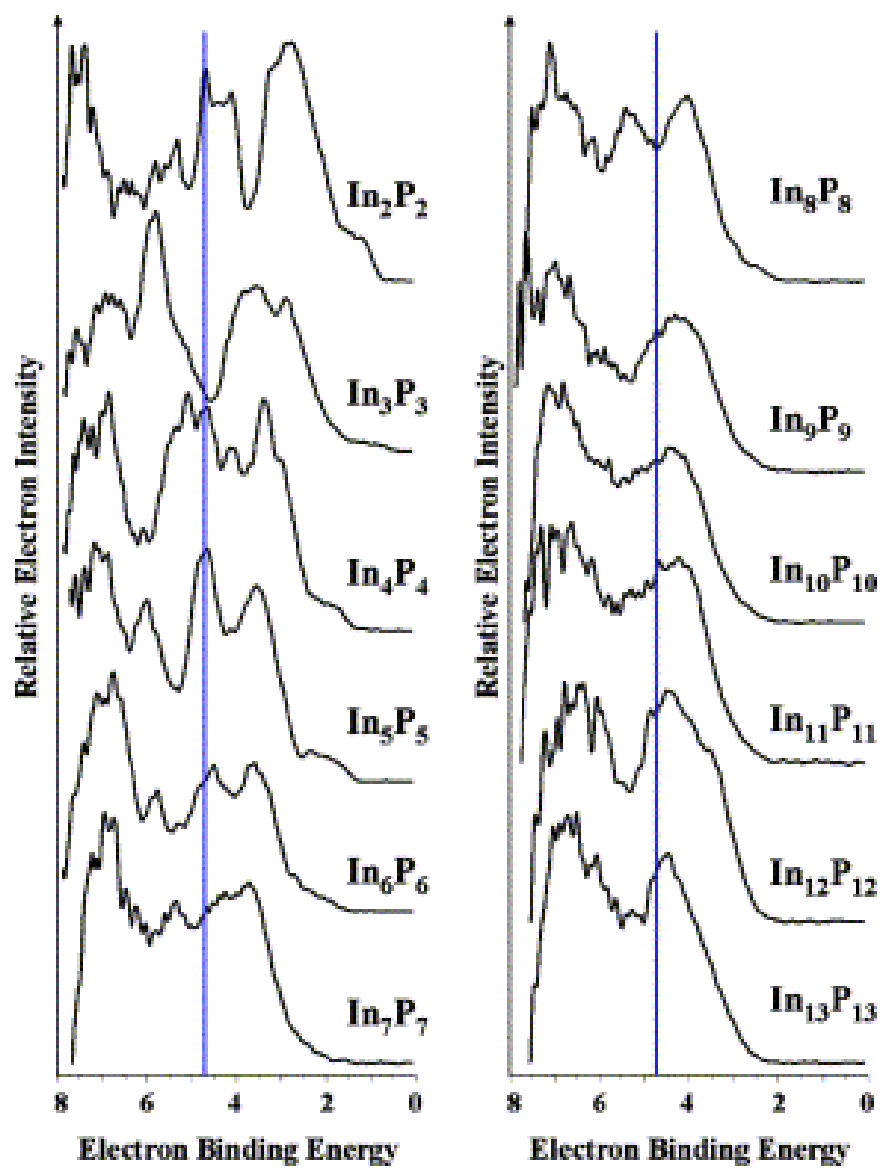
Figure 9.1 – Anion photoelectron spectra of size-selected stoichiometric InxPy−(x=2–13) clusters at 7.9 eV detachment energy.

In photoemission experiments on semiconductor surfaces[7], the photoelectron kinetic energy distribution reflects the density of states (DOS) in the valence and core bands of the bulk material. In the InP photoemission spectrum[6], the highest energy band, whose maximum lies about 2 eV below the valence band (VB) edge, is composed primarily of linear combinations of phosphorus 3p-orbitals, while the next band with maximum at −6 eV is a mix of indium 5s-like states and phosphorus 3p-like states[28]. Our PE spectra for $In_xP_x^-$, $x \geq 9$, are quite similar to the photoemission spectrum. The two peaks in the anion PE spectra are closer together, i.e. their maxima are separated by 2.5–3 eV compared to 4 eV in the photoemission spectrum. Nonetheless, there appears to be a correspondence between features in the anion cluster PE spectra and the bulk photoemission spectra.

In order to address this issue in more detail, electronic structure calculations were carried out to learn more about the geometries and the nature of the molecular orbitals of InP clusters in the size range studied here. We performed density functional calculations on In_3P_3, In_4P_4, In_6P_6, and In_9P_9 at the B3LYP (Becke three-parameter exchange functional with the Lee, Yang, and Parr correlation functional) level of theory. We used the Gaussian98 program suite[29] with a correlated consistent polarized valence double-zeta (cc-pVDZ) basis set for P atoms and a Los Alamos National Laboratory double-zeta (LANL2DZ) with effective core potential (ECP) basis set for In atoms. Many starting geometries were used and only the lowest energy structures are shown in Figure 9.2 All vibrational frequencies for these structures were found to be real, indicating they are at least local minima, but we

165

cannot rule out the possibility of lower-lying isomers that were missed by the optimization procedure. There are not significant changes between anion and neutral geometries. The structures in Figure 9.2 clearly do not resemble the zinc-blende structure of bulk InP. Indeed, if a zinc-blende initial geometry is used for In_9P_9, the dangling bonds disappear and the structure is optimized to maximize the coordination number of each atom.

Our calculated lowest energy geometry for In_3P_3 is almost identical to the work by Costales et al[30]. The structures for In_4P_4, In_6P_6, and In_9P_9 are here described for the first time. In_4P_4 and In_6P_6 can be compared to calculations on other group 13–15 semiconductor clusters, such as Ga_4As_4 [31-33] and Ga_6As_6 [32, 34]. Our In_4P_4 structure has a bicapped octahedral structure with the apex P atoms separated by 2.3 Å, and the four In atoms separated by 3.7 and 4.0 Å. It differs from the lowest energy structures for Ga_4As_4 found by Song et al.[31] and BelBruno [33]; In_4P_4 local minima were located corresponding to those structures and were found to lie 2.1 and 0.6 eV, respectively, higher in energy than our lowest-energy neutral configuration, whereas for the anion these structures lie 0.4 and 0.2 eV above the ground state. In_6P_6 has a distorted C_1 structure, quite different from the Ga_6As_6 molecular arrangements[32, 34]. In_9P_9 has a C_s structure with an average In-P bond distance of 2.6 Å. This structure is a nearly prolate symmetric top, with an asymmetry parameter $\kappa=(2B-A-C)/(A-C)=-0.88$, where A, B, and C are the three rotational constants (in decreasing order) for the equilibrium geometry and $\kappa=-1$ is the limit for a prolate top. In contrast, the smaller clusters are nearly oblate, with $\kappa=0.98$ for In_4P_4.
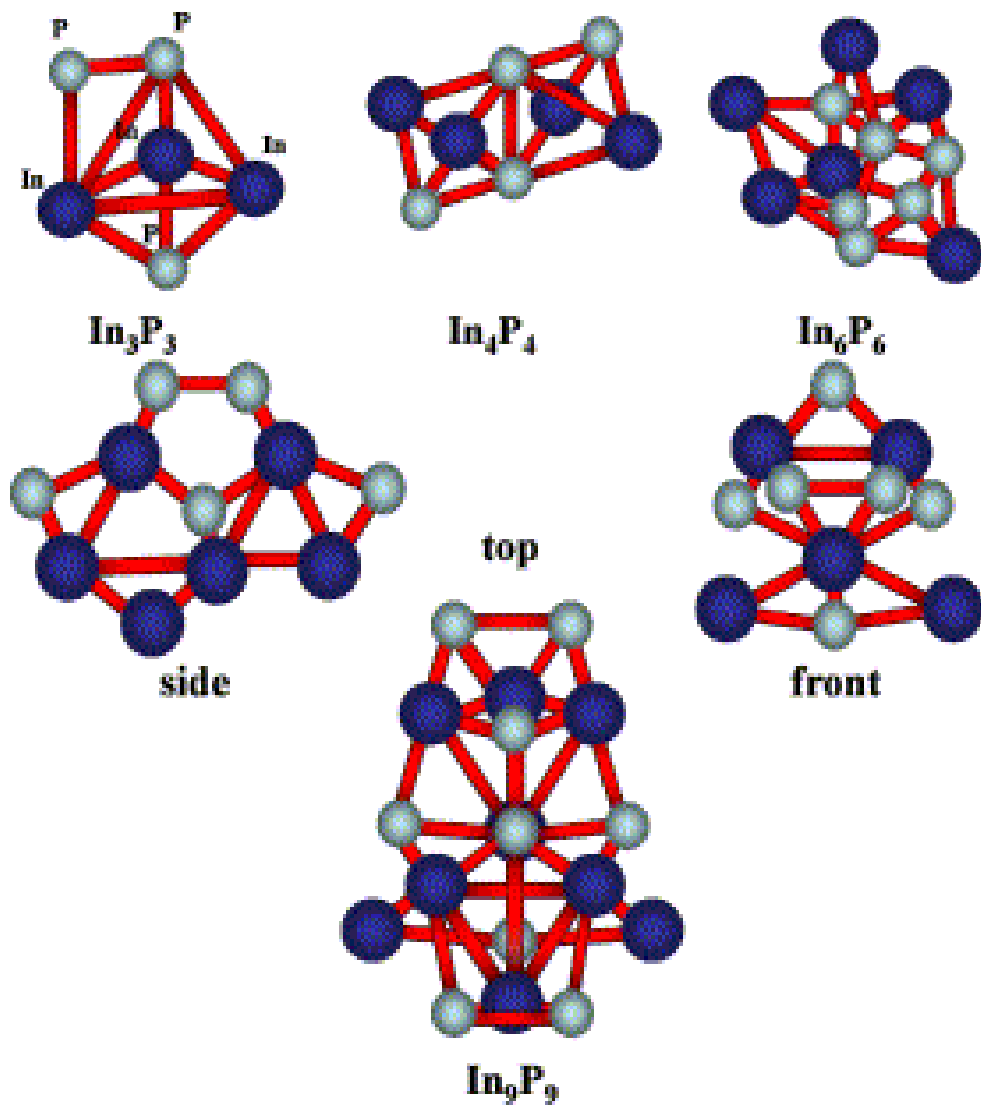
**Figure 9.2** – Structures of the In$_3$P$_3$, In$_4$P$_4$, In$_6$P$_6$, and In$_9$P$_9$ clusters optimized at the

B3LYP level of theory.

Discussion:

The DFT calculations can be used to interpret the trends in electronic structure revealed by the PE spectra, in particular the coalescence of many bands for the smaller clusters into two bands for the larger ones. We analyzed the character of the molecular orbitals (MO) for two cases: In_4P_4 and In_9P_9. Koopman's Theorem was used to obtain binding energies for electrons in each MO of the anion as an approximate means of determining the vertical detachment energy to the ground and multiple excited states of the neutral cluster, using the lowest energy geometries shown in Figure 9.2.

In Figure 9.3, stick spectra indicating MO binding energies in the 0–7.9 eV range are superimposed on the PE spectra. In the case of $In_4P_4^-$, the binding energy of the electron that resides in the singly occupied molecular orbital (SOMO) is considerably less than the next most weakly bound electron. We can identify detachment from the SOMO with the weak shoulder at low binding energy in the experimental PE spectrum (resolved as a distinct peak in our earlier work[17]), and have therefore shifted the calculated stick spectrum by 1.2 eV towards lower eBE to line up the SOMO binding energy with this shoulder. We then observe a reasonable correlation between the remaining calculated binding energies and features in the PE spectrum. The features around 3.1 eV are from detachment from MOs with predominant phosphorous 3p, character, those from 4 to 6 eV correspond to MOs with mixed In 5s and P 3p character, and the feature around 7 eV from MOs with predominant In 5s character.
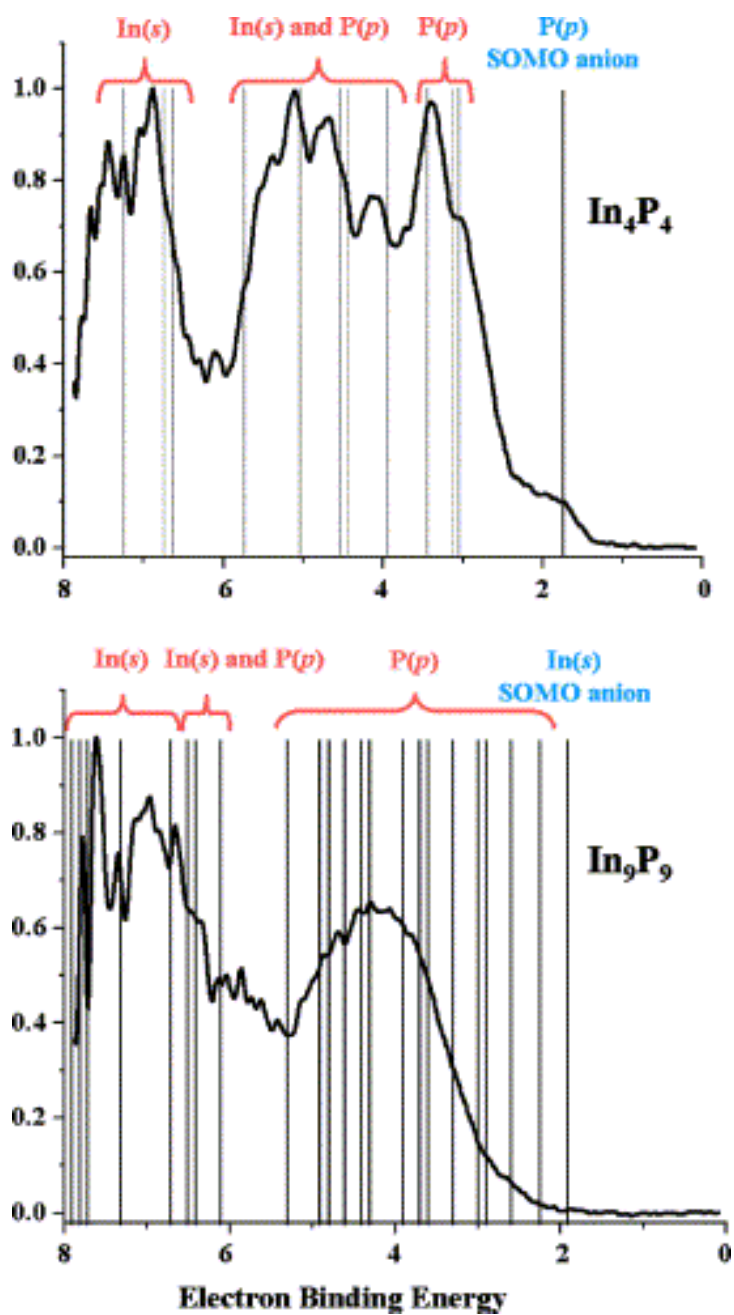
Figure 9.3 – Superimposition of calculated stick spectra for the electronic transitions

of In$_4$P$_4$ and In$_9$P$_9$ on the anion PE spectra taken using 157 nm photon energy.

For In_9P_9, no shift was applied to the calculated stick spectrum. The MO

binding energies segregate into two groups that match reasonably well with the

experimental spectrum. Comparison of the stick and PE spectra suggests that the

lower energy peak comprises MOs of P(3p) character, while the MOs corresponding

to the higher energy peak are a combination of mixed In(5s)/P(3p) and largely pure

In(5s) orbitals. This is the same orbital parentage responsible for the first two bands

in the bulk photoemission spectrum of InP[28]. It therefore appears that two features

in the $In_xP_x^-$ ($x \geq 9$) PE spectra and the first two bands in the bulk photoemission

spectra are of similar origin.

As mentioned above, the splitting between the two bands in the cluster PE

spectra is somewhat smaller than in the bulk photoemission spectra. One possible

explanation is that only the upper part of the more strongly bound band can be

detached at 7.9 eV. However, our electronic structure calculations show no additional

states lying at slightly higher binding energies. In fact, the calculations for In_9P_9 show

a significant gap until around 10.6 eV, where a new band with predominant P(3s)

character is seen, analogous to the third band of the bulk photoemission spectrum[6].

Another possible explanation for the different band spacings could be that the

cluster geometries in the size range probed here are dominated by surface atoms and

deviate considerably from the bulk zinc-blende structure. To explore the relation

between geometry and band splitting, we performed crude single-point energy

calculations on In_9P_9, $In_{13}P_{13}$, and $In_{20}P_{20}$ clusters with the zinc-blende structure using

the B3LYP method. The clusters exhibited two bands of electronic states, with

average splittings of 2.8, 3.1, and 3.6 eV for zinc-blende In_9P_9, $In_{13}P_{13}$, $In_{20}P_{20}$

clusters, respectively. The most tightly bound states for $In_{13}P_{13}$ and $In_{20}P_{20}$ had binding energies of 8.0 and 9.1 eV, respectively. The splitting for zinc-blende In_9P_9 differs only slightly from that for the optimized structure in Figure 11.2 (3.2 eV), but for zinc-blende $In_{20}P_{20}$, the calculated splitting is very close to the bulk value, suggesting that as the number of tetrahedrally coordinate atoms increases, the band spacings approach the bulk valence band splitting. This observation clearly warrants experimental verification through measurement of the PE spectra of slightly larger clusters than were considered here. Unfortunately, signal levels for larger clusters were too small to enable us to obtain their PE spectra, so this investigation will require modifications of our ion source and mass spectrometer configuration.

Conclusions:

Vacuum ultraviolet photoelectron spectra of In_xP_x anions (x = 2–13) clusters were measured to probe the evolution of their electronic structure with size. The spectra of smaller ($x \leq 6$) clusters show numerous discrete electronic features, with fewer seen for x = 7 and 8. For $x \geq 9$, the PE spectra comprise two broad peaks resembling the first two valence bands of the InP bulk photoemission spectrum and calculated density of states. Electronic structure calculations show that the character of the electronic states contributing to the two bands in the cluster PE spectra is similar to that in the bulk photoemission spectrum.

References:

1. Castleman, A.W., et al., *Clusters: structure, energetics, and dynamics of intermediate states of matter.* Journal of Physical Chemistry, 1996. **100**(31): p. 12911-12944.

2. Hatami, F., et al., *InP quantum dots embedded in GaP: Optical properties and carrier dynamics.* Phys. Rev. B, 2004. **67**: p. 085306-085313.

3. Micic, O.I., et al., *Size-dependent spectroscopy of InP quantum dots.* Journal of Physical Chemistry B, 1997. **101**(25): p. 4904-4912.

4. Kan, S., et al., *Synthesis and size-dependent properties of zinc-blende semiconductor quantum rods.* Nature Materials, 2003. **2**(3): p. 155-158.

5. Alivisatos, A.P., *Perspectives on the physical chemistry of semiconductor nanocrystals.* Journal of Physical Chemistry, 1996. **100**(31): p. 13226-13239.

6. Vesely, C.J. and D.L. Kingston, *Valence band density of states of InP and GaSb as determined by X-ray photoemission.* Physical Review B (Solid State), 1973. **8**(6): p. 2685-2687.

7. Ley, L., et al., *Total valence-band densities of states of III-V and II-VI compounds from X-ray photoemission spectroscopy.* Physical Review B (Solid State), 1974. **9**(2): p. 600-621.

8. Smith, N.V., M.M. Traum, and F.J. Di Salvo, *Mapping energy bands in layer compounds from the angular dependence of ultraviolet photoemission.* Solid State Communications, 1974. **15**(2): p. 211-214.

9. Colvin, V.L., A.P. Alivisatos, and J.G. Tobin, *Valence-band photoemission from a quantum-dot system.* Physical Review Letters, 1991. **66**(21): p. 2786-2789.

10. Katari, J.E.B., V.L. Colvin, and A.P. Alivisatos, *X-ray photoelectron spectroscopy of CdSe nanocrystals with applications to studies of the nanocrystal surface.* Journal of Physical Chemistry, 1994. **98**(15): p. 4109-4117.

11. Banin, U. and O. Millo, *Tunneling and optical spectroscopy of semiconductor nanocrystals.* Annual Review Of Physical Chemistry, 2003. **54**: p. 465-492.

12. Cheshnovsky, O., et al., *Ultraviolet photoelectron spectroscopy of semiconductor clusters: Silicon and germanium.* Chemical Physics Letters, 1987. **138**(2-3): p. 119-124.

13. Liu, Y., et al., *Photodetachment and photofragmentation studies of semiconductor cluster anions.* Journal of Chemical Physics, 1986. **85**(12): p. 7434-7441.

14. Taylor, T.R., et al., *Photoelectron spectroscopy of GaX2, Ga2X, Ga2X2, and Ga2X3(X=P,As).* Journal of Chemical Physics, 2001. **115**(10): p. 4620-4631.

15. Gómez, H., T.R. Taylor, and D.M. Neumark, *Anion Photoelectron Spectroscopy of Aluminum Phosphide Clusters.* Journal of Physical Chemistry A, 2001. **105**(28): p. 6886-6893.

16. Taylor, T.R., et al., *Evolution of electronic structure as a function of size in gallium phosphide semiconductor clusters.* Chemical Physics Letters, 1998. **297**(1-2): p. 133-140.

17. Xu, C., et al., *Anion photoelectron spectroscopy of small indium phosphide clusters (In[sub x]P[sup -][sub y]; x,y=1--4).* The Journal of Chemical Physics, 1994. **101**(6): p. 5406-5409.

18.   Asmis, K.R., T.R. Taylor, and D.M. Neumark, *Electronic structure of indium phosphide clusters: anion photoelectron spectroscopy of InxPx- and Inx+1Px- (x=1-13) clusters.* Chemical Physics Letters, 1999. **308**(5-6): p. 347-354.

19.   Kolenbrander, K.D. and M.L. Mandich, *Optical and near-infrared spectroscopy of neutral indium phosphide clusters.* Journal of Chemical Physics, 1990. **92**(8): p. 4759-4767.

20.   Maus, M., G. Gantefor, and W. Eberhardt, *The electronic structure and the band gap of nano-sized Si particles: competition between quantum confinement and surface reconstruction.* Applied Physics A (Materials Science Processing), 2000. **70**(5): p. 535-539.

21.   Busani, R., M. Folkers, and O. Cheshnovsky, *Direct observation of band-gap closure in mercury clusters.* Physical Review Letters, 1998. **81**(18): p. 3836-3839.

22.   Thomas, O.C., et al., *Metallic Behavior in Magnesium Clusters.* Physical Review Letters, 2002. **89**: p. 213403.

23.   Wu, H., S.R. Desai, and L.-S. Wang, *Evolution of the electronic structure of small vanadium clusters from molecular to bulklike.* Physical Review Letters, 1996. **77**(12): p. 2436-2439.

24.   Wang, L.-S., X. Li, and H.-F. Zhang, *Probing the electronic structure of iron clusters using photoelectron spectroscopy.* Chemical Physics, 2000. **262**(1): p. 53-63.

25.   Xu, C.S., et al., *Photoelectron spectroscopy of C-4(-), C-6(-), and C-8(-).* Journal of Chemical Physics, 1997. **107**(9): p. 3428-3436.

26.   Cheshnovsky, O., et al., *Magnetic time-of-flight photoelectron spectrometer for mass-selected negative cluster ions.* Review of Scientific Instruments, 1987. **58**(11): p. 2131-2137.

27.   Wang, L.-S., et al., *Photodetachment photoelectron spectroscopy of multiply charged anions using electrospray ionization.* Review of Scientific Instruments, 1999. **70**(4): p. 1957-1966.

28.   Cohen, M.L. and J.R. Chelikowsky, *Electronic Structure and Optical Properties of Semiconductors.* 1989, New York: Springer.

29.   Frisch, M.J., et al., *GAUSSIAN 98.* 1998, Gaussian Inc.: Pittsburg, PA.

30.   Costales, A., et al., *Theoretical study of structural and vibrational properties of (AIP)n, (AlAs)n, (GaP)n, (GaAs)n, (InP)n, and (InAs)n clusters with n = 1,2,3.* Journal of Physical Chemistry B, 2002. **106**(8): p. 1940-1944.

31.   Song, K.M., A.K. Ray, and P.K. Khowash, *On the electronic structures of GaAs clusters.* Journal of Physics B: Atomic, Molecular and Optical Physics, 1994. **27**(8): p. 1637-1648.

32.   Yi, J.-Y., *Atomic and electronic structures of small GaAs clusters.* Chemical Physics Letters, 2000. **325**(1-3): p. 269-274.

33.   BelBruno, J.J., *Bonding and energetics in small clusters of gallium and arsenic.* Heteroatom Chemistry, 2003. **14**(2): p. 189-196.

34.   Zhao, W. and P.-l. Cao, *Study of the stable structures of Ga6As6 cluster using FP-LMTO MD method.* Physics Letters A, 2001. **288**(1): p. 53-57.

Appendix A: Lab user's manual

This appendix outlines the experimental setup used in the laboratory. It starts off describing the pump laser and general maintenance and problem solving of the laser. Then the optic parametric generator/optic parametric amplifier (OPG/OPA) is discussed. After the OPG/OPA is discussed, finding signal is dealt with.

A general note on safety:

The pump laser used in this lab is a class 4 laser, which can very easily blind and burn the skin of a user. Users should remove all hand and wrist jewelry, especially reflective rings and watches, before operating or repairing the laser. Goggles should be used when aligning. Also the flash lamps produce high levels of UV radiation and can be damaging to the eyes. There is also a considerable electricity hazard associated with the laser. When a user is maintaining the laser, care should be taken not to receive an electrical shock.

Starting the laser and daily routines:

Turn on the main power switch and then turn the key to activate the laser. The user should start by keeping manual mode on and fire the laser at least five times. To manually fire the laser, press the "charge" button on the control panel and then press "fire." After a few shots, press the "auto/manual" button and press "start" when program 1 is selected. Let the laser warm up for about two hours. The laser can be operated after 1 hour, but the lasing threshold will be higher and steadily decrease over time. Once the laser is warmed up, turn the oscillator voltage down below threshold. Place the power meter in front of the laser, turn the laser to program 2, activate program 2, open the shutter and measure and record the lasing threshold.

This may also be done visually with a piece of orange florescent paper. Turn the oscillator voltage 30-40V above threshold and verify that the output voltage is 25-30 mJ. Then take a stability scan of at least 1000 shots. The acceptable range for stability is 2%, but 1% is much more favorable. If the laser is at 2% stability or higher, then perform maintenance on the laser until the stability returns. The acceptable temperature range for the laser is 18-22 degrees Celsius. If the laser is not operated in that temperature range, then it may become unstable. Check especially for very intense pulses because the damage threshold on the LaserVision OPG/OPA is 35 mJ/pulse for a 20 ps laser and laser pulses above 35 mJ/pulse may damage the crystals in the OPG/OPA. Verify that the laser is not generating pulses of that magnitude and record the stability, average power, and maximum pulse in the laser log.

Changing the dye:

The time to change the laser dye is when the threshold of the laser continues to rise over a period of time. The average life span for the laser dye is about three weeks. Take care in how hard the oscillator is pumped because if the flash lamps are pumped too high, the Pockel's cell may be damaged. The sweet spot for my Continuum Leapard is when the threshold is around 1380 V. The dye should be changed when the threshold creeps to 1400 V for more than one day.

In changing the dye, warm up the laser and activate program 2 keeping the shutter closed. Take a spare dye reservoir and fill it with clean, dry 1,3-dichloroethane. Exchange the top of the dye reservoir to the reservoir containing 1,3-dichloroethane. Repeat until the solution in the reservoir is visibly clear. After all of

the dye is flushed, the oscillator cavity is in free running mode. This is when the dye

cell should be optimized. For most dye changes, the dye cell alignment does not need

to be optimized. The dye cell should be optimized only if there is a stability issue or if

there was a recent large change in the ambient temperature.

After the laser is in free running mode, dye can be added to the reservoir. To

make a dye solution, take a clean sample vial and place around 20 mg of Q-Switch 1

laser dye inside of it and fill it ¾ of the way with 1,3-dichloroethane. Then place this

solution into a sonicator for at least fifteen minutes. Once the stock solution is

prepared, it should be stored in a freezer. Place a fast photodiode inside the laser so

that the pulse train can be visible. To see the pulse train, block the Pockel's cell

trigger and block the output of the oscillator before it enters the amplifier (it is not

necessary to block the output of the oscillator, but for safety reasons it is best to limit

the beams entering the amplifier). When adding dye, use the syringe and pull some of

the solution already in the reservoir into the syringe and then deposit the solution into

the reservoir (this will help to increase mixing). After the dye solution is added to the

dye cell, wait 30 seconds, turn down the oscillator voltage, and open the shutter. Look

at the pulse train by setting a fast photodiode to fifty ohms impedance and triggering

off of the highest peak on the pulse train. Continue to add dye until the pulse train

looks similar to Figure 2.1 and the lasing threshold is similar to standard operating

parameters. Once the dye has been changed and the work for the day has been

completed, turn off the flash lamps and the high voltage on the laser and let the dye

circulate all evening long.
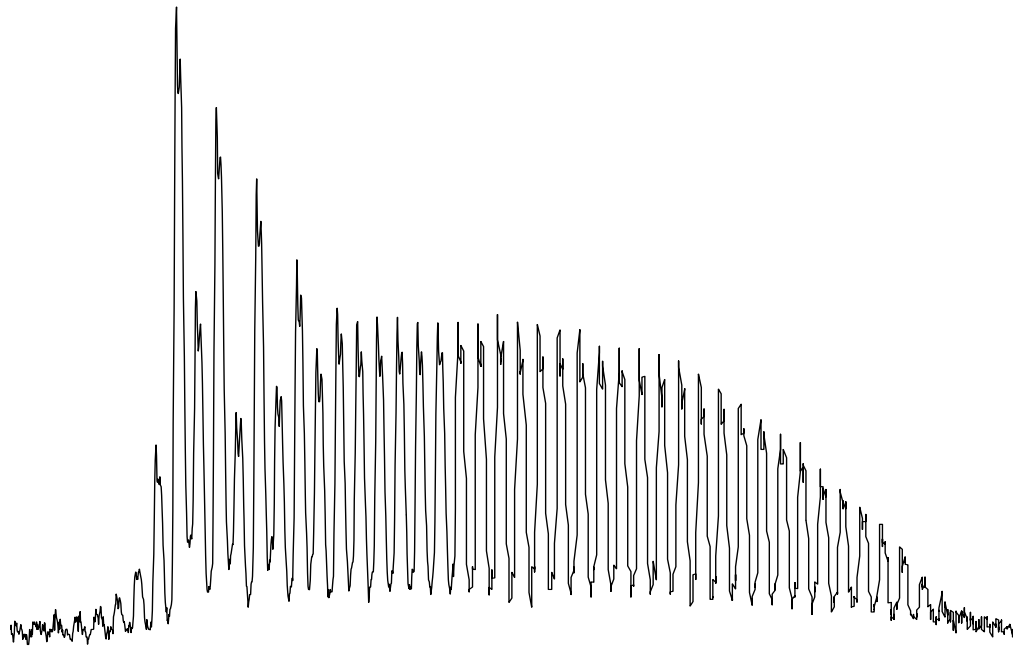
Figure 1 – The pulse train inside the oscillator cavity of the laser.

The pulse train needs to have a flat area where the pulse can be selected. To check

where the pulse is being selected, remove the block to the Pockel's cell and the pulse

should look similar to Figure 2.2.
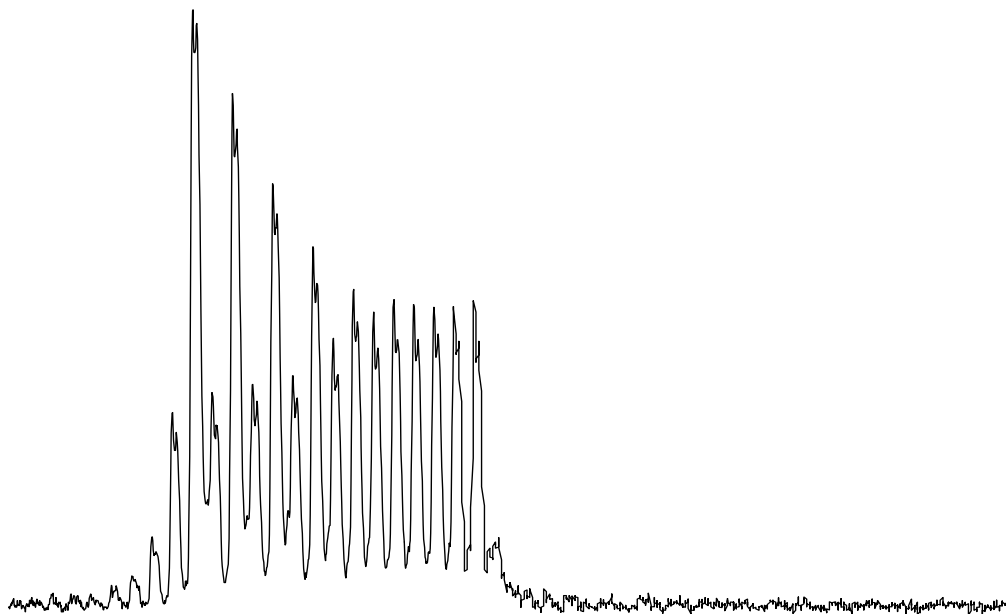
Figure 2 – The pulse train after the pulse is selected from the oscillator. The selected

pulse needs to be from the flat area of the pulse train. If the selected pulse is taken too

early, the laser may be unstable.

Regaining stability:

The stability of the laser usually lies in the oscillator cavity. The alignment of

the laser cavity is very dependant on the ambient temperature. If the laboratory is too

hot then the laser can become unstable and generate large pulses. It is best to keep the

lab at around twenty degrees Celsius. If the laser is still unstable even though

temperature is around 20 degrees Celsius, then the dye cell alignment should be

optimized. Place the photodiode to view the pulse train of the oscillator and block the

Pockel's cell trigger and the output of the oscillator to the amplifier. Using the scope,

turn the impedance of the photodiode to one mega ohm and trigger off of the laser

flash lamps externally. The pulse should look like Figure 2.3.

Figure 3 – Free running mode. This can be viewed when the impedance of the

photodiode is set to high.

Turn off the acusto optic mode locker (AOML) by pressing the button on the power

supply and put pure 1,3-dichloroethane in the dye cell so that the laser is in free

running mode. Now tweak the mirrors of the dye cell by using an Allen wrench to

turn the setscrews on the dye cell. The dye cell is optimized when the buildup time in

the oscillator cavity is minimized, or the pulse is moved furthest toward the left.

Add dye to the dye reservoir and check to see if stability returns (be sure to

turn the AOML back on). If stability still has not returned, then the next step is to

tweak the AOML. To change the AOML, one of the screws on top of the AOML

must be tightened while the other is simultaneously loosened. The AOML is

maximized when the pulse from the photodiode on its "slow" setting is moved to the

right or when the buildup time in the oscillator cavity is maximized. The pulse will go

through a maximum as the AOML is tweaked. The user should notice this maximum

as it passes and set the AOML to this maximum. The horizontal position (with respect

to the beam within the dye cell being vertical) of the AOML does not need to be

tweaked after it is set initially. Now turn off the AOML and observe the pulse from

the photodiode. If the pulse moves to the left by around 15 microseconds, then the

AOML is in it's optimum setting.

If stability still does not return, then proceed to change the frequency of the

AOML. First write down the frequency of the AOML before it is changed. At the

time this thesis is written, the frequency of the AOML is 70214 kHz. Each AOML

has a different frequency associated with it, so other lasers may not have similar

frequency values and if the AOML has to be changed, then the optimum frequency

will change also. Move the frequency by about 10 kHz at a time at first then move to

single kHz changes. The object of this exercise is to increase the build up time of the

light pulse in the laser cavity. The AOML may also need to be tweaked as the

frequency changes. This procedure optimizing the frequency and AOML build up

time may have to be iterated several times.

Once the frequency and position of the AOML is optimized, turn the

impedance of the channel to which the photodiode is connected to fifty ohms and

trigger off of the same channel as the photodiode. Adjust the trigger height to the

largest pulse in the pulse train. Verify that the pulse train does not vary in length. If it

does vary in length greatly, turn the prism in the oscillator cavity a little to try to

correct for any oscillations (it may be fruitful to mark how much the prism has moved

so the original position can always be returned). Remove the block to the Pockel's

cell trigger and observe the pulse train. If the selected pulse is not in the flat area of

the pulse train, add paper in front of the Pockel's cell's optical trigger until the correct

pulse is selected. Now look at the pulse leaving the oscillator. Use the potentiometer

on the Pockel's cell trigger to fine tune pulse selection. The large pulse leaving the

oscillator should be at least seven times greater than the remnants of the pulse train.

Figure 2.4 illustrates a pulse leaving the amplifier.
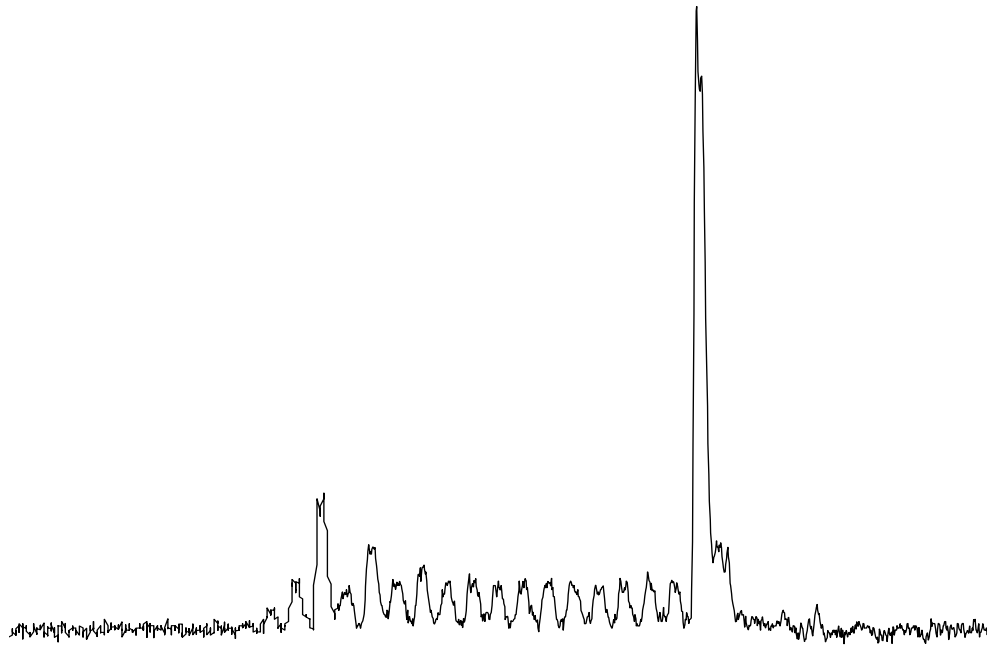
Figure 4 – Pulse leaving the oscillator.

The pulse entering the amplifier should have the same ratio be on the order of forty-

to-one. Figure 2.5 illustrates this pulse.
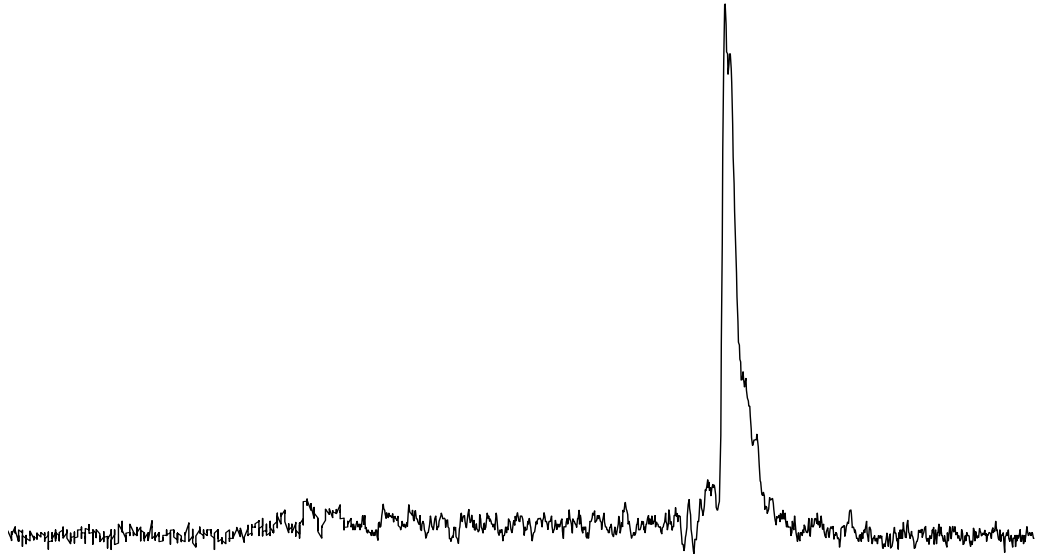
Figure 5 – Pulse entering the amplifier.

To decrease leakage (leakage is extra light entering the amplifier other than the mode-locked pulse) the Pockel's cell can be tweaked. If stability still does not return after, then call Continuum and ask for advice.

Faraday isolator:

If while the shutter is closed there is a laser pulse leaving the laser, then a parasitic oscillation is most likely taking place. Parasitic oscillation is a separate free running mode that forms between the oscillator and the amplifier. The Faraday isolator minimizes parasitic oscillation. If parasitic oscillation takes place, the polarizers and quarter wave plates in the Faraday isolator need to be tweaked. First mark any starting positions with a pencil, a marker, or white paint. Place the slow photodiode collecting light from a card leaving the amplifier and monitor the free running mode. Rotate the quarter wave plates in the Faraday isolator and observe if it

removes the free running mode. Next rotate the polarizers. Moving the polarizers may move the beam slightly and may decrease the amount of energy in the beam. The beam entering the amplifier should be around 200 micro joules of energy. The polarizers' angle should be around a Brewster angle. Turn the amplifier up 100 V above operating voltage and move the polarizers such that the free running mode leaving the amplifier disappears. Turn the amplifier voltage back down to its normal operating value and check to see if the beam entering the amplifier needs to be tweaked by putting on safety glasses and looking at the beam visibly with florescent paper. If the beam is asymmetrical, then tweak the mirror closest to the Faraday isolator to get the beam centered in the pinhole. If a free running mode does not disappear after tweaking the polarizers and quarter wave plates, or if the output energy of the laser is too low, then Continuum should be called so a field engineer can assess the situation.

Aligning the OPG/OPA:

Irises should be set up in the OPG/OPA to expedite this process. There may be several stray beams coming from the LaserVision box when it is open, so extreme care and safety glasses are always recommended. Make sure the 1064 nm from the pump laser is going through those irises and entering into the OPG and OPA. Start with the alignment of the OPG. Close the irises so that only a small amount of green light is entering the OPG. Remove the 532 nm mirror labeled "C" on Figure 6. Move the crystals so that the back reflections from the crystals form a vertical line. Verify that the light is entering the crystals in the middle of the crystals (or that the light is clear of any burn marks if they are present on the crystals). Replace the end 532

185

mirror and place it so that the back reflection goes through the center of the closed iris (this can be further observed in the back reflection out of the OPG/OPA). Remove the stacked silica to the OPA and open the irises to the OPG. A faint green beam should be visible entering the OPA. Use the half wave plate to turn down the 1064 going to the OPA.

Move the crystals in the OPA to a visible normal (eyeball the positions). Remove the stacked silica exiting the OPA and the 1064 mirror. Now use the faint green beam from the OPG to align it through the center of the crystals in the OPA. It may also be fruitful to set up temporary irises on the table so that the beam is entering into the crystals in a straight line. After the beam from the OPG is centered onto the OPA crystals, overlap the 1064 beam with the faint green beam from the OPG. The maximum output power will be when the two beams are completely overlapped.

After the beams are overlapped, put the crystals about 5500 motor positions past a visible normal such that they are in the relative position of \ / or a "v" with the point toward the opening of the box. Put the stacked silica back into the OPG (not the stacked silica leaving the OPA, the one that after removed, the faint green beam enters the OPA) and put the 1064 mirror in the path of the beam exiting the OPA. For safety, maneuver the discarded 1064 into a beam dump. Put a power meter exiting the OPA and maximize the power leaving the OPA. To maximize the power, the user must iterate between changing the motor positions, timing, and beam positions. The 5500 motor positions is an approximation, the optimum may be over 1000 motor positions past that. The two beams in the OPA should be tweaked slightly, but it may greatly increase the power output.

Once the power leaving the OPA is maximized, replace the stacked silica leaving the OPA. The location of the stacked silica will greatly affect the power output. The stacked silica can be put on a rotating stage. After calibrating the output of the OPG/OPA, set the output to 2900 cm^{-1} and try to minimize the output. The best spot to be in is a little before this minimum because at this minimum a lot of infrared light is adsorbed. Move the infrared back to 2850 cm^{-1}. There should be at least 400 micro joules of power leaving the OPG/OPA.

The 532 nm used for the experiment is generated in the OPG. The residual 1064 nm from the doubling crystal, number 5 in Figure 6, in the OPG is directed via 1064 mirror to another doubling crystal, number 6. This beam then exits the OPG. Any residual 1064 is deflected to a beam dump. The polarizers labeled O and P control the power of the light exiting the OPG/OPA. The polarizers dictate how much 1064 nm light is entering each stage.
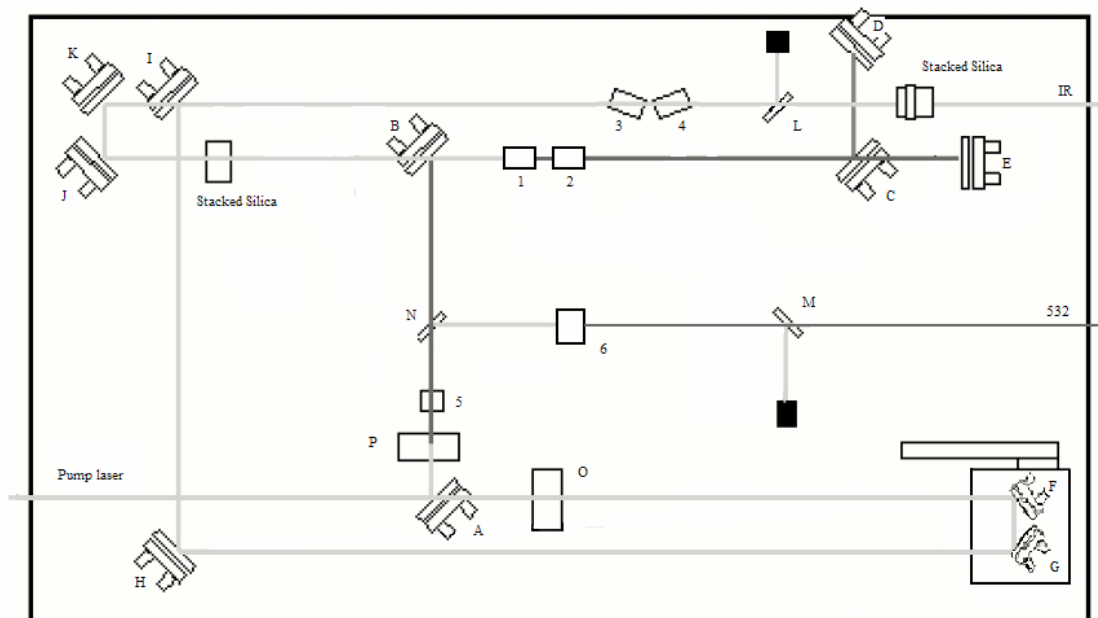
Figure 6 – Setup for the OPG/OPA. The crystals are numbered and the other

components are given letters. The 532 nm and tunable IR beams are labeled.

Calibrating the OPG/OPA:

The IR leaving the OPG/OPA is calibrated by and adsorption spectrum from a

polystyrene film. A typical spectrum is shown in Figure 2.7.
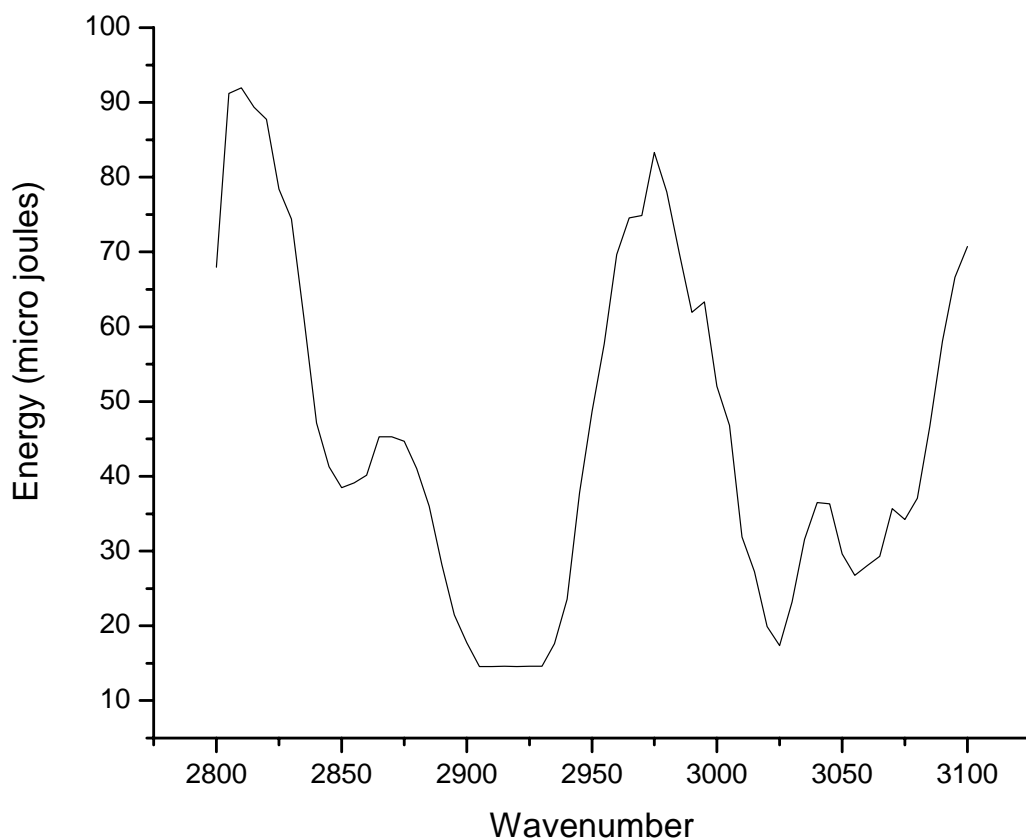
Figure 7 – Polystyrene spectrum.

The things to note on the calibration spectrum are the local minimum at 2850 cm^{-1},
the shoulder at 2990 cm^{-1} and the three valleys at 3025 cm^{-1}, 3055 cm^{-1} and 3075 cm^{-1}. If the local minimum is not at 2850 cm^{-1}, then move the motors to where the
minimum lies and open one of the setup programs and zero the first four motors. Take
another polystyrene scan and iterate if necessary. If the resolution of the spectrum is
off, remove the polystyrene and move crystals three and four until the power output is
maximized. Then take a new polystyrene scan to verify that it is calibrated.

Setting up for sum frequency generation:

In order to generate the sum frequency, four things need to be correct: the spatial overlap of the two laser beams, the timing of the incumbent beams, the polarization of the beams and the collection of the sum frequency in the detector. There are several tools which will ease both the setup of the sum frequency generation and the day-to-day trials of finding signal.

Laser 2

SFG
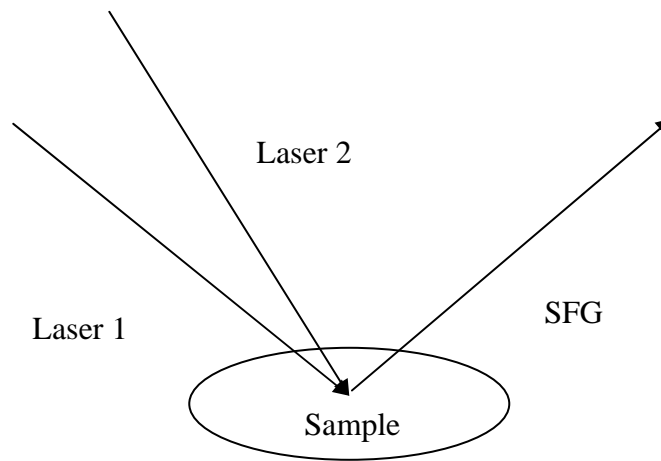
Laser 1

Sample

Figure 8 – SFG illustration. In order to generate SFG, two laser beams of the proper polarization must be spatially and temporally overlapped onto the sample.

To set up collection, line up a monochromator attached to a photo multiplier tube (PMT) onto the breadboard of the laser table and have two mirrors to maneuver the SFG into the PMT. The two mirrors are necessary to account for the two degrees of freedom in the SFG beam, the vertical and horizontal directions. First use the two collection mirrors and two irises of the same height to align the visible beam off of the sample to the monochromator in a straight, level beam. The best way to ensure a straight beam is to put the iris stands of the same height along the same path of holes

in the breadboard and then place a collar on a single iris, set to the height of the

monochromator, and use the same iris for both stands. To straighten the beam iterate

the position of the visible beam by first using the mirror closest to the sample to direct

the visible beam onto the iris furthest from the monochromator and using the mirror

furthest from the sample to direct the beam to the iris closest to the monochromator.

By iterating with those two mirrors and those two points, the beam will eventually

converge to be collinear with the holes of the breadboard and be parallel to the floor.
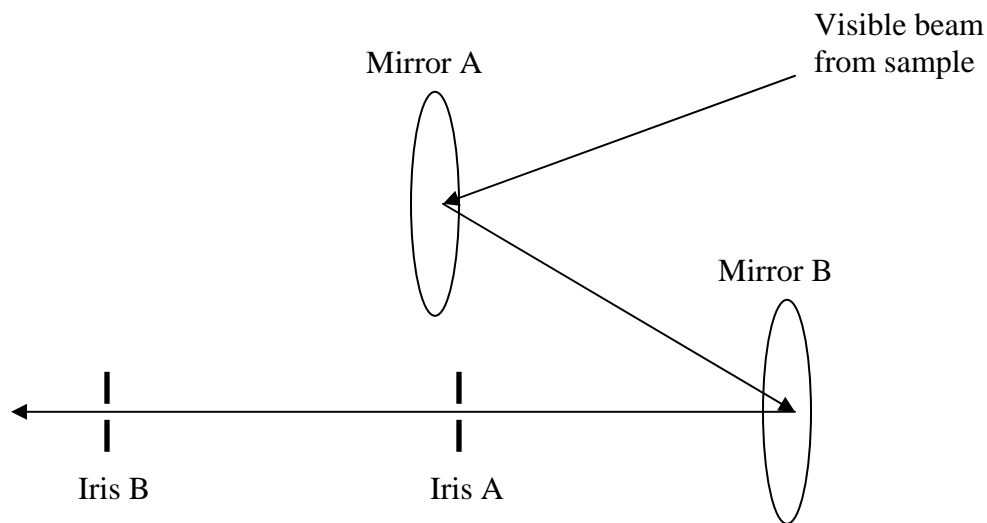
Figure 9 – Monochromator set-up. To align the visible beam straight and level to the

monochromator, iterate the position of the beam between using Mirror A to position

the beam onto Iris A and Mirror B to position the beam to Iris B.

Now that a visible beam is set up that is collinear with the holes in the

breadboard and level, it is time to place the monochromator. Take the detector off of

the monochromator and take the top off of the monochromator so the inside of the

apparatus is visible. Tune the monochromator to 532 nm. Then position the

monochromator so that the amount of light both entering and exiting the

monochromator from the 532 nm beam is maximized. After the beam is centered with

the monochromator, place the focusing lense into the center of the path of the beam.

Next move the position of the lense until the amount of light entering and exiting the

monochromator is again maximized. When the position of the monochromator is

maximized, replace the top and secure the position of the monochromator as much as

possible with screws, mounts, and double stick tape. The more the monochromator's

position is secured, the less frequently the setup will have to be revisited because the

monochromator may be bumped occasionally.

After the monochromator's position is fixed, the position of the PMT can be

maximized. Center the PMT in the housing such that the amount of light reaching the

PMT is maximized. Then place the PMT and housing onto the monochromator to

attain maximum light collection. Now secure the position of the PMT and housing

with mounts, screws and tape. Use black duct tape or black vinyl electrical tape to

cover any sections of the PMT housing or monochromator where ambient light may

leak in. Cover the PMT housing and monochromator as much as possible using dark

cloth or extra housing, like opaque Plexiglas, to keep ambient light from entering the

PMT.

The IR beam should have a visible HeNe beam that is collinear to it to aid in

alignment. Once again, two mirrors are needed to ensure the position of this collinear

beam. The procedure is very similar to creating a straight and level visible beam,

instead now instead of irises determining the position of the visible beam, the use of

liquid crystal paper or an IR viewer can be employed. This aids in the overlap

because the liquid crystal paper changes color when the IR beam comes in contact with it and the HeNe's red characteristic color is easily discernable on the liquid crystal. If the IR viewer is used, just take a piece of white paper and look at the spot on the paper. The IR beam will flash at 20 Hz, while the HeNe will appear continuous. Chose two spots to align the beams. Then set the HeNe's position is set by iterating between the visible mirror closest to the HeNe to center the overlap on to the liquid crystal paper furthest from the sample and the visible mirror further away from the HeNe to center the beam onto the liquid crystal paper closer to the sample.

Mirror A

HeNe

IR laser

Mirror B   Spot A   Spot B
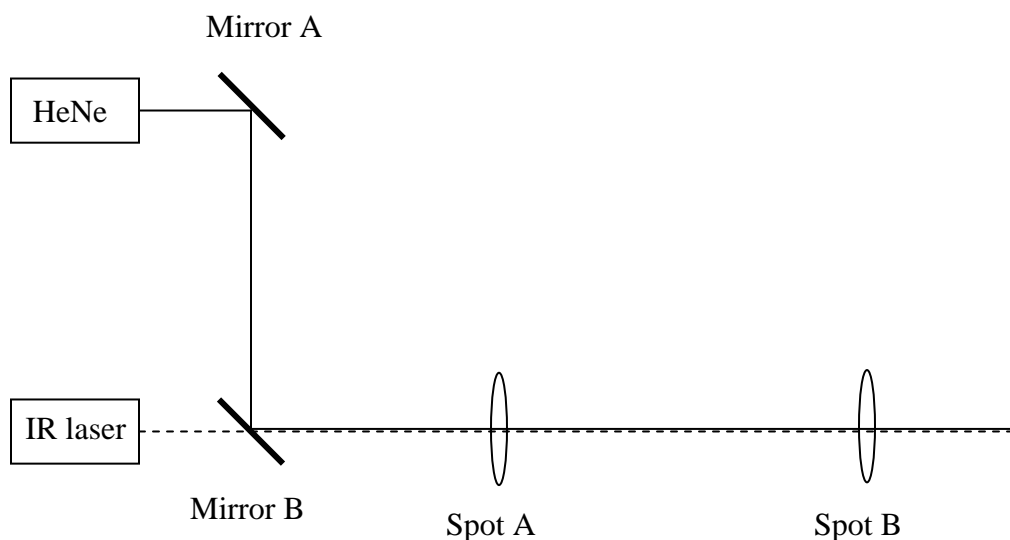
Figure 10 – Overlapping the infrared beam with a HeNe laser. To align a HeNe (solid line) collinear to the IR beam (dashed line), use two mirrors and iterate centering the beam onto two points using either liquid crystal paper or an IR viewer.

Timing is the next step in finding SFG and it is aided by using a zinc selenide (ZnSe) crystal. Set up a translating stage with two visible mirrors on it and align the laser such that when the stage is moved, the beam does not skew. Measure the

distance that the IR and visible beams travel and place the timing stage such that the distance the two beams travel is approximately the same. Measure this distance from where the two laser beams are generated, or from the doubling crystal in the OPG for the 532 nm and after crystal 4 in the OPA. Place the ZnSe in a convenient location before the sample and visibly overlap the two SFG generating beams. If any focusing mirrors, telescopes, polarizers etc. are used for the SFG generating beams, place them before the ZnSe. Align the detector stage with the visible beam and then move the visible beam off a little. The SFG beam will be between the visible and IR beams but closer to the visible beam. At this point, the detector should be on and the monochromator should be tuned to the sum frequency of the two beams. Make sure not to overload the detector. Filters are recommended to keep the visible beam from entering the PMT and monochromator. Hopefully, there will be some SFG signal. If there is no SFG signal, make sure the two beams are overlapped on the ZnSe, play with the detector mirrors a bit. If there is still no signal, move the mirrors such that the SFG beam should be going into the monochromator and move the timing stage until SFG signal is observed. Once signal is observed, maximize the position of the mirrors before the detector, the overlap of the two laser beams on the ZnSe and turn the PMT voltage down to keep it from overloading. Now continue to vary the timing. There will be more than one maximum for the SFG signal off of ZnSe. The point at which to keep the timing stage is when there is the largest signal off of the ZnSe. This can be tricky because there could be several times which yield signal off of ZnSe.
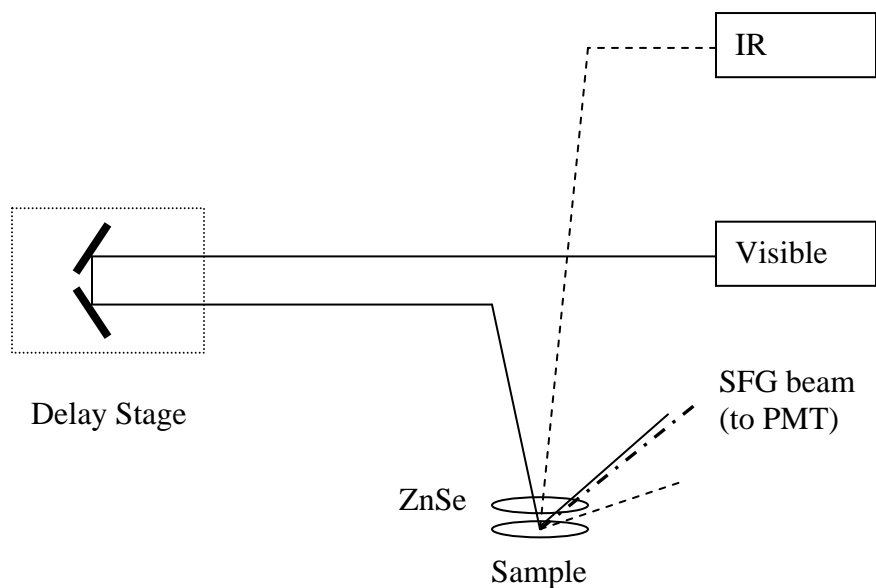
Figure 11 – SFG timing stage. Use the delay stage to find signal from ZnSe. Scan the timing and find the time in which the SFG generation is maximized.

Now that the timing is maximized for ZnSe, remove the sample and place gold in the same position as the sample. The gold should be clean and shiny so that a good reflection is generated. The SFG signal off of gold is dependent on the polarization of the SFG generating beams. Use polarizers to make the beams of PPP polarization as they hit the sample. The IR laser beam can be further verified by using either stacked silica or germania for the PPP polarization. Overlap the two laser

beams onto the gold and turn on the PMT to its highest setting (once signal is found turn the voltage of the PMT down as to keep it from overloading). Maximize the signal by moving the collection mirrors, tweaking overlap, and adjusting the timing stage. Use the irises that were originally used for to align the PMT with the visible beam to center the SFG beam into the monochromator. After the signal is maximized off of the gold, center irises to the visible beam coming off of the sample. The irises will block the SFG beam from the sample, so set up posts and place a collar on an iris so that the iris can be easily removed. These two irises will greatly simplify finding signal in the future.
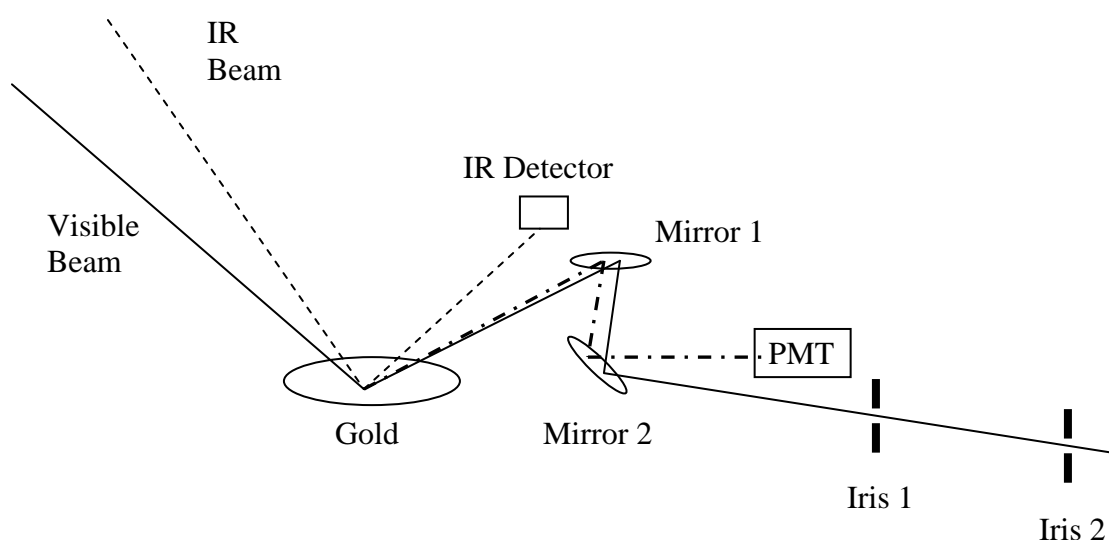
Figure 12 – Setting up the collection irises. After the signal has been maximized off of gold and the SFG beam centered, place two irises in the path of the visible beam coming off of the sample. The SFG beam is the beam between the visible and IR beams.

Replace the sample where the gold was and look for the background off of the sample. If the experiment calls for ultra high vacuum, look for background signal

before baking out because one may have to revert back to the gold and looking for signal in air will save the bake out time. Overlap the two SFG generating beams on the sample. Use the two irises and the two mirrors iterating between using mirror 1, in figure 5, to center the beam to iris 1 and mirror 2 for iris 2. After a few iterations, the signal should appear. Then do fine adjustments to the mirrors to get the beam centered, maximize the overlap, and maximize the timing stage. If the signal does not appear, check to see if the signal is maximized off of gold again. Take a background scan and verify that the background is flat. If the background is curved, then the most likely culprit is the infrared focusing lense before the sample. Moving the beam to the center of the lense and maximizing the overlap should fix this problem. If the irises worked for finding signal, then use these as the basis for finding signal in the future. The irises can even aid in finding signal as the experiment is progressing if the sample moves.